Magnesium Sulfonyldibenzoates: Synthesis, Structure, Phase Transformation and Microscopic Studies

By: Kaitlyn Lucas

Submitted in Partial Fulfillment of the Requirements

for the Degree of

Master of Science

in the

Chemistry

Program

YOUNGSTOWN STATE UNIVERSITY

December, 2013

Abstract

Metal-Organic Frameworks, or MOFs, are crystalline materials consisting of metal ions or clusters coordinated to often rigid or flexible organic linkers to form two- or three-dimensional structures. MOFs can be porous, and the voids within the MOFs can host other molecules such as solvents or gases. A current and newly explored area of MOFs involves the reaction of magnesium salts with different carboxylates. These specific MOFs can have good stability to adsorb and desorb gases at higher temperatures. Solvothermal synthesis is the method used to produce these frameworks; however other methods have been tested and reported. Also the syntheses can be environmentally friendly, using less harmful chemicals to produce the products, and require little to no work up considering the products contain almost no impurities. Once the frameworks are produced it is applicable that they be connected to a planar substrate for further commercial use. By using reactive seeding and other methods there are several different ways that MOFs can be attached to a support. The specific aim of this project is to develop novel magnesium metal-organic frameworks, characterize them and then test their adsorption properties for different types of gases.

Acknowledgements

The following persons were my guidance and support throughout my research. With extra ears, eyes, thoughts, ideas, and encouragement I was able to go beyond my expectations and produce at my best abilities. Many thanks to Dr. Sherri Lovelace-Cameron, Mrs. Carol J. Hirt, Mr. Andrew Hirt, and Materials Research Laboratories staff, Dr. Ruigang Wang, Dr. Matthias Zeller, Dr. Koteswara Rao Vandavasi, Dr. Timothy Wagner, Dr. Peter Norris, Dr. Allen Hunter, Dr. Larry Curtin, and Mr. Tausif Siddiqui. I would also like to thank my dear friends and colleagues, and YSU Chemistry Department.

I would like to acknowledge the Cushwa Commercial/Shearing Fellowship Foundation for providing me with the ability to gain industrial experience at Materials Research Laboratories Inc. while completing my Master's degree at Youngstown State University.

I am dedicating this thesis to my loving and supporting fiancé, Josh Miller, and also to my parents, Mr. Nick Lucas, and Mrs. Pamela Crothers. Their love for me has taught me to grow, fulfill my dreams, and follow my heart beyond my own expectations.

Table of Contents

Abstract iii

Acknowledgements iv

Table of Contents v

List of Figures viii

List of Tables xi

List of Schemes xi

List of Abbreviations xii

Chapter 1

1.1 Background 1

1.2 Application Background 3

1.2.1 Pressure Swing Adsorption 3

1.2.2 Composite Technology vs. Carbon Absorbers 5

1.2.3 Zeolites 7

1.2.4 Mesoporous Materials 8

1.3 Types of Frameworks 11

1.3.1 Open Metal/Extended Frameworks 11

1.3.2 Frameworks with High Surface Areas (BETs) 16

1.3.3 Lewis Acidic Frameworks 22

1.3.4 MOF Table Summary 24

1.4 Alumina Support 24

1.5 Mechanical Synthetic Approach 26

Chapter 2

2.1 Metal-Organic Frameworks 27

2.1.1 Concept of a Metal Organic Framework 27

2.1.2 Molecular Metal-Organic Hybrid 30

2.1.3 Porosity 31

2.1.4 Topology 33

2.1.5 Interpenetration 34

2.2 Pore Expansion 35

2.2.1 Mg-MOF-74 35

2.3 Reactant Theory Beginning with Magnesium 37

2.3.1 Organic Linker 39

2.3.2 4,4'-Bipyridine: A Weak Base 40

2.4 Metal and Organic Linker Synthetic Theory 41

Chapter 3

3.1 Characterization Techniques 45

3.1.1 X-Ray Diffraction (XRD) 45

3.1.2 Scanning Electron Microscopy 48

3.1.3 Energy Dispersive X-Ray Spectroscopy (EDS) 50

3.1.4 Thermogravametric Analysis (TGA) / Differential Scanning Calorimetry (DSC) 51

3.2 Statement of Purpose 52

3.3 Experimental 52

3.3.1 Materials 52

3.3.2 Autoclave Preparation 52

3.3.3 Reaction Preparation 53

3.3.4 Powder X-Ray Diffraction 53

3.3.5 Single Crystal X-ray Diffraction 54

3.3.6 SEM/EDS Analysis 55

3.3.7 TGA/DSC Analysis 55

3.3.8 Clausius Clapeyron Equation 56

Chapter 4

4.1 $[Mg]_3[SDBA]_3[DMF]_3MeOH$ [1] 57

4.2 $[Mg]_3[SDBA]_3[DMF]_3EtOH$ [2] 57

4.3 $[Mg]_3[SDBA]_3[DMF]_3EtOH{\cdot}H_2O$ [3] 58

4.4 $[Mg]_3[SDBA]_3[DMF]_4$ [4] 58

4.5 [SDBA][Bipy] [5] 59

4.6 Ball Milled Product [6] 60

4.7 Al_2O_3 Pellet 60

4.8 $[Mg]_3[SDBA]_3[DMF]_3MeOH$ [1] on Al_2O_3 Pellet 61

Chapter 5

5.1 Macroscopic Observations 62

5.2 Results 62

5.2.1 $[Mg]_3[SDBA]_3[DMF]_3MeOH$ 66

5.2.2 $[Mg]_3[SDBA]_3[DMF]_3EtOH$ 78

5.2.3 $[Mg]_3[SDBA]_3[DMF]_3EtOH{\cdot}H2O$ 87

5.2.4 $[Mg]_3[SDBA]_3[DMF]_4$ 92

5.2.5 [SDBA][Bipy]byproduct from [1] 104

5.2.6 Ball Mill Product [7] 110

5.2.7 Alumina Pellet Support 114

Chapter 6

6.1 Metal-Organic Frameworks 121

6.2 [SDBA][Bipy] [5] and Ball Milled Product [6] 122

6.3 Alumina Support 123

6.4 Conclusion 124

6.5 Future Work 125

Chapter 7

References 127

Appendix A 132

Appendix B 134

List of Figures

Figure 1-1: Exelon toxic greenhouse gas emissions[2] 2

Figure 1-2: Adsorption process diagram[5]. 3

Figure 1-3: Gemini PSA system developed by Air Products[7]. 5

Figure 1-4: Composite membrane[5]. 6

Figure 1-5: Zeolite framework[10]. 8

Figure 1-6: The PXRD (top image) and TGA (bottom image) of MCM-41[13] 10

Figure 1-7: SEM micrograph of MCM-41[13]. 11

Figure 1-8: Compounds for porous extended solids[14]. 12

Figure 1-9: Crystal structure of $MnGe_4S_{10}{\cdot}2(CH_3)_4N$[14]. 13

Figure 1-10: An example of assembling MOFs by using SBUs[15]. 14

Figure 1-11: MOF-3 unit cell of the crystal structure[15]. 16

Figure 1-12: MOF-5[17]. 17

Figure 1-13: Selective guest binding in a Zn (II) -BTC network[19]. 18

Figure 1-14: MOF-177[18]. 19
Figure 1-15: MOF-200[18]. 20
Figure 1-16: A paddlewheel structure.[20,21] 21
Figure 1-17: MOFs part of the MIL series[16]. 22
Figure 1-18: HKUST-1 unit cell viewing an 18Å diameter pore[23] 23
Figure 1-19: HKUST-1 reactive seeding methodology[26]. 25
Figure 1-20: Mechanochemical reaction of CPL-1[27]. 27
Figure 2-1: Hofmann complex[24]. 29
Figure 2-2: Tetrahedral unit cell with black sticks highlighted to form cavity.[24] 30
Figure 2-3: Asymmetric unit of $[Cu(4\text{-},4'\text{-bpy})_{1.5}](NO_3)\cdot(H_2O)_{1.25}$ 33
Figure 2-4: Image showing linking strut, node, and net examples.[30] 34
Figure 2-5: Interpenetrating networks[31]. 35
Figure 2-6: Mg-MOF-74[3]. 36
Figure 2-7: Mg trimer linked MOF[36]. 39
Figure 2-8: Sulfonyl dibenzoic acid. 40
Figure 2-9: π-π stacking interactions between the bipyridine molecules[38]. 40
Figure 2-10: Teflon liner (left) and stainless-steel vessel (right)[42]. 44
Figure 3-1: Schematic representation of a Bragg-Brentano diffractometer[44]. 46
Figure 3-2: Unit cell window with active data collection running[45] 48
Figure 3-3: Interaction volume tear drop[44] 49
Figure 5-1: Molecular structure of [1] with 50% thermal ellipsoids. 67
Figure 5-2: Packed cell of [1] along the c*-axis (50% thermal ellipsoids). 70
Figure 5-3: Packed cell of [1] with view along c*-axis. 71
Figure 5-4: Molecular structure with organic linker angle measurements 71
Figure 5-5: SEM images of material [1] with visible channels 73
Figure 5-6: SEM image of [1], with a magnification of 1000X. 73
Figure 5-7: EDS spectra of [1] 75
Figure 5-8: Simulated (top) and actual (bottom) PXRD of [1]. 76
Figure 5-9: TGA of [1]. 77
Figure 5-10: Molecular structure of [2] with 50% thermal ellipsoids. 79
Figure 5-11: Extended structure of [2] along the c*-axis (50% thermal ellipsoids). 81

Figure 5-12: Packed cell of [2] with view along c*-axis (left) and then the dihedral angles in the unit cell of [2] with thermal ellipsoids at 50% (right). 82
Figure 5-13: SEM images of [2]. 83
Figure 5-14: EDS spectra of [2]. 84
Figure 5-15: Simulated (top) and actual (bottom) PXRD of [2]. 85
Figure 5-16: TGA of [2]. 86
Figure 5-17: Molecular structure of [3] with 50% thermal ellipsoids. 88
Figure 5-18: Extended structure of [3] along the c*-axis (50% thermal ellipsoids). 90
Figure 5-19: Packed cell of [3] with view along c*-axis. 90
Figure 5-20: Molecular structure showing dihedral angles of [3]. 91
Figure 5-21: Molecular structure of [4] with no disorder 93
Figure 5-22: Extended structure of [2] along the c*-axis 96
Figure 5-23: Dihedral angles in unit cell of [4] with thermal ellipsoids at 50%. 97
Figure 5-24: SEM images of [4]. 98
Figure 5-25: SEM images of [4] macro-voids. 98
Figure 5-26: EDS spectra of [4]. 99
Figure 5-27: Simulated (top) and actual (bottom) PXRD of [4]. 100
Figure 5-28: Elemental mapping images of [4]. 102
Figure 5-29: TGA of [4]. 103
Figure 5-30: Molecular structure of [5] 105
Figure 5-31: SEM images of [5] at 185X magnification. 106
Figure 5-32: SEM images of [5] material at 540X magnification. 106
Figure 5-33: SEM images of [5] at 1860X magnification. 107
Figure 5-34: EDS Spectra of [5]. 108
Figure 5-35: Simulated PXRDs of [5] at two different phases. 109
Figure 5-36: SEM images of [6] 110
Figure 5-37: EDS spectrum of Ball Mill Product, [6]. 111
Figure 5-38: Actual PXRD of Ball Mill Product, [6]. 112
Figure 5-39: Elemental maps of the cross section of Ball Milled Product [6]. 113
Figure 5-40: TGA of [6]. 114
Figure 5-41: Alumina pellet before and after the reaction with [1] 115

Figure 5-42: Alumina pellet before (a) and after the reaction (b).....115
Figure 5-43: EDS spectra of [1] onto Al_2O_3 Pellet. 116
Figure 5-44: PXRD of Alumina Pellet.....117
Figure 5-45: Elemental Maps of [1] on alumina support.....120
Figure 6-1: Left image is of HKUST-1 support from Nan et al.[26] and right image is the alumina support at 50X.....123

List of Tables

Table 1-1: Comparison of CO_2 Adsorption in MOFs[16] 24
Table 2-1: Solubility chart of 4,4'-Sulfonyldibenzoic acid 42
Table 5-1: Summary of products 65
Table 5-2: Selected Bond Lengths (Å) and Angles (°) for [1].....69
Table 5-3: Dihedral Angles of [1].....72
Table 5-4: Selected Bond Lengths (Å) and Angles (°) for [2].....80
Table 5-5: Dihedral angles of [2].....82
Table 5-6: Selected Bond Lengths (Å) and Angles (°) for [3].....84
Table 5-7: Dihedral angles of [3].....91
Table 5-8: Selected Bond Lengths (Å) and Angles (°) for [4].....95
Table 5-9: Dihedral and Torsion Angles of [4]. 97
Table Appendix B: Solubility Charts of Solvents.....133

List of Schemes

Scheme 2-1: Reaction and formation of cadmium porous organic framework. 31
Scheme 2-2: Extended framework formation[24.] 32
Scheme 2-3: Formation of MOF with solvent. 38
Scheme 2-4: Predicted MOF synthesis. 41
Scheme 2-5: Theoretical reaction with SDBA and metal magnesium salt. 42
Scheme 2-6: Proposed reaction with DMF as solvent. 42
Scheme 2-7: Predicted synthesis with 4,4- bipyridine as weak base. 44

Scheme 5-1: Schematic representation of selected binding modes of carboxylate ligands 64
Scheme 5-2: Synthesis of [1] 66
Scheme 5-3: Synthesis of [2] 78
Scheme 5-4: Synthesis of [3] 87
Scheme 5-5: Synthesis of [4] 92
Scheme 5-6: Synthesis of [5] 104

List of Abbreviations

Å	Ångstrom
α	Alpha, angle
θ	Theta, Angle of Incidence
β	Beta, angle
a, b, c	Cell parameters
A, B, C	End centered unit cell type
AGR	Acid Gas Removal
AC	Activated Carbon
a.u.	Atomic units
Bar	Unit of pressure equaled to 1 atmosphere
BBC	4,4′,4″-[benzene-1,3,5-triyl-tris(benzene-4,1-diyl)] tribenzoate
BTB	4,4′,44″-benzene-1,3,5-triyl-tribenzoate
BDC	Benzenedicarboxylate
BTC	Benzenetricarboxylate
Bpy	Bipyridine
BET	Brunauer Emmett-Teller
cm	Centimeters
cm^{-1}	Reciprocal centimeters, wavenumbers
cm^3	Centimeters cubed, volume

CNT	Carbon Nanotube
cps	Counts per second
CPL	Coordination pillared layer
°C	Degrees Celsius
di-	Two
d	Distance
DHTP	2,5-dihydroxyterephthalic acid
DHTA	dihydroxyterephthalic acid
DMF	N,N'-dimethylformamide
eV	Electron Volts
E	Energy
EDS	Energy dispersive X-ray spectroscopy
υ	Nu, Frequency
γ	Gamma, angle
g	Grams or gas
h	Plank's constant
$h\upsilon$	Energy
hkl	Miller indicies
I	Intensity
I_o	Intensity of incident X-ray beam
J	Joule
K	Kelvin
k	Kilo
kV	Kilovolt
KE	Kinetic Energy
LNG	Liquefied Natural Gas
μ	Mu, linear absorption coefficient
μm	Micrometer
m	Meter
mm	Millimeter

M	Metal atom (Co, Cu, Ti)
MEA	Monoethanolamine
mL	Milliliters
M-O-C	Metal-Oxygen-Carbon
MOF	Metal Organic Framework
mol	Mole
mmol	Millimole
NMR	Nuclear magnetic resonance
nm	Nanometer
O^-	Oxide
P	Primitive unit cell type
Poly-	Many
PCP	Porous coordination polymer
ppm	Parts per million
psi	Pounds per square inch
PSA	Pressure Swing Adsorption
SBU	Secondary building unit
SEI	Secondary electron images
SEM	Scanning electron microscopy
SDBA	4-4'sulfonyl dibenzoic acid
Σ	Sum of
T	Temperature
% wt	Percent weight
x	Thickness
XRD	X-ray diffraction
λ	Wavelength
ZIF	Zeolitic Imidazolate Framework
ZOL	Zeolite Organic Lattice

Chapter 1: Background

1.1. Background

The environment is continually undergoing changes due to natural earth processes. Over the past decades the general population is becoming increasingly aware of the environmental world they live in today. The goal now, is to decrease the pollutants in the air, hazardous materials, and stifling gases that are aiding in the greenhouse gas emissions. Industries are attempting to decrease their waste production by implementing new techniques and recycling methods. One example is the Apple Company; their data exceeds Energy Star specification guidelines.[1]

The power plant industry has difficulty reducing their emissions because of the constant gas stream pollution. Exelon for example, reduced their greenhouse gas emission from 8,893 to 6,600 metric tons of CO_2. The goal is to continue reducing gas waste emission with novel technology. Solar power concepts alone do not solve the elimination of all gas waste produced. SO_2 and NO_x, from gas waste, are toxic and enter the atmosphere when the power plants are producing energy. In 2009, Exelon implemented Keystone wet limestone scrubbers in all coal-fired units and in 2011 the SO_2 emissions decreased by 19.7% as indicated in Figure 1-1. Also, selective catalytic reduction system was installed in 2012 for reduction of mercury and NO_x emissions.[2]

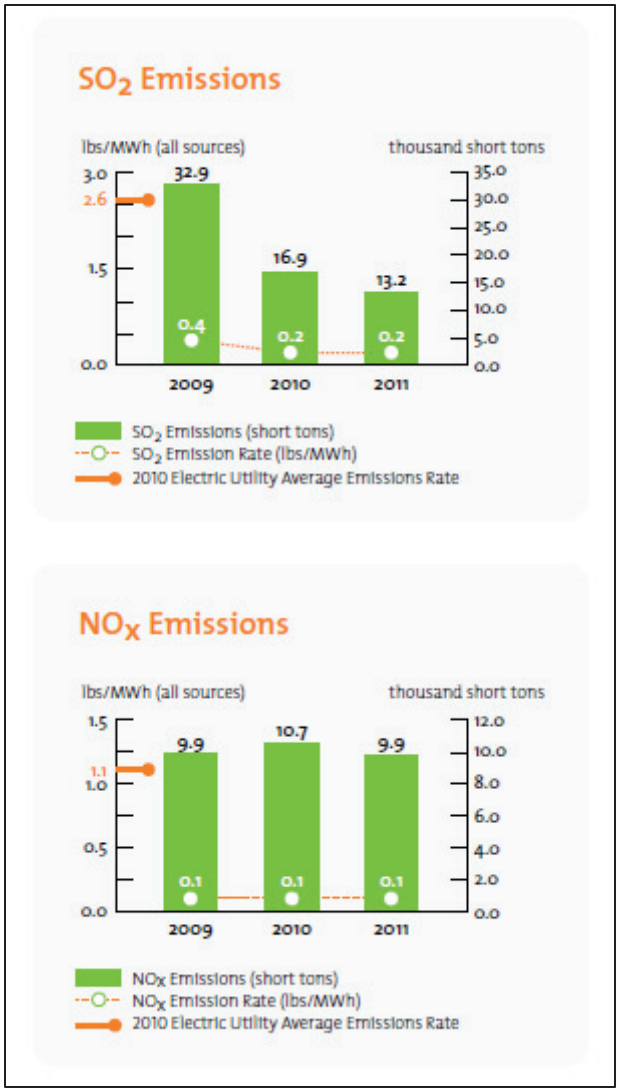

Figure 1-1: Exelon toxic greenhouse gas emissions.[2]

One possibility implemented in companies to eliminate greenhouse gases is the design of synthesized porous materials for gas adsorption. Porous materials such as metal-organic frameworks (MOFs) are now important due to their potential application. These porous crystalline solids are able to adsorb and desorb gas upon variation in temperature and pressure. As technology advances there may be a possibility to decrease toxic gas emissions in the future for a cleaner, safer, and greener society.

1.2 Application Background

How CO2 is adsorbed from a gas stream is an important issue, thus many industries and companies have included a CO2 capture process through a variety of techniques.[3] The use of porous, organic crystalline materials enhances this research dramatically; however membrane technology is mostly present in today's industries.

1.2.1 Pressure Swing Adsorption

Porous materials are used in numerous ways in industry. "(1) The purification of synthesis gas to produce hydrogen, (2) the removal of CO_2 from natural gas, and (3) the removal of CO_2 from flue gases produced by the combustion process (post-combustion CO_2 capture)" stated in *Metal Organic Frameworks: Application from Catalysis to Gas Storage* by David Farrusseng *et al.* (page 102).[4] First utilized in the 1950s by Air Liquide and Esso, and then in the 1970s after the oil crisis, pressure swing adsorption (PSA) is a typical gas adsorption process, shown in Figure 1-2, and is used in today's industries.

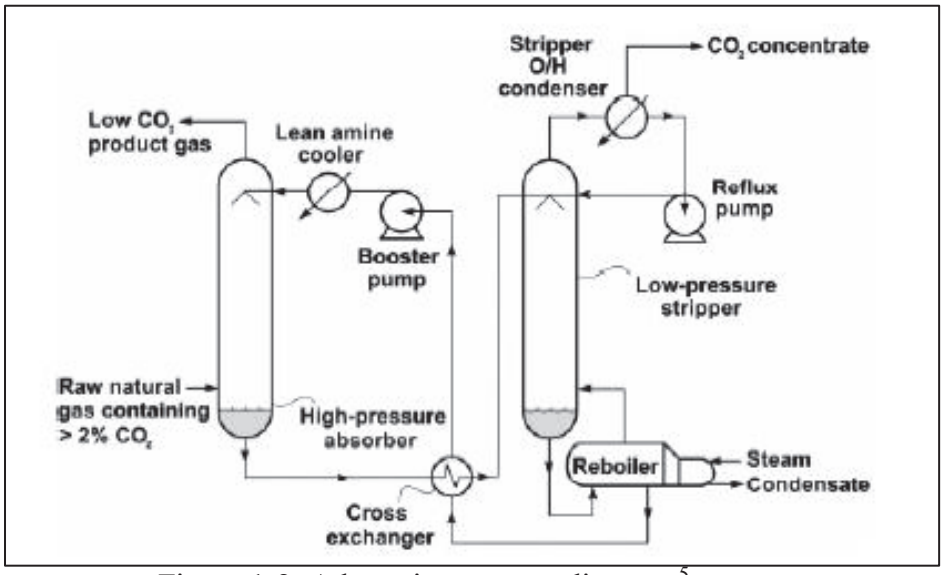

Figure 1-2: Adsorption process diagram.[5]

The PSA process separates a synthesis gas (syngas) mixture by incorporating two basic steps and two operating towers. The first step is in tower one, the adsorption step,

which involves high pressure, adsorbent liquid, and contains the natural gas. The *raffinate* is the natural gas which is recovered from the feed mixture.[4] Then, desorption or regeneration step, occurs in tower two, and the projected gases are captured for further use. The CO_2 gas caught in the second tower is from the adsorbent liquid. The liquid is condensed, leaving only the gas molecules that are caught and released. The second tower heats elements and separates gas at a lower pressure.

The PSA method is a fast process compared to the other methods. A disadvantage of PSA is its limitations on how much pure gas can be produced. Only 70-90% pure gas will come out of the PSA procedure, most of which is hydrogen. The rest of the gases in the stream mixture are still going into the atmosphere.[4] The goal is to be able to capture the gases that are released. Due to the recovery of H_2 gas, the PSA process produces large amounts of CO_2 as a byproduct, which is released into the atmosphere. It is suggested that the CO_2 be removed from the gas stream, which will start recycling gas waste emissions.

At present, specific gases are being adsorbed via amines or glycol derivatives for the selective adsorbance of CO_2. Also a variety of gases are adsorbed using amine adsorption technology, involving CO_2 through plants. It is suggested that amine plants do well in a low concentrated gas system, and membrane plants work well in a high concentrated gas system. In membrane plant systems, cellulose acetate is used for adequate adsorption, but researchers have found that polymers show decent CO_2 adsorption, at a lower cost.[6] The membrane plant results in a negative environmental impact because of the regeneration of high temperatures and the large amount of water that needs to be recycled. New technology is constantly improving the cost of adsorption,

separation, and maintenance. For instance, researchers have developed a PSA process called Gemini, Figure 1-3. The process includes two types of adsorbent beds that work simultaneously producing two pure streams of gas: CO_2 and H_2. The feed mixture moves into the A-bed adsorbents and CO_2 is removed. The CO_2 is depressurized with a purge column and recycled back into the A-beds to remove all the lighter impurities. At the same time the B-beds are working in the same way as a normal PSA system would, but recovers H_2 as the pure gas.[4,7]

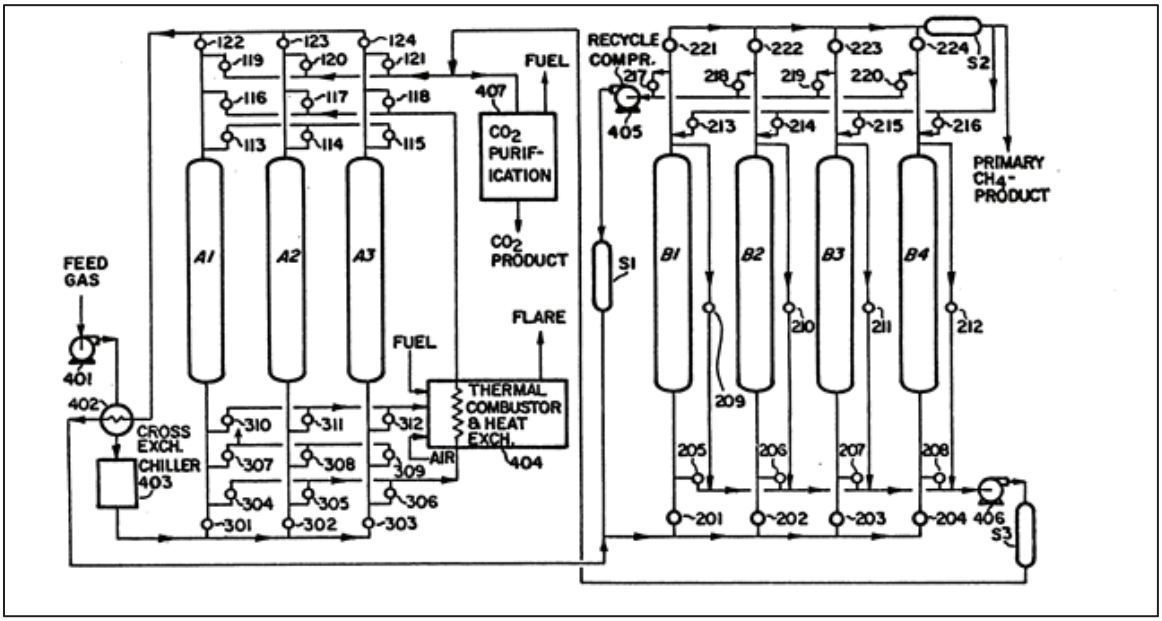

Figure: 1-3 Gemini PSA system developed by Air Products.[7]

1.2.2 Composite Technology vs. Carbon Absorbers

Natural raw gas contains toxic impurities i.e. dihydrogen sulfide, and to remove pure CO_2 from the raw gas, different adsorption techniques other than PSA must be implemented. In a process called acid gas removal (AGR) H_2S and CO_2 are removed first by a chemi- or physisorption. In a physisorption process most of the H_2S and CO_2 are dissolved into the solvent. When the H_2S and the CO_2 is extracted from the raw gas

liquefied natural gas (LNG) can be produced because the gas can now safely attain higher temperatures.[4]

Another way that CO_2 can be removed from LNG is with a composite membrane, which involves a porous support layer as well as an adsorbant layer, Figure 1-4. These membranes have observed mechanical strength, but the synthesis is expensive. It is proposed that simple polymers be placed in large stainless-steel vessels, or membrane modules, much more gas can be captured at one time. Since fewer membranes are being produced, it becomes more cost effective.[5]

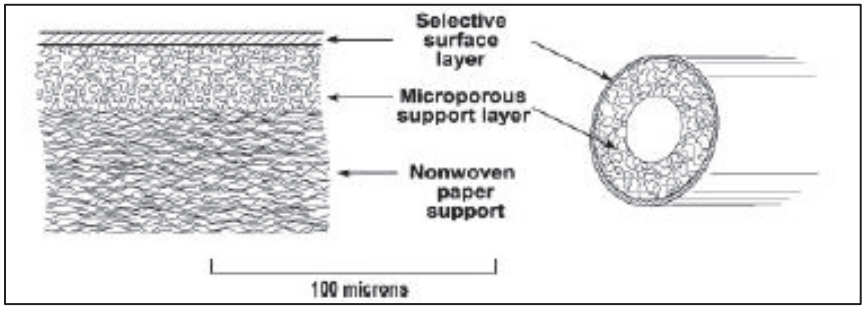

Figure 1-4: Composite membrane.[5]

As technology progresses, new methods of CO_2 adsorption have evolved which include, activated-carbon-based solid sorbents, carbon molecular sieves, and carbon-nanotube-based solid sorbents. As activated carbons (ACs) are applied in the industry, the PSA process can still be used to remove CO_2 from gas streams along with molecular sieves for purification. Carbon molecular sieves possess a small pore size distribution, which result in adsorption selectivity and capacity. Carbon nanotubes (CNTs) can be a considerable candidate for CO_2 adsorption due to their slightly larger pore size and sufficient stability. Sauata *et al.* found that single-walled CNTs can adsorb twice that of regular ACs, but raw CNTs adsorb much less CO_2 than ACs at room temperature. Among

the available adsorption techniques however, CNTs have so far demonstrated the highest selectivity for CO_2.[8]

Flue gas is the stream of gas that is released from the chimney stacks at power plants. The steam is a mixture of pure gases that are released into the atmosphere. From the flue gas stream CO_2 can be captured by utilizing *post-combustion CO_2 capture*.[4] Systems that are hypothesized and tested include the adsorption of CO_2 by monoethanolamine (MEA), absorption chilled ammonia, high-temperature carbonation-decarbonation cycles, etc. The tests employing these systems did not meet the standard requirements of the Department of Energy and are not implemented commercially. The discovery of commercially producible MOFs will eliminate the use of fossil fuels for energy production, and will allow an increase in the overall renewable energy mix, along with an increase in energy effectiveness.[4]

1.2.3 Zeolites

To meet the requirements of the Department of Energy, a material is needed with better adsorption capacity and stability at different temperatures and pressures. Research on CO_2 adsorption produced microporous crystalline framework materials, such as zeolites. Zeolites are known for having uniform crystalline pore sizes, and an affinity for gas adsorption. The framework contains silicon or aluminum, along with other metals that can give the overall structure a negative charge. Zeolites possess cations, i.e. sodium, Na^+, in the pores of the structure balancing the charge, but these cations can be removed and replaced by gases.[9] The pore size of the zeolites selects the gas molecule that can fit into the pore, and depending on the structure and stability of the framework, the gas can

be desorbed and recycled. There are many different types of zeolites synthetically and naturally made, and they show promise regarding CO_2 adsorption.[9]

An interesting example is a zeolite with an organic group as the lattice (ZOL), which is a new type of organic-inorganic zeolite containing an organic framework.[10] ZOLs are synthesized from organosilane and have a methylene group bridging the silicon atoms. The silicon atoms are being held together in the structure by bridging oxygen atoms forming a zeolitic framework, Figure 1-5. By adding these organic linkers of methylene or biphenylene, there is more porosity throughout the zeolite.

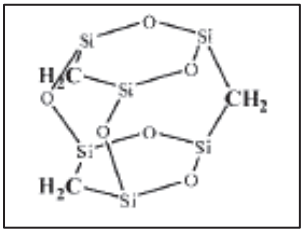

Figure 1-5: Zeolite framework.[10]

The development of new materials, allows new methods to be tested on gas adsorption. Zeolitic imidazolate frameworks (ZIF)s are comparable to zeolites, having a Metal-Imidazole-Metal (angle 145°) structural shape, as a zeolite has a Silicon-Oxygen-Silicon shape in its structure.[11] ZIFs and Metal-Organic Framework (MOF) materials are quite similar in their physique. Since these materials are closely related, it has opened up the synthetic world to numerous novel possibilities.

1.2.4 Mesoporous Materials

In the early 1990s mesoporous materials were greatly studied. One of the companies that conducted this type of synthesis was the former Mobil Oil Company, and they referred to their new materials as the M41S family. The family of materials involved, MCM-41, MCM-48, and MCM-50, were silicate-based materials structurally

similar to zeolite materials; the only difference was that they contained cationic surfactants. The M41S family had pores over 1000 m^2/g in volume, exhibit different dimensions. MCM-41 was a 1-D framework that had parallel channels, while MCM-48 was a 3-D framework with intriguing porosity that made it a catalytic pursued framework.[12]

Materials Research from São Carlos completed a full characterization on MCM-41.[13] Rogério A.A. Melo *et al*. focused on the hydrothermal synthesis difficulty, stability, and adsorption. MCM-41 was determined to have hexagonally arranged channels that exhibit a pore size of 15-100Å, had good stability at high temperatures ranging from 285-400°C, and interesting hydrophobicity and acidity, which made it a promising material in catalysis, ion exchange, etc. The powder x-ray diffraction and TGA analysis are shown in Figure 1-6. Also, Rogério A.A. Melo *et al.* were able to achieve an SEM image of the material, Figure 1-7, giving a close up image of MCM-41. The image revealed that the material contains agglomerates of crystals which were due to the high pressure that occurred in the autoclave during synthesis.

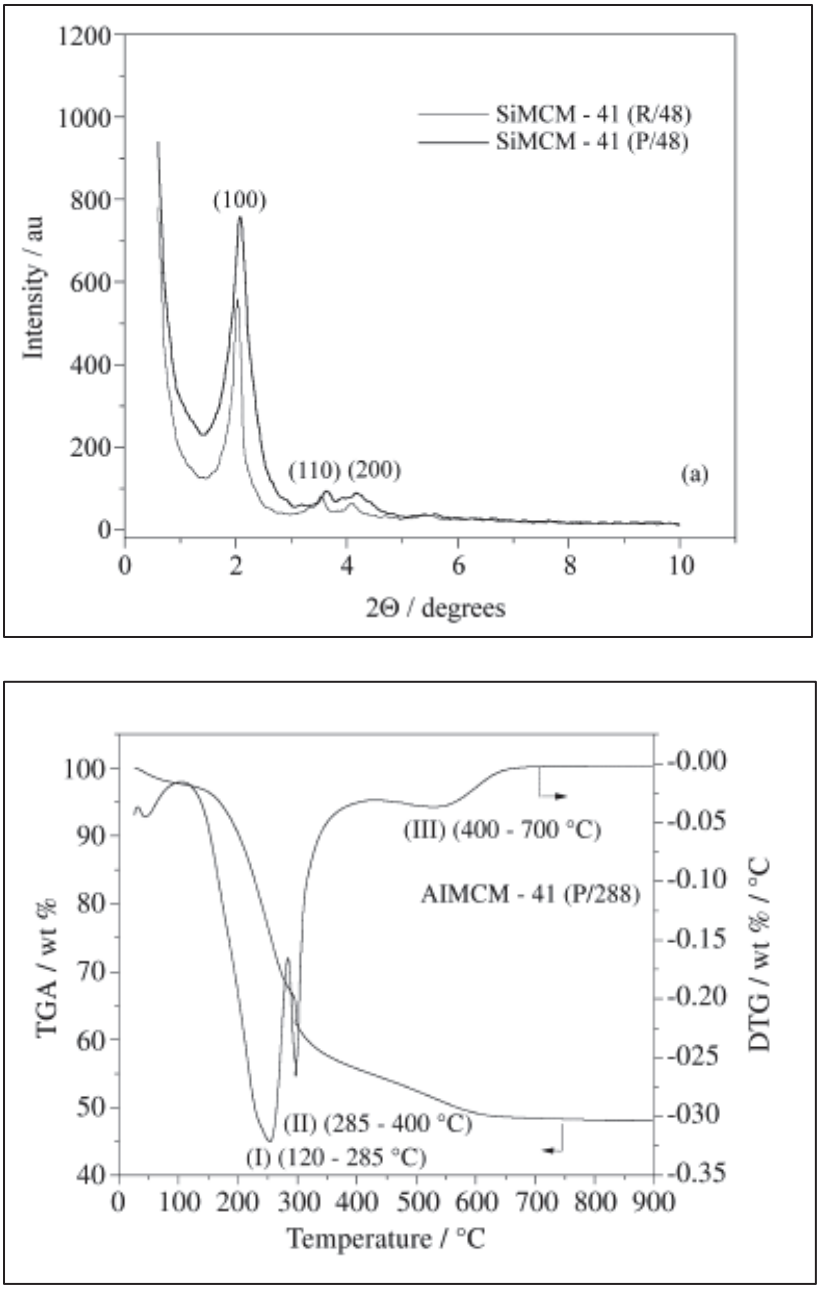

Figure 1-6: The PXRD (top image) and TGA (bottom image) of MCM-41.[13]

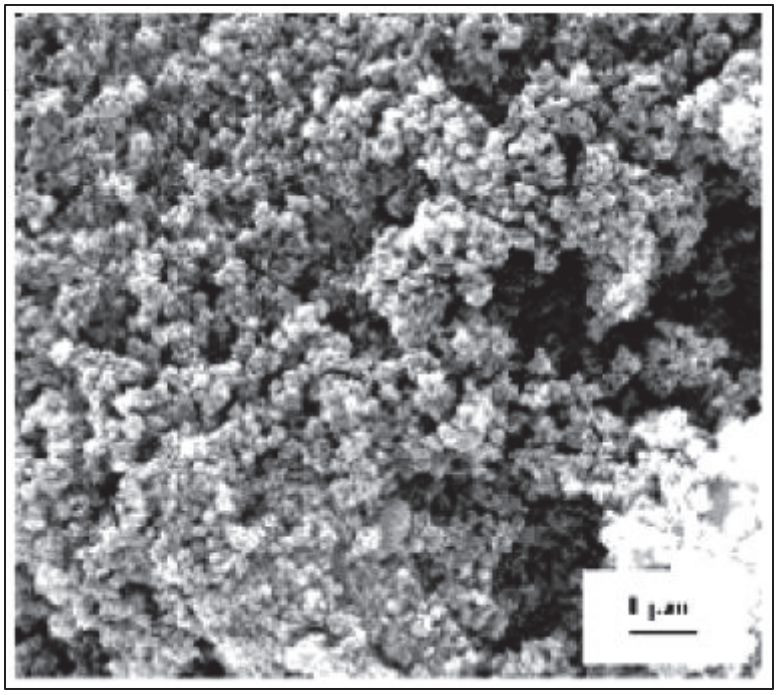

Figure 1-7: SEM micrograph of MCM-41.[13]

1.3 Types of Frameworks

Omar M. Yaghi, a chemistry professor from UCLA, and his research team synthesized the first MOF in the 1990s. The MOF was able to retain water molecules and nitrate anions. The tremendous research by him resulted in many new MOFs with interesting properties especially for gas adsorption. In order to comprehend the complex three dimensional frameworks, the theory of secondary building units (SBUs) were developed.

1.3.1 Open Metal/Extended Frameworks

In 1998 Yaghi *et al.* published a review called "*Synthetic Strategies, Structure, Patterns, and Emerging Properties in the Chemistry of Modular Porous Solids*."[14] The review discussed porous frameworks, extended solids, etc. in great detail. It stated the challenges in producing such materials and introduces a program that is aimed at

producing materials that link inorganic clusters and organic molecules to metal ions, Figure 1-8.

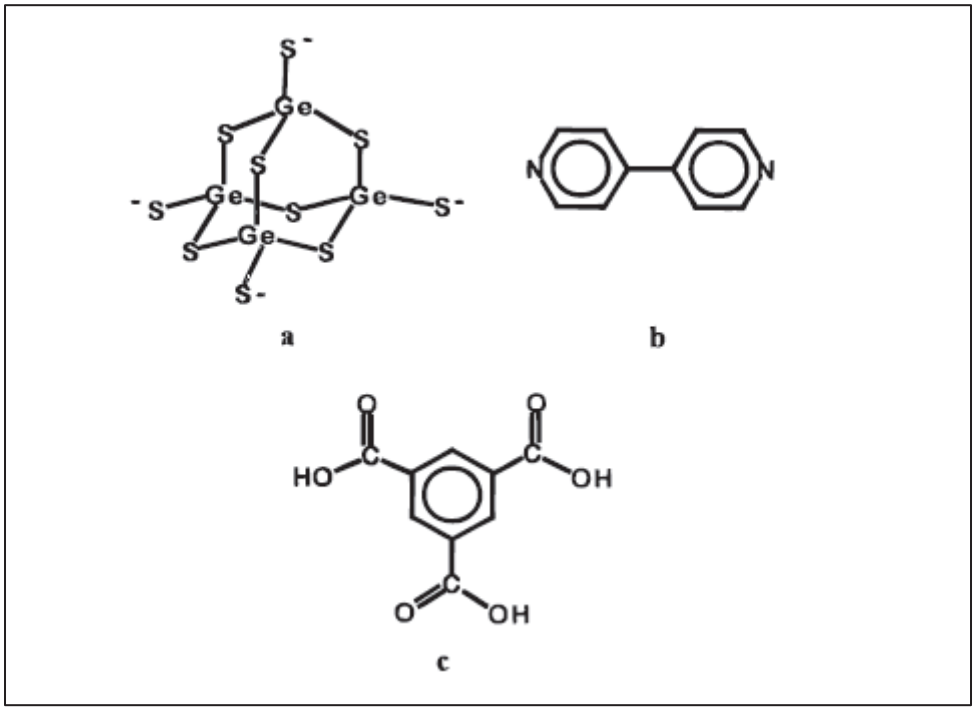

Figure 1-8: Compounds for porous extended solids.[14]

Yaghi *et al.* attempted several synthetic strategies for producing crystals including, diffusion and solvothermal techniques, which would give rigid porous frameworks that were able to adsorb and desorb guest molecules without collapsing or de-solvation. Yaghi *et al.* also made an effort to combine two different compounds, $Mn(CH_3CO_2)_2{\cdot}4H_2O$ and $Ge_4S_{10}[(CH_3)_4N]_4$ to make three dimensional porous frameworks, $MnGe_4S_{10}{\cdot}2(CH_3)_4N$ (Figure 1-9). Yaghi suggested a novel method for producing porous materials for catalysis and anion exchange, selective separations, and for site bonding.[14]

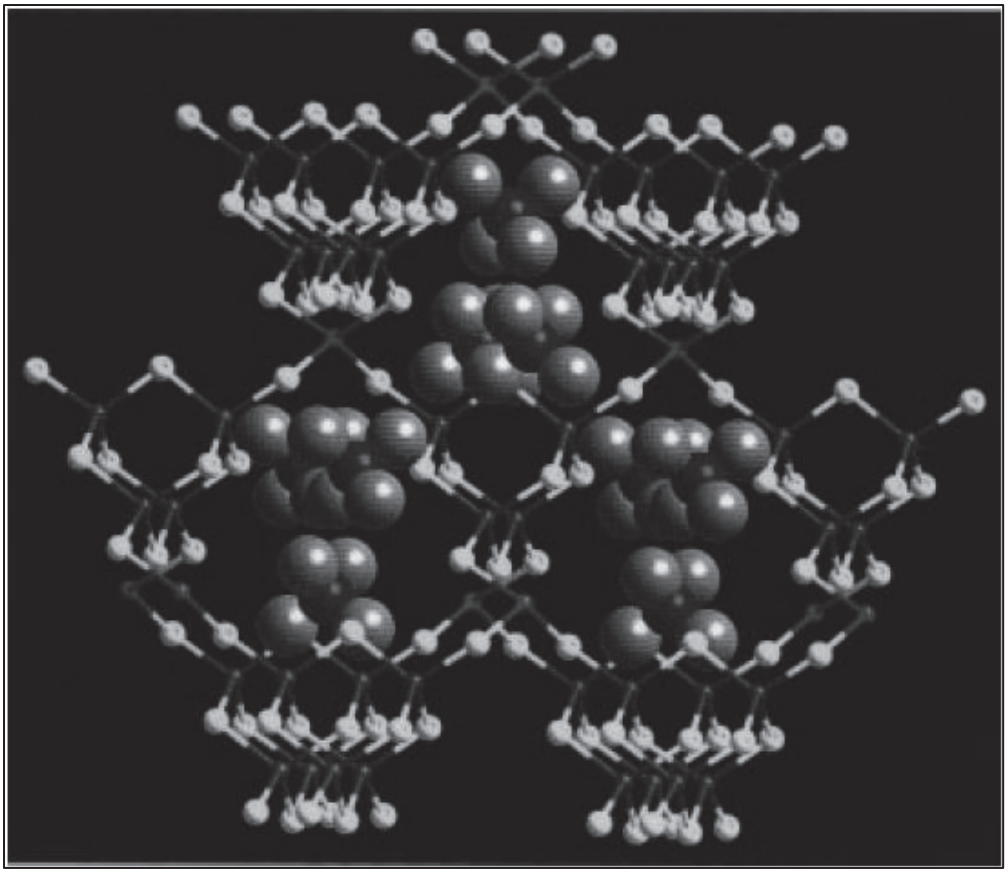

Figure 1-9: Crystal structure of $MnGe_4S_{10}{\cdot}2(CH_3)_4N$. The large tetramethylammonium cations occupy the pores in the 3-D framework.[14]

In 2001, Yaghi *et al.* published a second review, *"Modular Chemistry: Secondary Building Units as a Basis for the Design of Highly Porous and Robust Metal-Organic Carboxylate Frameworks."*[15] The review focused on the assembly of porous organic frameworks using the application of secondary building units (SBUs) to understand the topology of the structures. A product can be predicted by choosing a specific carboxylate ligand to connect with a specific fragment, which can become a large porous entity.

Most molecular complexes, specifically ones that contain carboxylates, can be combined with a metal cation to form an extended solid, Figure 1-10. Carboxylates are utilized in a synthesis because of their rigidity that occurs when they link to metal ions,

resulting in an M-O-C cluster formation. The framework crystallizes in such a way that the metal is locked in between the available carboxylate, and forms a stable extended framework. Also, the frameworks can become large in size because of the lengthy carboxylates that are used. It all depends on the length of the linker and the voids in the framework, which are proportional to the sequence of bonds that are used; a process called *expansion.*[15] In Figure 1-10, the bipyridine is reacts with a metal to create a molecular complex, which reacts with another complex. The molecular complexes form an expanded framework.

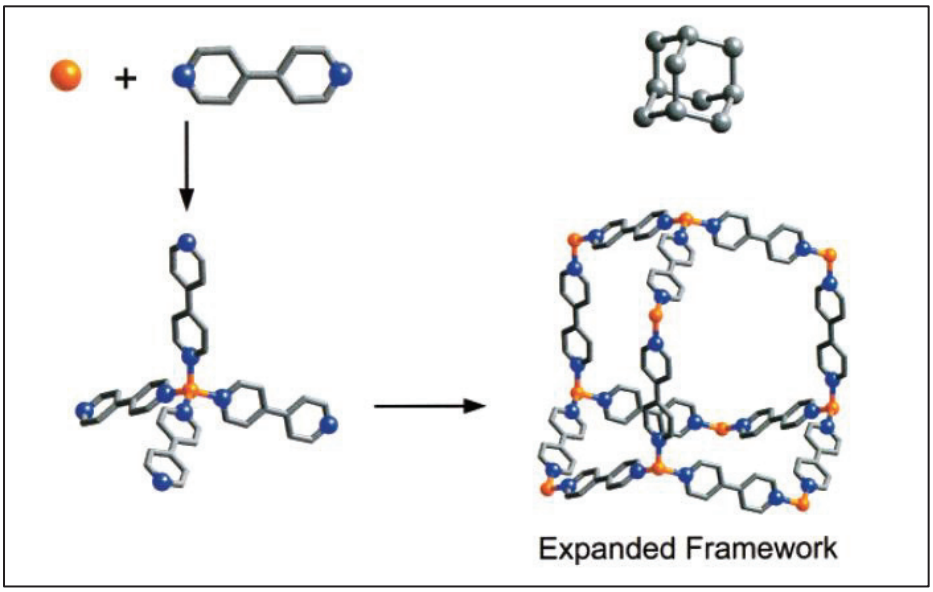

Figure 1-10: An example of assembling MOFs by using SBUs.[15]

Many MOFs have been produced, but most are not useful for potential applications. It is necessary to scale the reactions up to industrial size and the volatility of the solvents may be harmful to humans due to inhalation or ingestion, making the workplace unsafe. Most frameworks easily collapse when avoiding interpenetration and when heating up the MOF to release the solvent molecules.

Normally the structures made from the SBUs contain solvent molecules because the compounds will bond where ever there is available space, intercalation.[16] If the solvent molecule used in the reaction has weak ligand interaction, it is possible that the ligands can be removed and the frameworks not collapse. When producing MOFs, the reaction might occur at room temperature with a simple crystallization technique. One of the techniques used for MOF crystallization is diffusion and nucleation. For diffusion, the reaction mixture sits and a weak basic solution is slowly diffused into the mixture deprotonating the carboxylate and starting MOF formation, resulting in crystallization. Nucleation is the production of a crystal as it diffuses.[15] Once the crystallization technique is complete, stabilization of the framework needs to be retained as the solvent is removed. Then a successful MOF, which can be commercially applied, has been produced. One example discovered by Yaghi *et al.* is MOF-3, $Zn_3(BDC)_3 \cdot 6CH_3OH$, BDC = 1,4-benzene dicarboxylate, Figure 1-11. When methanol, which is the solvent, has been fully removed from the structure, the framework keeps its integrity and the product is a porous network.

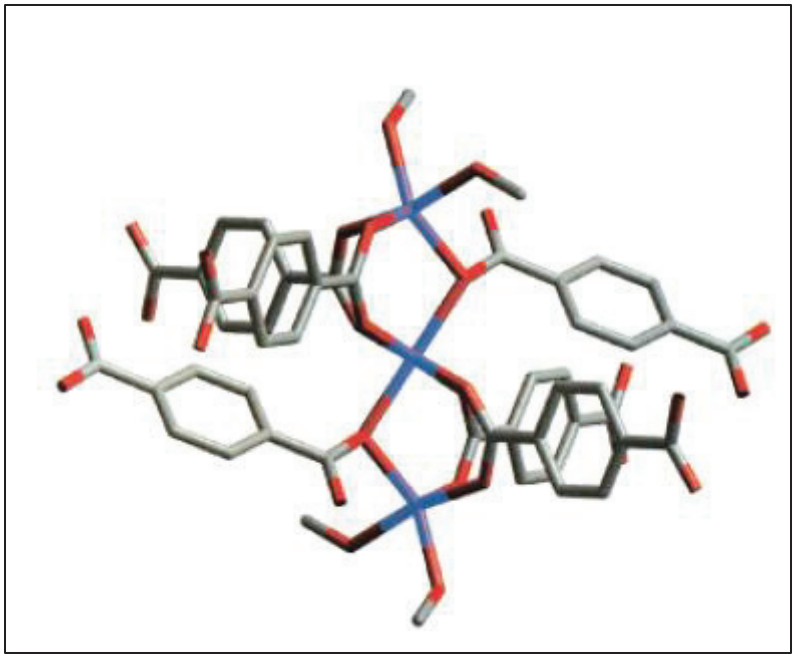

Figure 1-11: MOF-3 unit cell of the crystal structure.[15]

1.3.2 Frameworks with High Surface Areas (BETs)

When producing MOFs it is suggested to keep the density of the material low. In general, MOFs should be stable in many environments. Figure 1-12 shows an example of a known metal-organic framework, MOF-5, an important material that was produced by Omar M. Yaghi *et. al* and prepared with 1,4-benzenedicarboxylate (BDC) as a linker and zinc as a metal source.[17] A void volume of 79%, a crystal density of 0.59 g/cm^3, and a Brunauer Emmett-Teller (BET) surface area of 3800 m^2/g were the characterized results. The void spaces are represented by yellow spheres.[17-18] Working with stable carboxylates as organic linking groups the MOF can remain crystalline through the process of de-solvation and heating, creating consistency throughout the reaction.

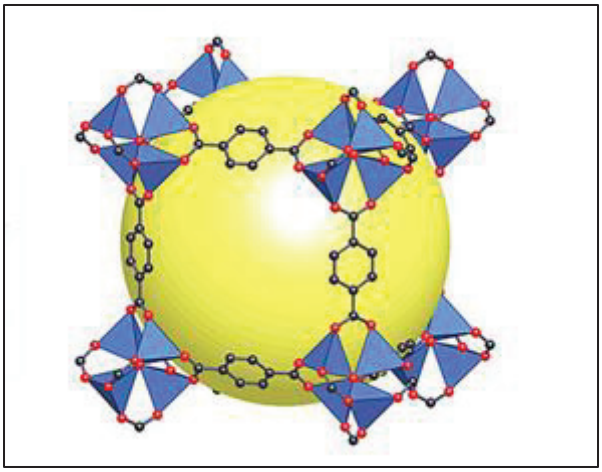

Figure 1-12: MOF-5.[17]

During the reaction the ligand binds with the metal centers, and from that the coordination complex forms. There can be a different number of geometries around the metal center, typical ones have four and six ligands, called tetrahedral and octahedral complexes, respectively. There can also be a five ligand complex called a pentahedral. MOF-5, for example, is a tetranuclear supertetrahedral cluster motif. It contains high symmetry in the crystal structure where the Zn^{2+} combines with a carboxylate and forms a well-defined unit with the oxygen as the cluster's center. The complexes have a charge that is donated from the ligand to the metal. Also, water and many basic amines have a neutral charge as a ligand, and are the molecules that will bind with the metal to form a stable complex. N,N'-dimethylformamide (DMF) and chlorobenzene were the solvents that were used in the production of MOF-5, the solvent deprotonated the organic linker and let the negative oxygen atoms combine with the positive zinc atoms.

Furthermore, Yaghi *et al.* discovered that a multitude of MOFs can be produced depending on the organic linkers and solvents that are used for the synthesis. By changing the solvent in a reaction i.e. working first with water, then pyridine and ethanol, and finally triethylamine and ethanol, different frameworks are produced, along

with different pore sizes. The goal is to achieve three-dimensional MOFs. In the MOF-4 framework, $Zn_2(BTC)$-$(NO_3)\cdot(H_2O)(C_2H_5OH)_5$, there is a cross-section of 14Å that is occupied by water and ethanol molecules. In the Zn-BTC network, Figure 1-13, it is possible to remove those water and ethanol molecules and leave a void in the crystalline structure.[19] With removal of the water and ethanol molecules the structure would have a void space of 44%, in which other gases can be adsorbed.

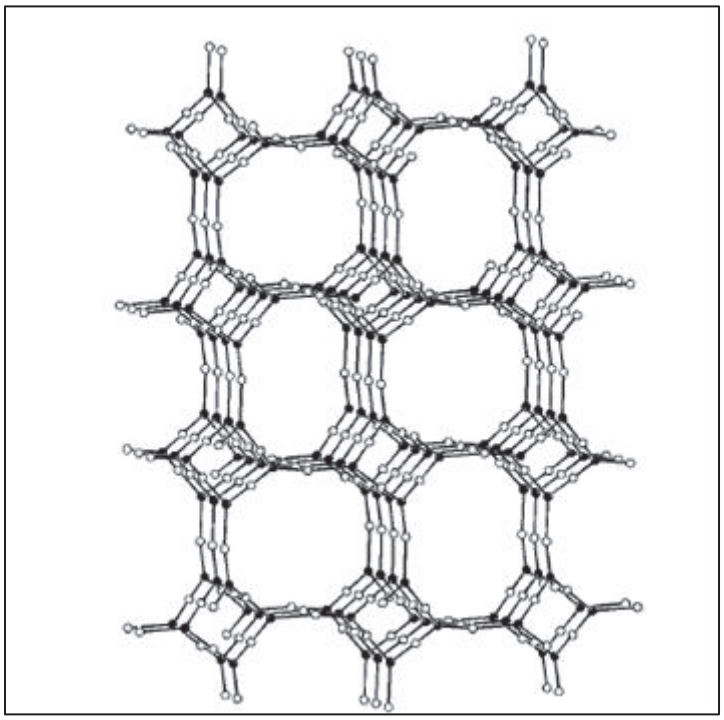

Figure 1-13: Selective guest binding in a Zn (II) -BTC network.[19]

Yaghi *et al.* hypothesized that the larger the pores in the MOF, the more gas molecules could be adsorbed. They theorized that by extending the linkers in between the metals as much as possible, they would be able to create large pores and high surface areas within the MOFs.[18] The challenges they faced were; (1) stability of the framework, because using large linkers makes the framework longer and more fragile, and (2) high

probability of interpenetration, since the space within the framework is large, it will be more susceptible to the ligands linking within each other, which consumes pore space.

Overcoming those challenges, Yaghi *et al.* created a series of MOFs, two of which are exceptionally large in porosity and surface area: MOF-177 and MOF-200, Figure 1-14 and 1-15, respectively. MOF-177 was prepared with 4,4′,44″-benzene-1,3,5-triyl-tribenzoate (BTB) as the linker creating a void volume of 83%, a crystal density of 0.43 g/cm^3, and a BET surface area of 4500 m^2/g.[23] MOF-200 was prepared with 4,4′,44″-benzene-1,3,5-triyl-tribenzoate (BTB) and 4,4′,4″-[benzene-1,3,5-triyl-tris(benzene-4,1-diyl)] tribenzoate (BBC), as the linkers, creating a void volume of 90%, a crystal density of 0.22 g/cm^3, and a BET surface area of 4530 m^2/g.[18]

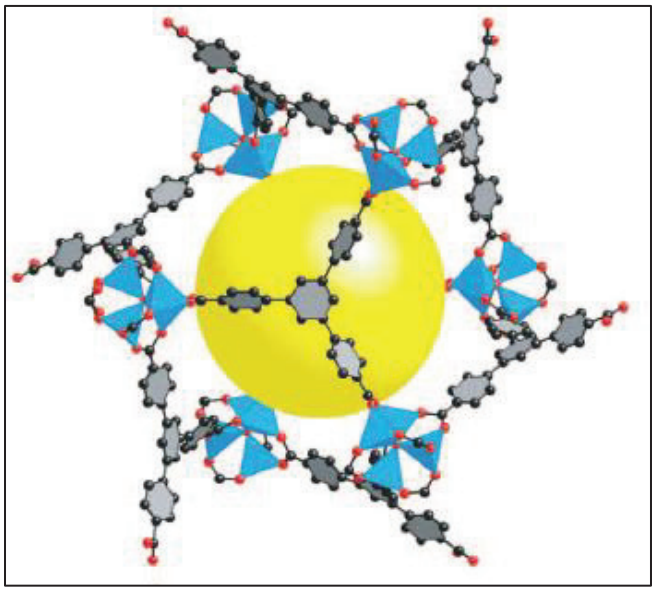

Figure 1-14: MOF-177.[18]

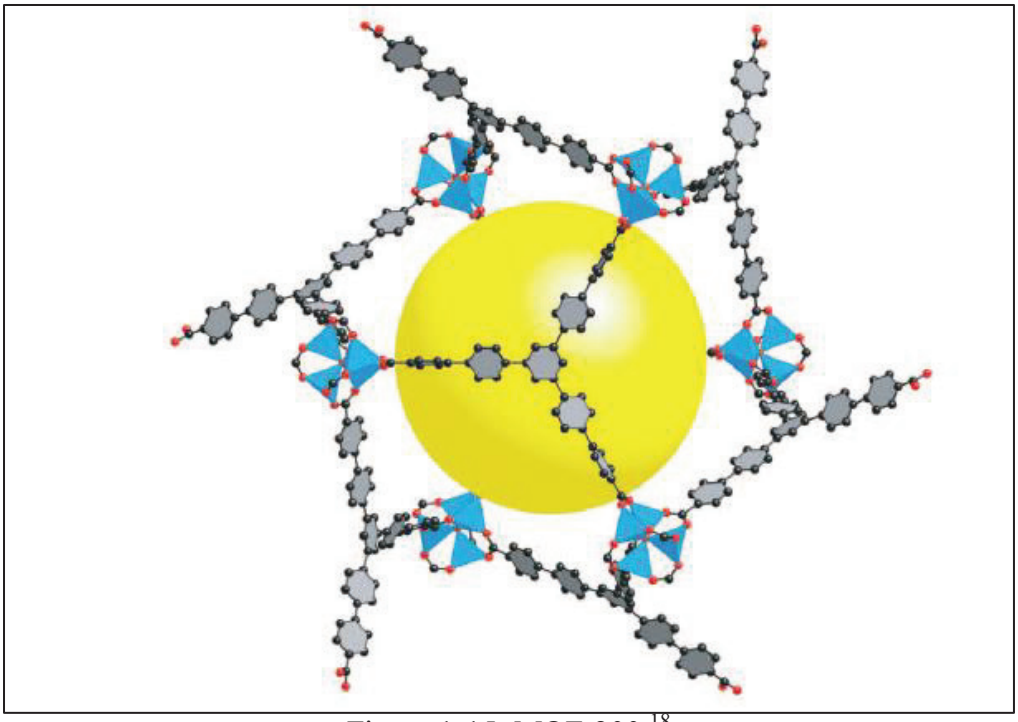

Figure 1-15: MOF-200.[18]

It is important to note that during the syntheses it was impossible to not have interpenetration within the MOFs. The difference between MOF-177 and MOF-200 is that MOF-200 contains mixed ligands: BTB and 4,4′,4″-[benzene-1,3,5-triyl-tris(benzene-4,1-diyl)] tribenzoate (BBC), which creates larger pores and a higher surface area.[18] The goal is to achieve no interpenetration in an MOF, and the MOF should be stable. Also the MOF should not collapse upon desorption of gas or applied heat.

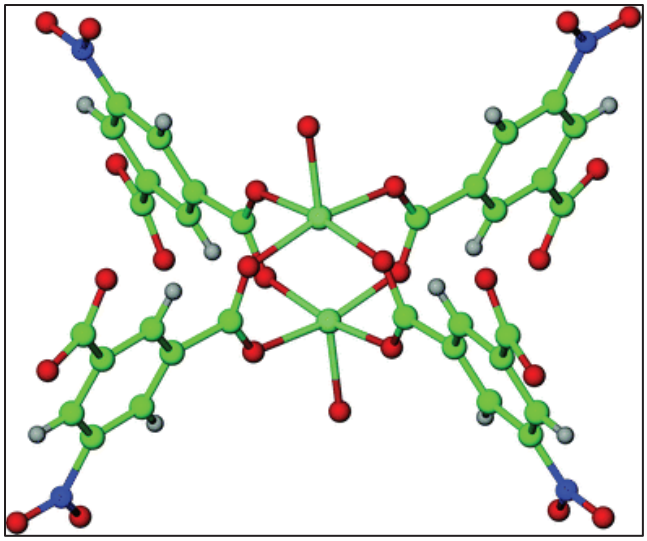

Figure 1-16: A paddlewheel structure.[20,21]

High surface area frameworks, as in "paddlewheel caged" structures, PCN-61 and PCN-66, as well as the MIL series, specifically MIL-100 and MIL-101, which are MOFs that have chromium cations as their metal centers have reasonable adsorption properties.[12,16] A paddlewheel is a cross-linking of metal-to-metal or metal-to-linker to form a hexatopic structure, Figure 1-16. They have a distinct structural topology. Based on the addition of isophthalate moieties, which are SBUs, paddle wheels are built upon one another to form cages creating large organic linkers, and results in less interpenetration and more space within the material.[22] PCN-61 and PCN-66 contain dicopper paddlewheel SBUs and have similar cage sizes, about 13Å, and have high stability due to the microporous cages.

The MIL series of MOFs use chromium as their metal cation, making the MOF unique. When chromium cations are placed with 1,3,5-benzenetricarboxylate, in a solvent, a tri-nuclear cluster [Cr_3O] with exceptionally high porosity is formed, Figure 1-17. The diameter of the pores of MIL-100 and MIL-101 are 29Å and 34Å, respectively. MIL-101 has a very large BET surface area of 4230 m^2/g, and has a hydrogen adsorption

capacity of 6.1% at 77K and 80 bar, which is of the highest recorded data for hydrogen storage. Furthermore, the CO_2 adsorption capacity for MIL-101 at 298K and 42 bar is 35 mmol/g which is the highest capacity than any MOF produced to date, including MOF-177, and that has a 33.5 mmol/g CO_2 maximum adsorption capacity.[16]

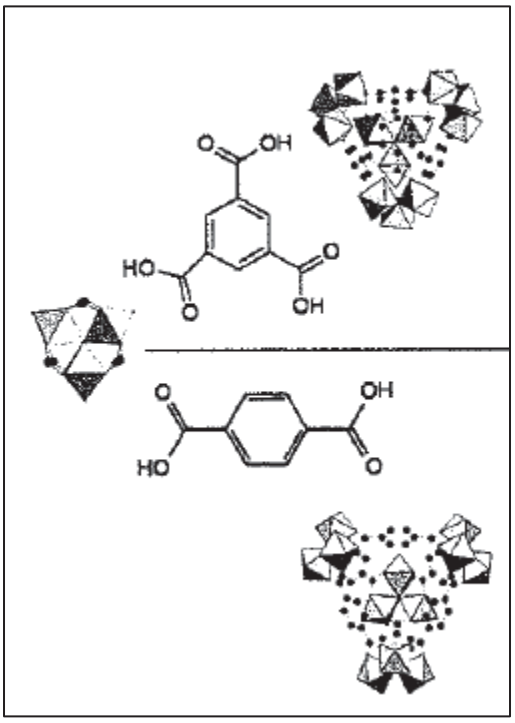

Figure 1-17: MOFs part of the MIL series. The structure of MIL-100 is shown on top and the structure of MIL-101 is shown on bottom.[16]

1.3.3 Lewis Acidic Frameworks

One of the challenges in the research is producing MOFs with good adsorption quality. Out of the hundreds of MOFs that are produced, few are able to adsorb gas or host guest molecules. In 1999, Williams *et al.* discovered a MOF that easily host guest molecules; it was through unsaturated metal Lewis acid sites in the framework. HKUST-1, $[Cu_3(btc)_2]$,btc = benzenetricarboxylate, is a porous coordination polymer (PCP) with free copper metal sites that have a positive 2+ charge and are accessible to host incoming molecules, including gas molecules, Figure 1-18. The MOF gave a BET surface area

measurement of 692.2 m^2/g, a density of 1.22 g/cm^3, and a porosity volume to be 40.7%.[23] Since the development of HKUST-1, researchers have been able to expand upon its capabilities into many areas of MOF synthesis and characterization.[4,12,16,23,24]

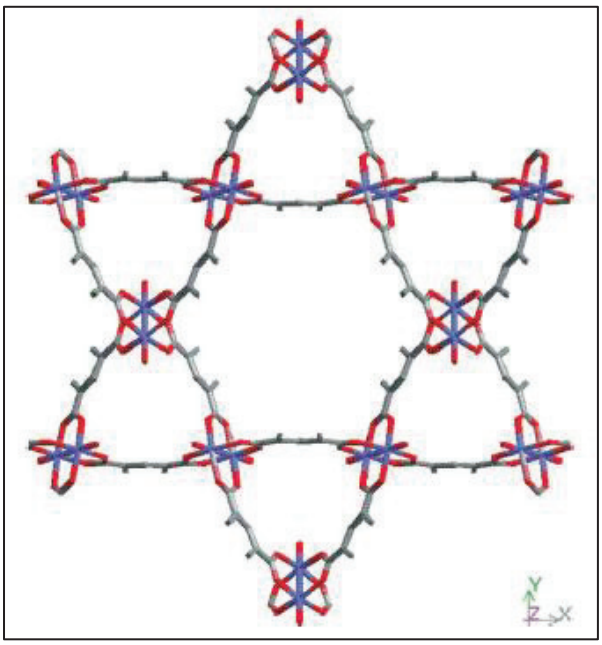

Figure 1-18: HKUST-1 unit cell viewing an 18Å diameter pore.[23]

Another example of open metal site frameworks is M_2(dhtp) (dhtp = 2,5-dihydroxyterephthalic acid; M = Mg, Mn, Co, Zn). Another paddlewheel type framework with a 2+ charge at the metal site depending on the metal cation that is present in the material. Mg_2(dhtp) shows CO_2 uptake at 298K and 1 atm of 35.2 wt%. The high percentage of CO_2 that can be adsorbed into this material is because of its lightweight and the strong interactions magnesium metal cation has with CO_2.[4] There are few MOFs that have been designed with metal cations as a Lewis acid. There is now use of post-synthetic work and grafting procedures that show promising results for catalysis and other applications.

1.3.4 MOF Table Summary

Table 1-1: Comparison of CO_2 Adsorption in MOFs.[16]

Material	BET (m^2/g)	Langmuir (m^2/g)	Volume (cm^3/g)	CO_2 at 270K (cm^3/g)	CO_2 at 298K (cm^3/g)
MOF-5	3,800	4,400	1.13	33.5	494
MOF-177	4,750	5,640	1.75		759
MIL-100	1,900		1.1		403
MIL-101	4,230		2.15		896
MIL-53(Al)		1,500			224
MIL-53(Cr)		1,500			224
HKUST-1	1,507	2,175	0.75		239
ZIF-100	595	780		38.1	
ZIF-69	950	964		69	

1.4 Aluminum Support

It is suggested that by applying a support to a MOF it will be easier to test for adsorption capacity. With the correct type of support, or planar substrate the MOF crystals or powder will bind to the support. Since some MOFs can be utilized commercially, it is necessary to have the MOF be ready for application-specified configurations. To have the MOF commercially ready for the industry, the MOF and the support are attached together through functional groups of the MOF to the support interface. The company, using the MOF will be able to use the product pre-attached to a working support. Certain MOFs are attached to a support by a seeding process.

MOFs are also attached to supports through capsules, for medical applications, MOFs acting as host matrices for nanoscale objects, composites formed in a one-pot synthesis, and MOFs grown onto 2- and 3-dimensional substrates using 'top-down' and 'bottom-up' strategies.[25] A reaction with a support will occur the same way in the solvothermal synthesis reaction, but the MOF crystals will grow on the support, which

can be aluminum, gold, etc. The MOF will grow within the pores of the support and is connected through a ligand.

One example that can be applied to MOFs for industrial gas adsorption is reported by Jiangpu Nan et al., *Step-by-Step Seeding Procedure for Preparing HKUST-1 Membrane on a porous α-Alumina* Support as mentioned above.[26] HKUST-1 was produced by using the 'top-down' and reactive seeding strategies, and can be produced on a pre-made alumina disc. The disc contains pore sizes of ca. 110 nm and about 35% porosity. Also, the seed deposition is an important part of the synthesis. During the reaction, the alumina disc is dipped into each reactant mixture for a certain amount of time, Figure 1-19. The seeding process allows each part of the MOF reactant solution to fill a part of the pores throughout the alumina disc. Then, the solvothermal reaction takes place and the HKUST-1 product crystallizes and forms on the alumina disc.

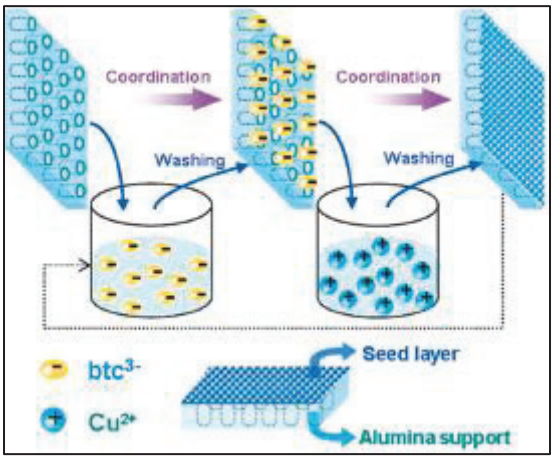

Figure 1-19: HKUST-1 reactive seeding methodology.[26]

1.5 Mechanical Synthetic Approach

Because of the difficulty of producing MOFs for commercial use, it would be necessary to attempt to discover a novel method that produces applicable results. MOFs must be able to be produced efficiently on a large industrial scale. It would not be practical to utilize solvothermal or hydrothermal synthesis, and so a more efficient method is needed, which will conserve the company's time. According to Kitagawa *et al.*, mixing materials in a mechanochemical method seems to be a promising technique.[27]

The mechanochemical synthetic method has limitations on the products that can be produced, as in no use of a solvent. Because of these limitations the MOF becomes industrialized by low cost, reducing reaction rate, etc. Kitagawa *et al.* produced a successful mechanochemical porous coordination polymer termed coordination pillared-layered (CPL) structure series, Figure 1-20. Copper is used as the metal cation, disodium pyrazine-2, 3-dicarboxylate is the organic linker, and pyrazine is used for the weak base. The reactants were added into an agate mortar and were ground with a pestle for 20 minutes. The reaction yielded a blue-greenish powder that resulted in CPL-1 after a PXRD was taken. The powder result also changes phase with humidity. During characterization of the material, adsorption of N_2 was observed. The collected data was varied in results and it was concluded that there were interstitial pores in the multicrystalline particles. For more detailed information please refer to the article, reference [27].

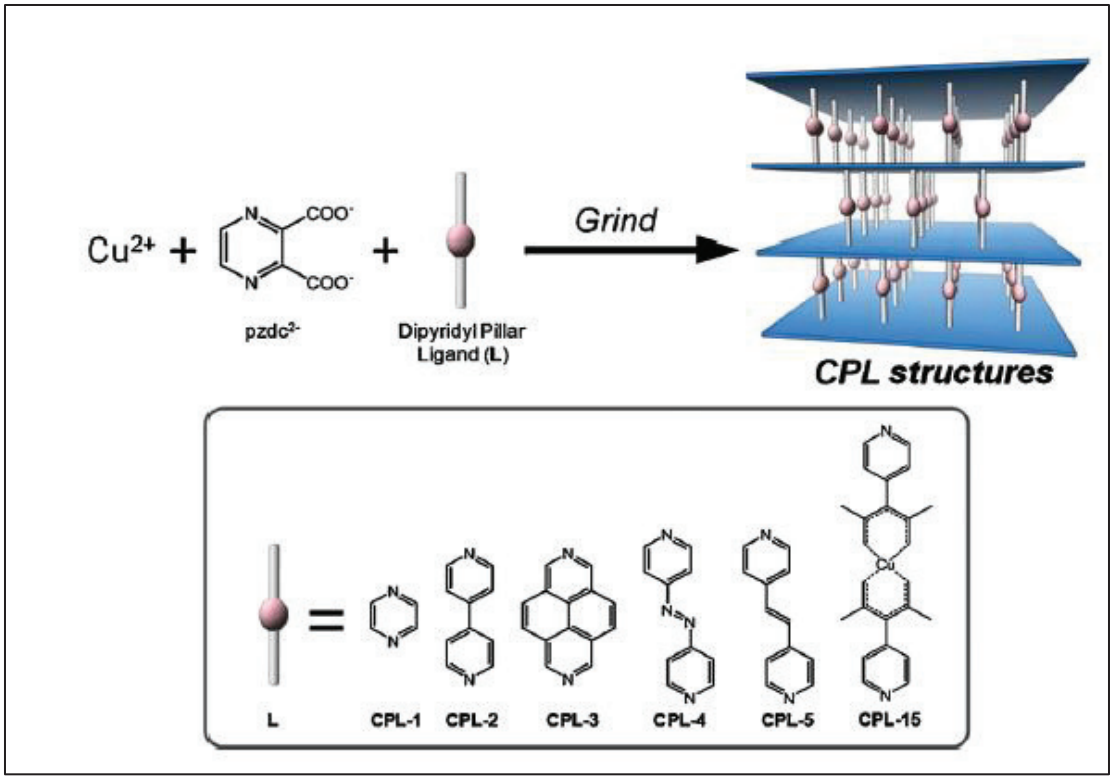

Figure 1-20: Mechanochemical reaction of CPL-1.[27]

Chapter 2: Introduction

2.1 Metal-Organic Frameworks (MOFs)

2.1.1 Concept of a Metal-Organic Framework

A MOF is not a clearly defined material, and could be confused with coordination polymers. There are unresolved discussions about the definition of a MOF. It is known that a MOF should be a porous two- or three-dimensional material, and it is a sub-group under coordination network solids. When working with coordination networks, it is common to refer to them as coordination compounds. The exact definition of a coordination compound is a compound that contains a coordination entity. To be specific, a coordination entity is a material that has an atom, or ion, usually a metal, surrounded by atoms or groups of atoms called ligands.[28] To further understand a coordination entity, the basic structures might include polymers, which are substances consisting of macromolecules.

In the literature, porous coordination polymers (PCPs) can also be known as MOFs. The difference is that PCPs are connected coordination bonds, non-covalent bonds, or other weak interactions, and MOFs are linked together by organic ligands and metal centers. They both have structural flexibility which promotes porosity. Their pores can range from micro- to mesoporous, <2 nm and 2-50 nm, respectively.[24] On page 15 of *Metal Organic Frameworks: Application from Catalysis to Gas Storage* by David Farrusseng et al. it states "Currently, coordination polymers having porous properties are termed PCPs or porous MOFs, and therefore we suggest "coordination framework" as an all-inclusive term because the chemistry of the background is defined as "chemistry of

coordination space."[4] To understand what is being stated these three concepts: (1) framework, (2) molecular metal-organic hybrid, and (3) porosity are discussed.

The first coordination frameworks discovered were simple inorganic complexes. A complete three-dimensional complex, called Prussian Blue ($Fe_4[Fe(CN)_6]_3$), was first determined by X-ray crystallography around 1936, which was a coordination framework connected by bridging cyanide ions. Between 1944 and 1949 the Hofmann Complex was discovered by Hofmann and Küspert.[4,24] The family of Hofmann compounds is a two-dimensional set of frameworks that contain nickel and benzene, with variation in their overall structures. The structures contain bridging cyanide groups which form a square network. Each nickel links to a side of a benzene ring, encapsulating the ring in a channel, Figure 2-1. The variations of the Hofmann complex include deviations of the original complex with different aromatic guests such as aniline, thiophene, and pyrrole.

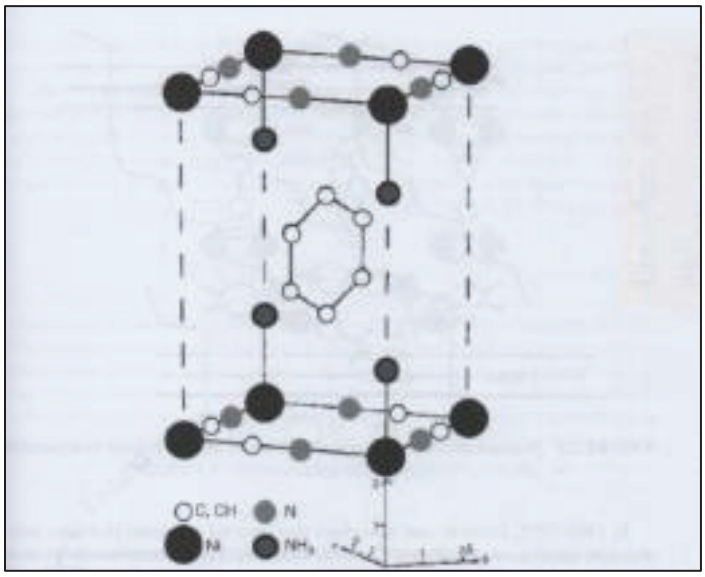

Figure 2-1: Hofmann complex. Partial crystal structure of the Hofmann complex showing benzene within the channel.[24]

2.1.2 Molecular Metal-Organic Hybrid

Frameworks bridged by inorganic ions, i.e. CN^-, are inflexible. Frameworks that have organic ligands to coordinate are stable, flexible, and can be designed for the functionality of the framework. In 1989, Robson reported the first organic coordination network involving copper metal and tetrahedral bridging ligands, Figure 2-2.[24] The framework had a porous volume of 700 $Å^3$, which meant that only one-third of the framework was crystal and the rest was ions and pores. An infinite framework of $\{Cu[C(C_6H_4 \cdot CN_4)]\}^+$ was prepared, with BF_3^-, whose ions were located in the cavities of the compound.

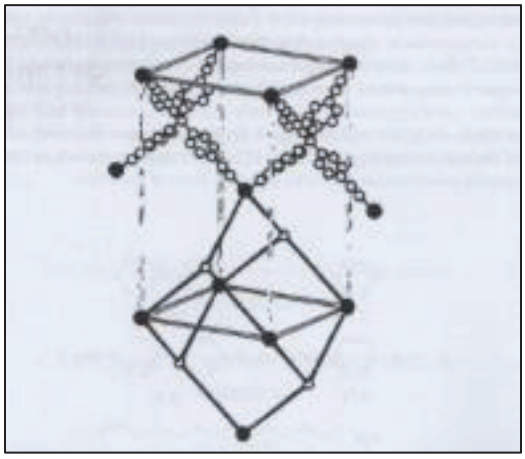

Figure 2-2: Tetrahedral unit cell with black sticks highlighted to form cavity.[24]

With the incorporation of the organic ligand, a macrocyclic polynuclear complex appeared. It started with a cadmium salt and 4,4'-bipyridine (bpy) as a weak base, and resulted in a square network of cadmium metal linked to four bpy molecules, which created large cavities with the possibility of hosting guest molecules, Scheme 1. Yaghi et al. termed compounds with metals, and organic ligands, "metal-organic frameworks (MOFs)."

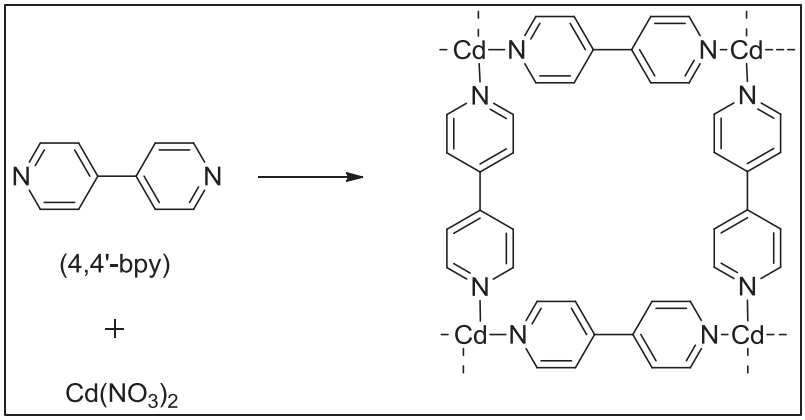

Scheme 2-1: Reaction and formation of cadmium porous organic framework.

2.1.3 Porosity

Metal Organic Frameworks: Application from Catalysis to Gas Storage by David Farrusseng et al. page 16 quotes "Porosity means "the quality or state of being a porous entity, which has many small holes that allow water, air, and so on, to pass through.""[4] In 1995 Yaghi et al. published one of the first MOFs, $[Cu(4\text{-},4'\text{-bpy})_{1.5}](NO_3)\cdot(H_2O)_{1.25}$.[24] The material was synthesized by hydrothermal synthesis. It is visible that each copper center has a trigonal planer orientation with 4,4'-bipyridine ligands extending off of the copper metal, which form six porous and three-dimensional interpenetrating networks.[4] Initially, Yaghi and his team thought that the reaction began with a metal and an organic linker which react to form a metal-organic ligand, Scheme 2-2, which is similar to Scheme 2-1. The organic ligand will react with other metal-ligands in the reaction to form an extended solid, and that is called an extended framework.[29]

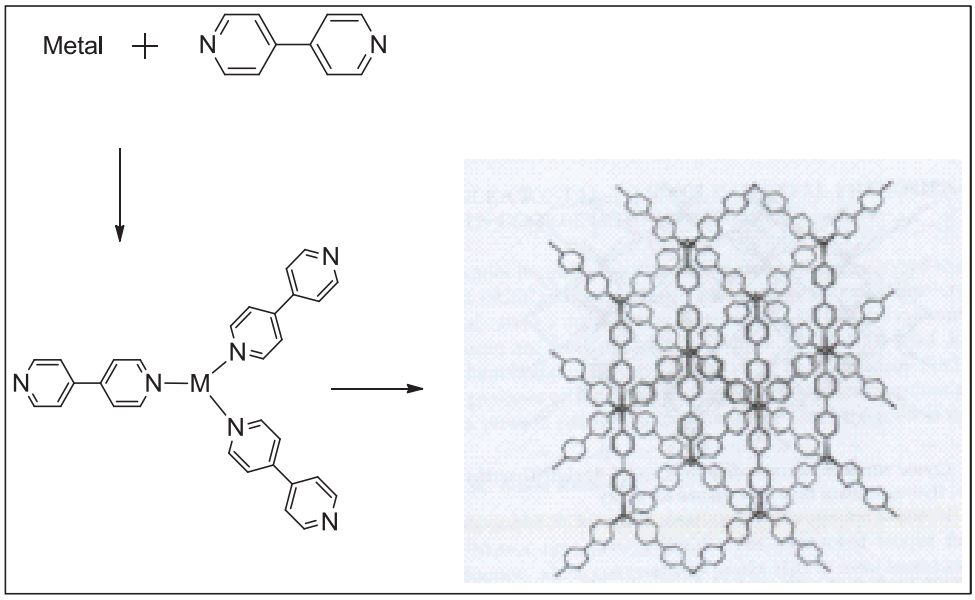

Scheme 2-2: Extended framework formation.[24]

During the hydrothermal synthesis, copper (II) nitrate, 4,4'-bipyridine, and 1,3,5-triazide were put into a programmable autoclave, and the results gave an 87% yield of orange crystals. Analysis of the collected product revealed interpenetration of the structure. The available voids contain nitrate anions, and water molecules, Figure 2-3. The reaction was heated to 140°C and slowly cooled to room temperature over a period of two and a half days. The crystal structure demonstrates gas sorption and the pores are stable up to 180°C.

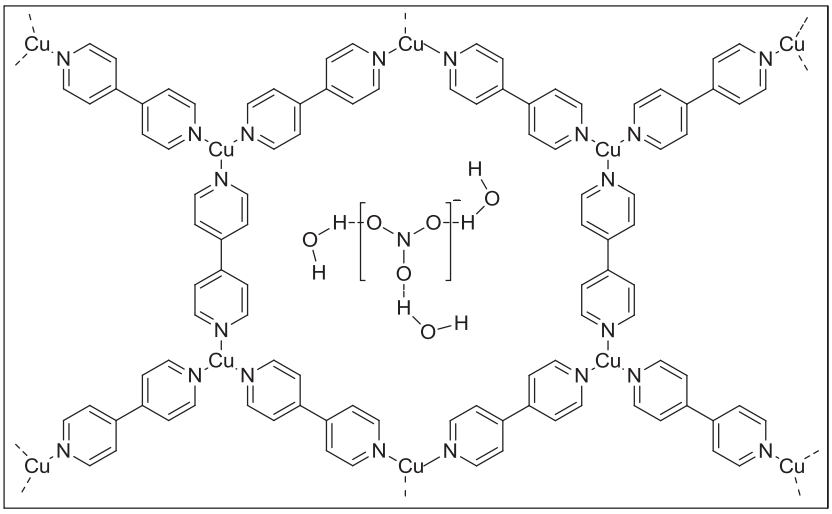

Figure 2-3: Asymmetric unit of $[Cu(4,4'\text{-bpy})_{1.5}](NO_3)\cdot(H_2O)_{1.25}$.

2.1.4 Topology

MOFs and other porous materials have complex crystal structures. The structure explanation can be reduced to a network name depending upon how the connections are within the molecule. A node is a link with two or more connecting substituents, and if there are two or more nodes connected to each other, then that part of a structure can be called a net, Figure 2-4. The number of nets in a structure can be infinite and was first developed by Wells and later perfected by Robson and Hoskins for crystal design. A node can include metal ions, clusters, and ligands; once the node name is determined, the connectivity can be analyzed and the network named.[24]

Hundreds of networks have been named and are used often for structures. The most common type of net is the diamond topology which involves two- and three-dimensional frameworks that can expand from four- to six-dimensional networks, and few have been termed multinodal networks. Once the network is identified then the net has to be classified, involving the exact topology of the framework. To find examples

which help in defining framework topologies, check the Reticular Chemistry Structure Resource (RCSR) database website, http://rcsr.anu.edu.au/.

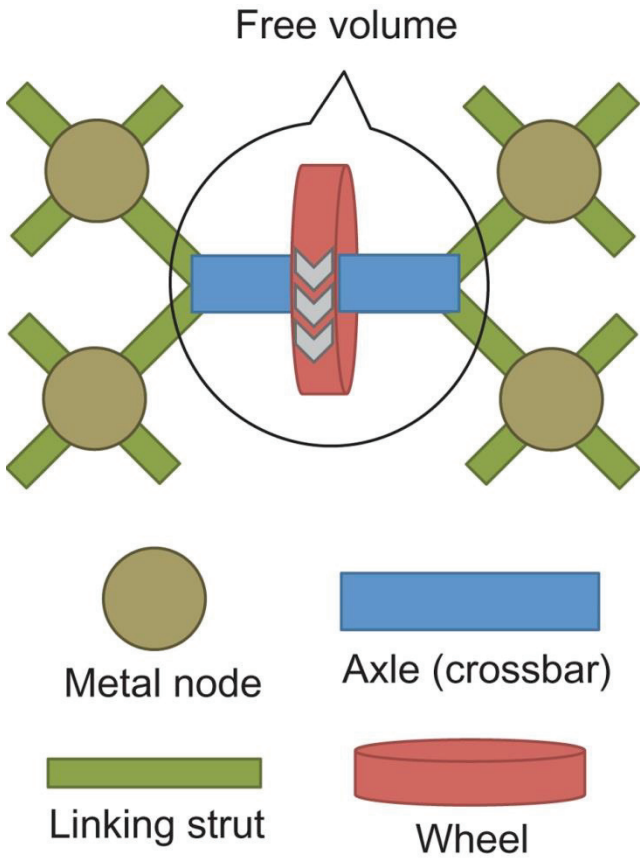

Figure 2-4: Image showing linking strut, node, and net examples.[30]

2.1.5 Interpenetration

A synthesized porous network can contain interpenetration, which is when two or more polymeric networks are weaved within one another and cannot be separated unless chemical bonds are broken, Figure 2-5. During MOF formation, the structure will form so all available spaces are filled, intercalation. The ideal MOF will contain porous networks, which eliminate room for interpenetration; however some interpenetration can be an advantageous for porous networks. It will create the porosity throughout the network while stabilizing the structure. If a structure has interpenetration with a solvent, and the

solvent is removed, the structure could collapse leaving a non-porous and non-crystalline framework.

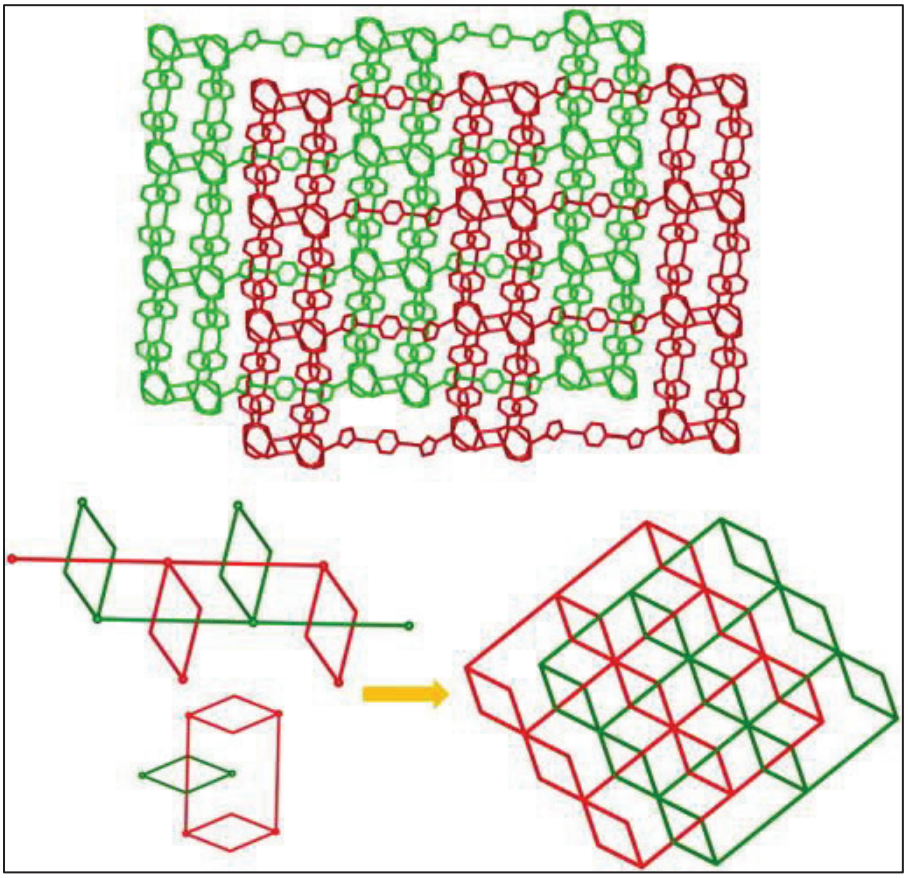

Figure 2-5: Interpenetrating networks. Two-dimensional 2-fold interpenetrating metal-organic framework based on tetranuclear manganese (II) clusters.[31]

2.2 Pore Expansion

2.2.1 Mg-MOF-74

Metal-organic frameworks have shown many advantages as an adsorbent when compared to typical adsorbents currently used in the industry.[32] When gas streams are put into pipelines they initially have CH_4 (50%-65%), CO_2 (35%-50%), and a small amount of N_2. Ideally CO_2 needs to be separated from the other gases down to 2-3% to avoid pipeline corrosion. CO_2 and CH_4 are difficult to separate from each other because of their

gas properties. MOF-74 was a good material for possible CO_2 adsorption because when magnesium was put in place as the metal cation, Mg-MOF-74 was found to have good affinity for CO_2. Mg-MOF-74 was synthesized and characterized by Zongbi Bao *et al.*, and they used a solvothermal synthesis giving dark yellow crystals as the product. A BET surface area of 1174 m^2/g was observed, and CO_2 uptake up to 8.61 mmol/g (37.8 wt.%) was obtained at 298 K and 1 bar.[3]

Figure 2-6, is Mg-MOF-74, dihydroxyterephthalic acid (DHTA), the organic linker, is planar and has two hydroxyl (OH^-) groups extending from the molecule. The two hydroxyl groups are deprotonated by the solvent leaving an oxide (O^-) group. The Mg^{2+} is attracted to the oxide group and forms a ligand. Also, because DHTA is planar, the crystal structure that is formed is symmetrical leaving voids in the molecule, which can be used for gas adsorption.

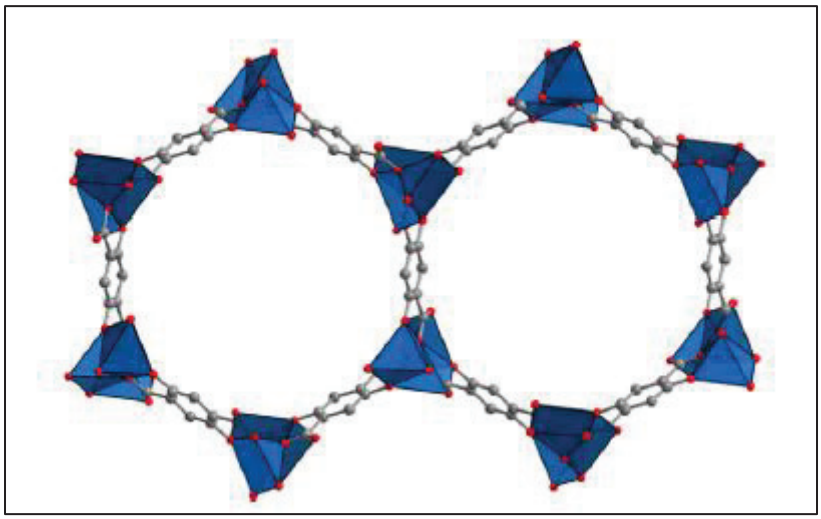

Figure 2-6: Mg-MOF-74.[3]

2.3 Reactant Theory Beginning with Magnesium

It is noted to carefully choose the appropriate reactants to produce a successful MOF. For a MOF to be formed, a hydroxyl group on an organic linker has to be deprotonated by a base, and then the deprotonated oxygen of the hydroxide group has to donate its electrons to a possible metal cation. For a linking bond to occur in a reaction it is suggested that the organic linkers be planer with good symmetry, or contain carboxylate or imidazolate groups for freeing up an oxygen atom, or negative charge. These characteristics help produce successful MOFs. It is observed that most metals in MOFs are originally an ionic salt having an ionic bond between the cation and the anion and they are easily dissociated in the solvent. Once the metal is dissociated it is able to accept electrons from the solvent or deprotonated oxygen.[33]

Magnesium is a fairly reactive metal and connects with many organic ligands to form stable MOFs. Magnesium can be used in reactions because of its reactivity to exchange ligands. Magnesium is able to form a ligand with water molecules, and can be easily removed from the bonded water molecules with a weak base. Another property of magnesium is its ability to form good crystals. The products should be soluble in the solvent that is used during the reaction to result in successful single crystal formation.

Magnesium is versatile and able to form many different products. A magnesium MOF was produced with a (10,3)-a-net topology, or an ability to have chirality.[34,35] In the procedure, a base was used as the solvent, as with Yaghi's procedure described above.[15, 17-19] In Scheme 2-3, the acid gets deprotonated by the base added or formed in situ. The acid has nucleophilic coordinates with a positive charged atom, i.e. a metal cation. There might be product formation at this point resulting in a high quality MOF.

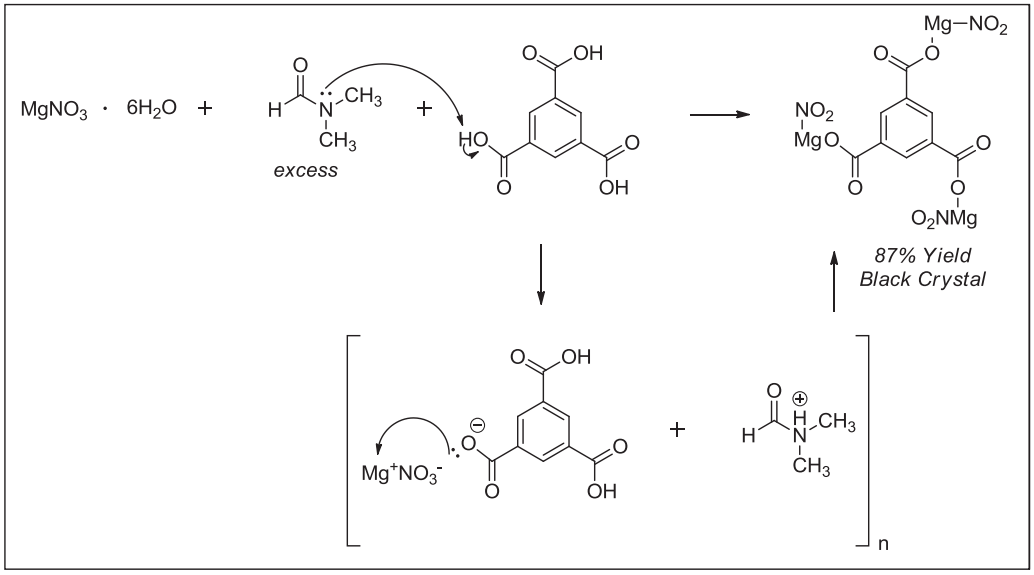

Scheme 2-3: Formation of MOF with solvent.

Because of the versatility of magnesium, most Mg-MOFs form a trimer with three magnesium atoms all linked together, Figure 2-7. This inhibits the symmetry in the structure, and might decrease the void space. Magnesium atoms might form a trimer because of the light atomic weight of the atom. One magnesium atom might not be stable enough to bond to deprotonated oxygen alone. It could be possible that by adding two more magnesium atoms the weight of the first one increases, giving the magnesium trimer more stability. Once the middle magnesium cation is stable, the charge on each outside magnesium cation can accept an electron from an oxygen atom. This might give a penta- or octahedral ligand pattern, depending on type of ligand.[36]

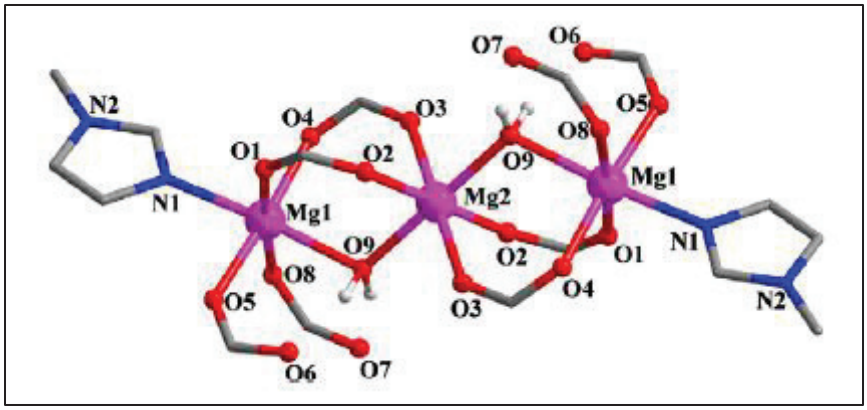

Figure 2-7: Mg trimer linked MOF.[36]

Few Mg-MOFs have been produced to date, but magnesium can act like the divalent transition metal series because it has a 2+ charge. Magnesium can bond with more than one oxygen atom, to itself, or to another lightweight atom. For example, as stated above, a symmetrical Mg-MOF is Mg-MOF-74, Figure 2-6.[3] It has a magnesium atom connected to five oxygen atoms that come from the organic linker, DHTA.

2.3.1 Organic Linker

Mg-MOF-74 has affinity for CO_2 and by increasing the void space in the molecule it might be able to have better adsorption capacity. Di- and polycarboxylate organic linkers are mostly planar. By utilizing a V-shaped ligand, i.e. 4-4'sulfonyl dibenzoic acid (SDBA) it is possible for a more porous product to form from the synthesis, Figure 2-8. These ligands are semi-rigid having rotation around the sulfur bond. SDBA is a versatile ligand having the ability to donate up to six atoms, and can form multiple coordination nodes. By attempting the synthesis with SDBA instead of a planar organic linker, it is possible that the V-shaped ligand will give an expanded void in the product creating better adsorption of gas molecules.[37]

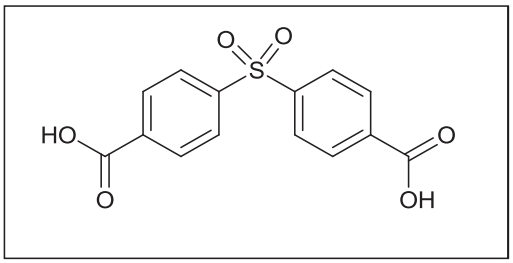

Figure 2-8: 4,4'-Sulfonyl dibenzoic acid.

A disadvantage of using SDBA as the organic linker is its low ability to form single crystal structures. It might be difficult to get the ligand to crystallize when reacted with a metal and a base. To achieve a MOF with high quality data the ideal product is in single crystalline form.

2.3.2 4-4' Bipyridine: A Weak Base

MOF reactions are able to produce *in situ* bases that will deprotonate the hydrogen atoms from the organic linker during the reaction. Some reactions require strong bases, like NaOH, to have a full deprotonation during the reaction. It is dependent on the organic linker if a weak base, strong base, or no base is needed. The materials that have been produced from SDBA have all used a weak base in the reactions, 4,4'- or 2,2'-Bipyridine. In theory the bipyridine should become part of the product, like the one in Figure 2-9 produced by Rishikesh Prajapati *et al.* The π-π stacking interactions between the bipyridine molecules give the structure good symmetry and stability.[38-39]

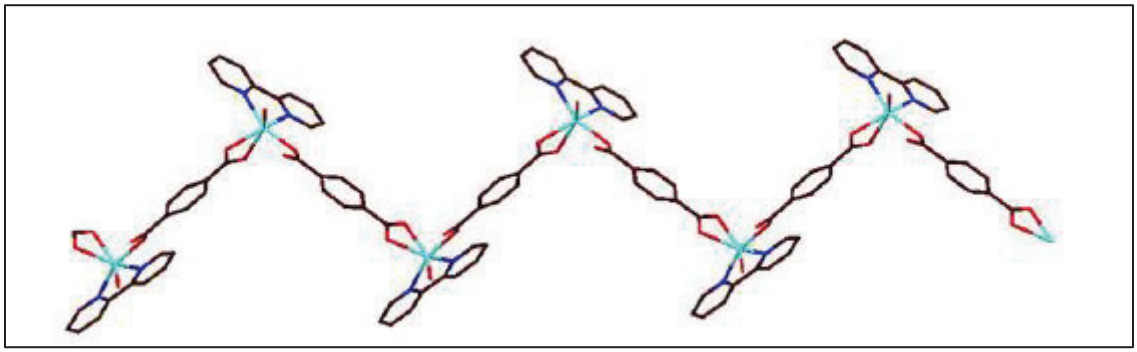

Figure 2-9: π-π stacking interactions between the bipyridine molecules.[38]

2.4 Metal and Organic Linker Synthetic Theory

Magnesium is utilized because of its high reactivity and ability to bond easily to an organic ligand. In theory, the solvent would deprotonate the carboxylate ligand. The negative oxygen atom would then bond with the magnesium cation. The overall product would be a two- or three-dimensional material. The predicted product can be seen in Scheme 2-4.

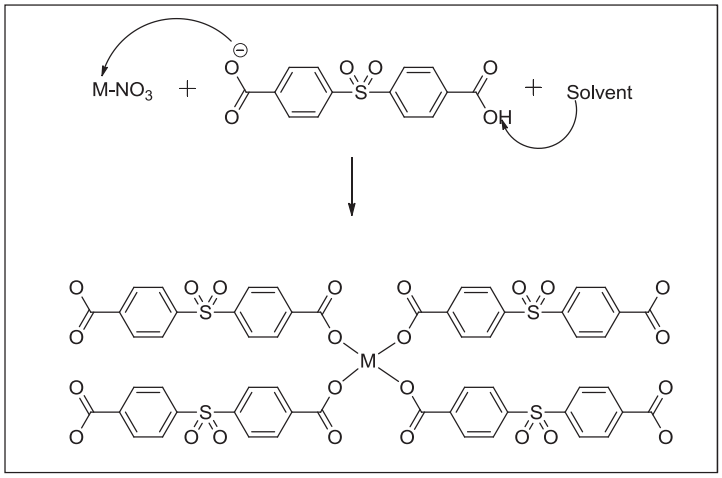

Scheme 2-4: Predicted MOF synthesis.

The goal of the synthesis was to use as little solvent as possible and produce the material within a 72 hour time frame without exceeding 100°C. In a glass vial, 1 mmol equivalent of SDBA and magnesium nitrate, $Mg(NO_3)_2 \cdot 6H_2O$, were added to 6 mL of de-ionized water and stirred for 30 minutes. The vial was then closed and transferred to a 100°C oven for 72 hours. The glass vial was removed and cooled to room temperature. The reaction appeared that it had proceeded however, the characterization of the products resulted in recrystallized starting material and acidic byproducts, as seen in Scheme 2-5.

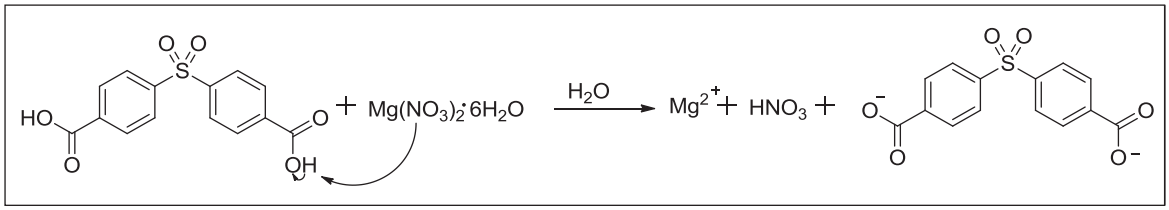

Scheme 2-5: Theoretical reaction with SDBA and metal magnesium salt.

After further research, it was resolved that SDBA must dissolve in solution for the reaction to properly take place.[40-41] It was found that SDBA was only soluble in dimethylformamide (DMF), which is shown in Table 2-1. For more information on carboxylic acids and solubility refer to Appendix A.

Table 2-1: Solubility chart of 4,4'-Sulfonyldibenzoic Acid

Name	Molecular Formula	Molecular Weight (g/mole)
4,4'-Sulfonyl Dibenzoic Acid	$C_{14}H_{10}O_6S$	306.29

1-butanol	1,4-dioxane	1-hexanol	1-pentanol	1-propanol
X	X	X	X	X

2-propanol	DMF	Ethanol	Methanol	THF	Water
X	OK	X	X	X	X

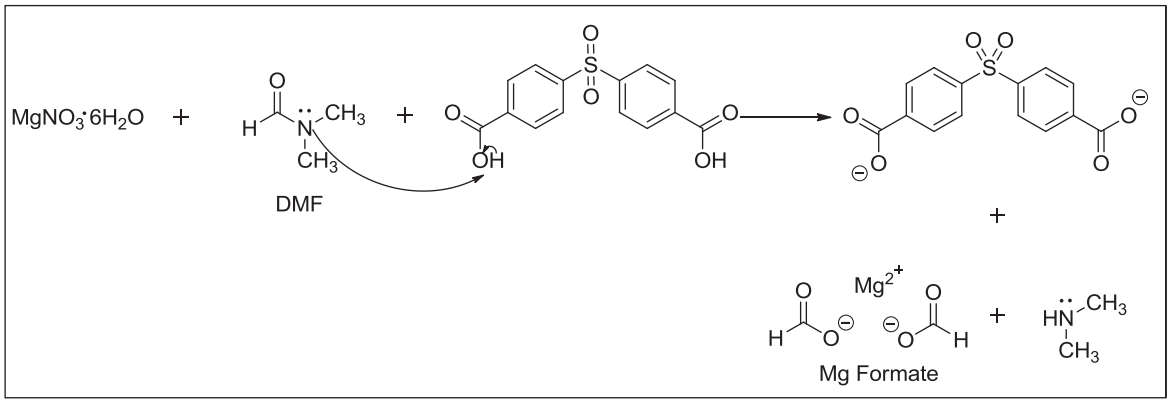

Scheme 2-6: Proposed reaction with DMF as solvent.

The reaction in Scheme 2-6 used DMF as the solvent, but the reaction still did not give the desired product. In the scheme above, DMF deprotonated the organic linker and the DMF carboxylates formed a polar-covalent bond with the magnesium cations. Magnesium formate crystals were produced along with deprotonated SDBA, and left over solvent. It was determined that the pH of the reaction was 4-5.5 which might be too acidic to form a two- or three-dimensional product. A weak base was added to the reaction mixture, which would decrease the acidity, and possibly be a part of the product. It is noted that the instruments for characterization are limited, and the best way to characterize an unknown product from a reaction would be in single crystal form.

To increase the pH to 6-6.5, 4,4'-bipyridine was added to the reaction. The base's linear shape might show promising results. Scheme 2-7 shows the step by step theoretical synthesis. As the solvent deprotonates the SDBA, the magnesium atoms can bond to 4,4'-bipyridine and SDBA to form a two- or three-dimensional framework. The framework might be symmetrical because 4,4'-bipyridine is planar. The product might contain large pores that are able to store gas molecules. The symmetry and large pores can be based off of Mg-MOF-74, which is suggested to resemble the product below.

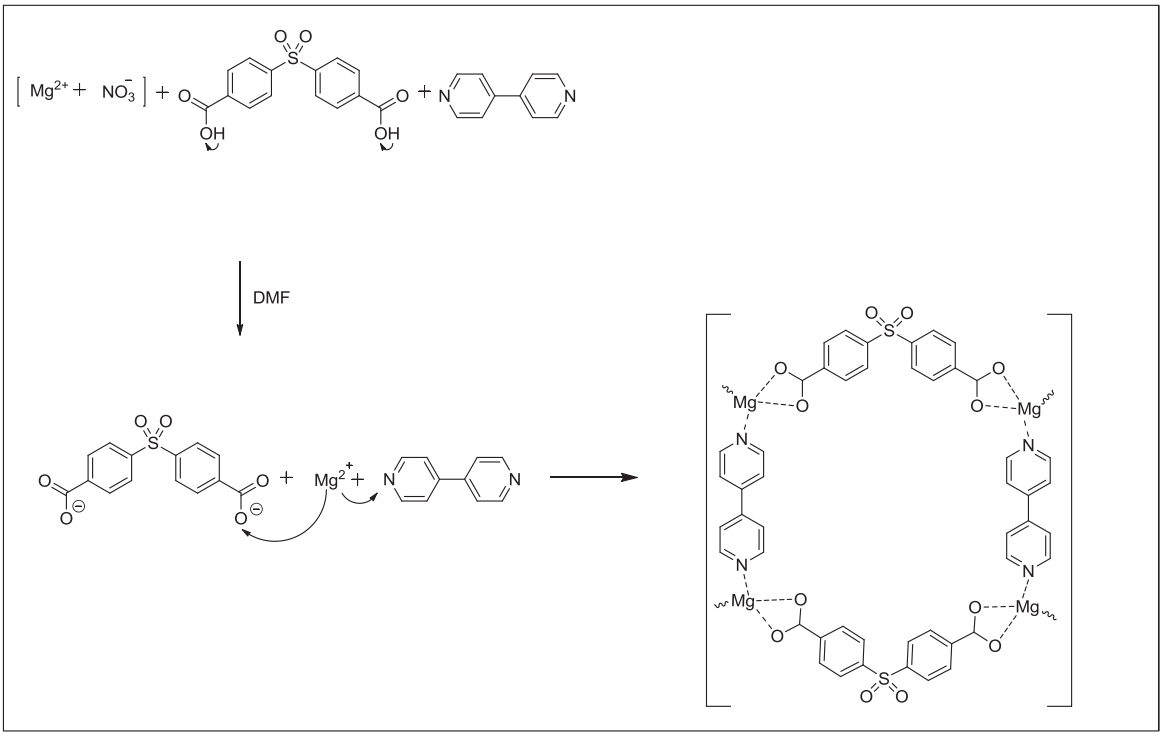

Scheme 2-7: Predicted synthesis with 4,4'-bipyridine as weak base.

For the reactions, a 23 mL Teflon-lined stainless steel autoclave was used with a maximum temperature range to 220°C with water as the solvent. The operating temperature for more volatile solvents is up to 180°C because of pressure build up.

Figure 2-10: Teflon liner (left) and stainless-steel vessel (right)[42].

Chapter 3: Characterization Techniques and Experimental Procedures

3.1 Characterization Techniques

Spectroscopy techniques that are used in this research consist of solid-state techniques that include X-ray diffraction (XRD) and scanning electron microscopy (SEM) coupled with energy dispersive X-ray spectroscopy (EDS). Other characterization techniques used to gain sample data was thermogravametric analysis (TGA), which involves the decomposition of a sample through heat, and differential scanning calorimetry (DSC), which calculate the energy a sample gives off when it is heated to decomposition.

3.1.1 X-Ray Diffraction (XRD)

To determine the placement of the atoms, and what compounds are in a sample, it is necessary to use X-ray diffraction (XRD). Analysis of an unknown powder (or any solid material) can be accomplished by powder x-ray diffraction (PXRD) if the sample is crystalline. Less than 0.5 grams of powder can be spread uniformly on an aluminum disc or salt plate sample holder, flat surfaces bigger than 1/2" X 1" can be analyzed directly and smaller samples can be ground.[43] The output diffraction are a series of peaks observed with the computer program EVA.

Tabulations of d spacings and relative peak intensities for many crystalline compounds have been published by ICDD-International Centre for Diffraction Data and are used as comparison standards for unknown materials. To find a match, it is necessary that an approximate elemental analysis is known at the start, so that the search for a matching pattern can be narrowed.[43]

Figure 3-1 shows a schematic of a Bragg-Brentano geometry diffractometer. In the diffractometer there is a bent monochromator crystal that is hit before the sample and only lets the $K\alpha_1$ radiation to pass through to the sample. The electrons are excited where there is crystalline material of the specimen and the results show peaks with different intensities.[44]

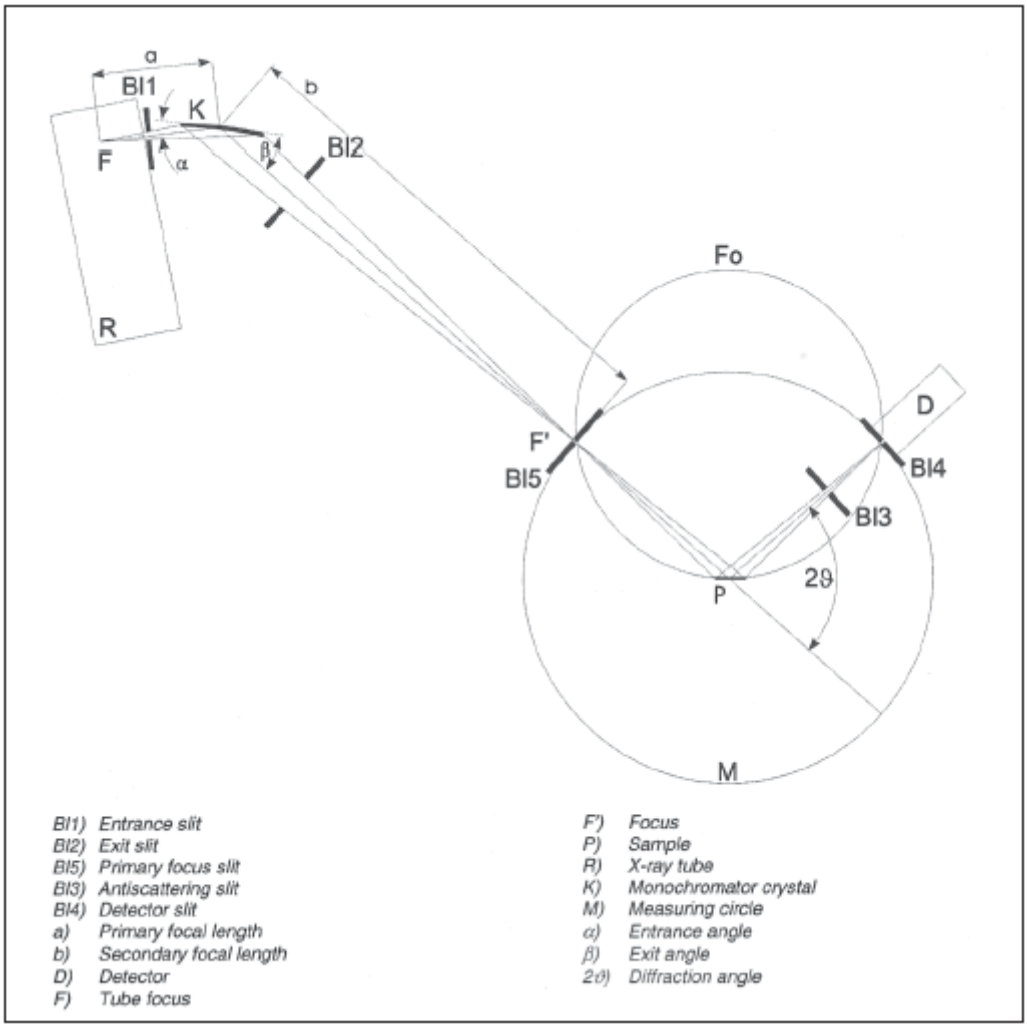

Figure 3-1: Schematic representation of a Bragg-Brentano diffractometer[44].

One of the main equations used in the determination of the diffraction data is called Bragg's Law, Eq. 3-1, which can be used to solve for the d-spacing, the space in between the planes of atoms.[44]

Equation 3-1:

$$n\lambda = 2d \sin \theta$$

λ = wavelength of the x-ray radiation directed onto sample
d = interplanar spacing for each set of crystal planes
2θ = the measured diffraction angle
n = integer (1, 2, 3,....n)

When using a single crystal diffractometer, a mount with the crystal in place is put into the instrument. When an X-ray beam hits the sample the electrons on the crystalline material come to have a higher level of energy. The beam is diffracted by any crystalline material present in the sample. Through a series of refinements the exact places of the specimen atoms can be evolved and the molecular structure of the crystal can be solved. Also, many other details can be determined about the single crystal from the diffraction data including, unit cell data, bond lengths, lattice structure, atomic positions, etc.

To determine the positions of the atoms, and what elements are in a sample, it is necessary to use X-ray diffraction. When using a single crystal diffractometer, a mount with the crystal in place is put into the instrument. When an X-ray beam hits the sample the electrons on the crystalline material become excited. The collected data can be seen in Figure 3-2.[45]

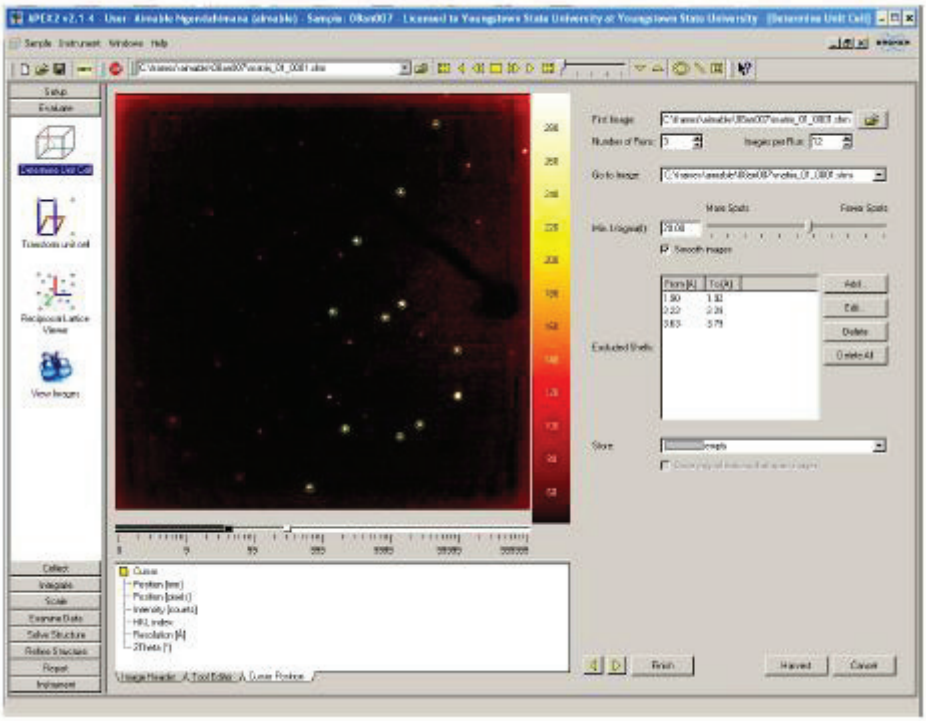

Figure 3-2: Unit cell window with active data collection running[45]

3.1.2 Scanning Electron Microscopy

Scanning electron microscopy (SEM) uses a highly focused electron beam (less than 10nm diameter) which can be scanned in a raster on the sample surface. Interactions between the samples and the incident electrons lead to the ejection of low energy secondary electrons about the location of the incident electron beam. The intensity of secondary electrons produced at each point is used to form a image of the sample.[43] Magnification factors from 10X to 300,000X can be obtained. The depth of field allows the images to be in focus at all points across a rough surface. An electron beam is produced by an electron gun, made from tungsten (W), Lanthanum hexaboride (LaB_6), or a field emission gun (FEG). The beam can be adjusted to a larger probe size or smaller probe size, depending upon the sample and type of instrument being used; the beam is one to ten nanometers in diameter. In addition, the SEM does not suffer from the light

microscope problem of light reflecting off at odd angles and being lost from view. Backscattered electrons can originate from up to about 1µm below the sample surface (depending on the material investigated), are affected by coating with surface layers of dissimilar material, and by the atomic weights of the various components present in the imaged area. This results in grey level variations which can give some indication of the compositions present at various locations on the sample.[43] In Figure 3-3, the depth and relative size of where the beam can penetrate is shown, which is known as interaction volume. Near the top of the tear drop are the secondary and backscattering electrons. Lower in the tear drop characteristic X-rays start to originate allowing energy dispersive X-rays to be determined.

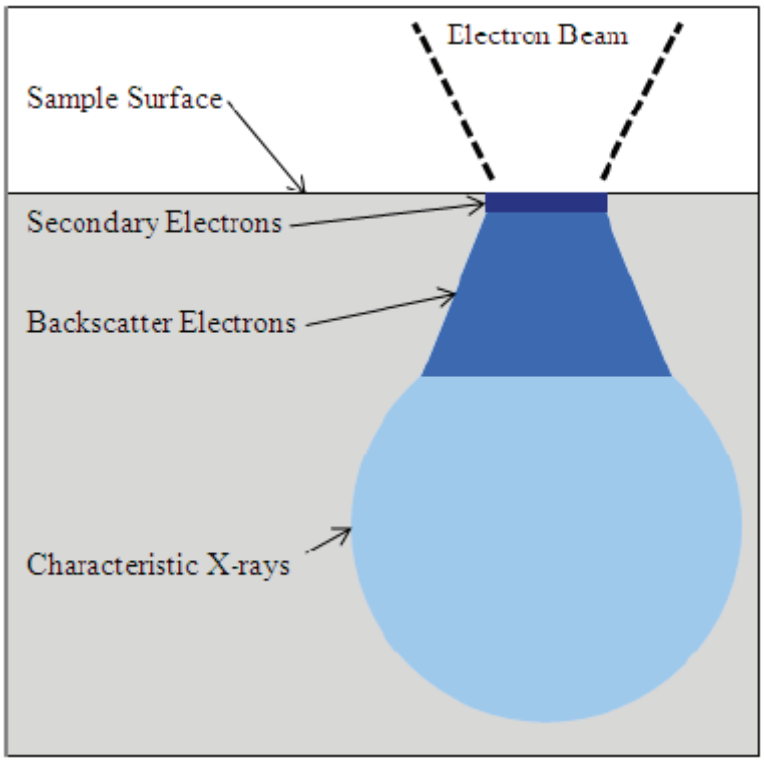

Figure 3-3: Interaction volume tear drop, which is the depth and size of where the electron beam can penetrate into the sample.[44]

3.1.3 Energy Dispersive X-ray Spectroscopy (EDS)

In combination with SEM, Energy dispersive x-ray spectroscopy (EDS) is an effective method for analyzing the main components as well as low-level (nominally 0.1%) contaminants in relatively thick (several micron) layers. A focused beam of electrons is used to bombard a solid in order to knock out electrons from inner electron orbital shells of atoms in the near surface region of the sample.[46] Electrons from outer shells can move into the inner shell vacancies as replacements for the ejected electrons. For each atomic relaxation transition, the energy difference between the outer and inner shell electrons is released by the atom. This energy is emitted either as a characteristic x-ray or as an outer shell electron which has absorbed the energy released by the atomic relaxation process. EDS spectra displays an intensity versus energy plot of x-rays emitted by the sample that are bombarded by the electron beam of a SEM. The vertical scale are the x-ray intensities at each energy position. The horizontal scale runs up to the value of the SEM acceleration voltage which is used and the x-ray peaks which appear on the spectrum have energies in the same range.[46] Since each element emits x-rays of characteristic energies, one can relate an x-ray peak to its corresponding element using a table of major x-ray emission energies. The EDS technique has poor sensitivity for x-rays originating from the light elements. The electron beam may be scanned in a raster on the sample while the spectra are collected.

Another technique that can be used with EDS is elemental distribution mapping. This technique shows where the elements are located throughout the sample. The technique is utilized for mixtures of different alloys and samples that have composite materials. Elemental distribution maps can be obtained to show the distribution on the

sample of an element of interest.[43] The intensity of a digital signal is modulated such that a series of dots appears on the final image with the density or intensity related to the concentration of the element, i.e. more dots or brighter spots indicate more of the element. The elemental distribution shown on the map can be related to the sample topography shown in an SEM secondary electron image taken of the same area.

3.1.4 Thermogravametric Analysis (TGA)/ Differential Scanning Calorimetry (DSC)

Thermal gravimetric analysis (TGA) records the sample weight during heating, thus showing the temperature at which mass is lost The thermal events recorded during the TGA analysis are capable of revealing information about the material composition and its reaction to heating. The sample is placed on a pan that is hooked to a precision balance. The pan with sample is heated or cooled in a furnace during an experiment. A purge gas can flow over the sample throughout the experiment creating a controlled environment. The data are a curve that plots weight (mg) versus temperature (°C) on a graph. With specific materials, a weight percent loss can be determined showing how stable the materials are.[47]

Differential Scanning Calorimetry (DSC) is a sensitive means for measuring the thermodynamic behavior of samples if there are no kinetic hindrances or hysteresis. An experimental sample is heated, at a programmed rate, along with an inert reference material (one that undergoes no abrupt thermal changes over the range of interest). DSC is useful for identifying such properties as melting point, glass transition temperature and endo- or exothermic decompositions. Heat capacity plays a role between the phase transitions in a DSC experiment. DSC is also useful for identifying the heat of transition

of the changes in the materials. The resulting data could be compared to the TGA data to confirm the reactions.[47]

3.2 Statement of Problem

The synthesis of novel porous coordination frameworks will be explored using magnesium nitrate hexahydrate, 4,4'- sulfonyldibenzoic acid, 4,4'-bipyridine, and a series of solvents including, dimethylformamide, methanol, ethanol, and distilled water in theory to form three-dimensional metal organic frameworks. Different instrumentation will be utilized to characterize the products of several reactions to determine their chemical and physical properties.[48]

3.3 Experimental

3.3.1 Materials

Sulfonyldibenzoic acid (SDBA) and 4,4'-bipyridine (bipy) were purchased from Sigma-Aldrich. Magnesium nitrate hexahydrate $[Mg(NO_3)_2]\cdot 6H_2O$ was purchased from Fischer Scientific and dimethylformamide (DMF) was purchased from Sigma-Aldrich. Ethanol and methanol were purchased from Pharmo-AAPER. All materials were used without further purification.

3.3.2 Autoclave Preparation

Autoclave vessels were cleaned with diluted nitric acid (HNO_3) in a 1:1 ration of HNO_3 and distilled water. 2-3 mL of 8M HNO_3 was added into each Teflon-lined stainless steel vessel; the vessels were sealed and put into the oven for 4-6 hours with the oven temperature at 140°C. The vessels were taken out and washed with soap and deionized water.

3.3.3 Reaction Preparation

In each reaction the reactants were added in the following order. DMF was pipetted, to the exact milliliter, into the Teflon liners. SDBA was added and the mixture was stirred until all reagents were fully dissolved. Bipy was added to the solution while being stirred. Other solvents were added followed by $Mg(NO_3)_2 \cdot 6H_2O$ and the mixture was stirred for at least 10 minutes or until the reactants were fully dissolved. The vessels were capped and sealed. The internal temperature of the oven was calibrated to 160°C and the samples were placed in the oven for the time specified for each experiment.

The products obtained were dried by being placed into a Schlenk tube. The valve was connected to a Schlenk line with a high vacuum pump. A dewar filled with liquid nitrogen was placed over the glass tube to keep the products cool under vacuum for 24 hours. The crystals retained their shape through the drying process, and lightened in color going from a darker bluish to a lighter purple.

3.3.4 Powder X-Ray Diffraction

Powder X-ray diffraction patterns were collected at room temperature using a Bruker D8 Advance or a Rigaku Miniflex diffractometer with Cu-Kα radiation in reflective mode, with open sample cups, or open aluminum disc cups, respectively. The data were analyzed using the EVA Application 7.001 software of SOCABIM (1996-2001), distributed by Bruker AXS, Madison, WI. Also, Rietveld refinements were performed using Topas.[46]

3.3.5 Single Crystal X-Ray Diffraction

A single crystal selected by size, and shape, was mounted onto a thin fiber from a pool of Flurolube® oil and immediately placed on a Bruker AXS SMART APEX CCD diffractometer with a fine-focus sealed X-ray tube and a graphite monochromator. The experiments were carried out with Mo Kα radiation at 100K. The lattice parameters were optimized from a least-squares calculation on carefully centered reflections. Apex2 v.2012.4-3 was data collection, SAINT V8.18C was used for integration of data, SHELXS97 and SHELXL2012 were used for solving structures, and SHELXLE Rev576, Shelxle and SHELXTL were used for refinement.[49]

Absorption was corrected for by multi-scan methods. Each structure was solved using direct methods. This procedure yielded the heavy atoms, along with a number of C atoms. Subsequent Fourier synthesis yielded the remaining C atom positions. The reflections were merged according to the crystal class for structure refinement and the calculation of statistics. The final refinement of each compound included refinement of anisotropic thermal parameters on all non-hydrogen atoms.[50]

The valence sum of each metal cation was calculated with the bond valence sum method. The equation, Eq. 3-2, shows that the valence sum of the magnesium cations can be calculated by recorded bond lengths and known constants.

Equation 3-2:

$$\text{Valence Sum} = (1.693 \cdot \text{bond length}) / (0.37 \cdot \text{bond length})$$

3.3.6 SEM/EDS Analysis

For SEM/EDS analysis, no more than 0.20 mg of sample was placed on carbon tape, mounted on a round carbon sample mount, and lightly coated with gold (Au) - for conductivity in the SEM - using an Emscope SC500 sputter coater. The prepared samples were placed onto the goniometer stage of a scanning electron microscope marketed by Topcon (ISI), Inc. of Paramus, NJ. Elemental distribution maps and EDS spectral data were collected from the samples for elemental identification using a Si(Li) crystal detector manufactured by Gresham Scientific Instruments Ltd. of Buckinghamshire, UK, coupled to a multichannel analyzer and imaging interface manufactured by 4pi Analysis, Inc. and resident in an Apple Macintosh® G4 workstation.[43]

3.3.7 TGA/DSC Analysis

Thermal gravimetric analysis (TGA) profiles were recorded on a TA Instruments TGA2050 Thermogravametric Analyzer. Samples were heated at a rate of 10°C min^{-1} from 25 to 500°C under a flow of 60 ml min^{-1} nitrogen. Platinum pans were used and then cleaned in 16M concentrated nitric acid.

Experimental DSC data were collected on DSC2910 Differential Scanning Calorimeter from TA Instruments using an aluminum pan sample holder. Samples were heated at a rate of 10°C min^{-1} from 25 to 500°C under a flow of 60 ml min^{-1} nitrogen. Aluminum pans were discarded after use.

3.3.8 Clausius Clapeyron Equation

The Clausius Clapeyron equation was used to calculate the vapor pressure of the solvent at various temperatures. Eq. 3-3 gives a detailed explanation of how the vapor pressure in the reaction was calculated during the experiment.

Equation 3-3:

$P_1 \cdot V_1 / T_1 = P_2 \cdot V_2 / T_2$

P_1 = Barometric pressure in atm

V_1 = Total volume of solvent in the Teflon-liner

T_1 = 298K (Room Temperature)

P_2 = ?

V_2 = Total volume after reaction (equaled to V_1)

T_2 = Temperature of oven

Chapter 4: Synthesis

4.1 $[Mg]_3[SDBA]_3[DMF]_3[MeOH]$ [1]

During a typical solvothermal synthesis, 9 mL of dimethylformamide was pipetted into a Teflon-lined steel container. 4,4'-sulfonyldibenzoic acid (0.183 g, 0.600 mmol) and 4,4'-bipyridine (0.093 g, 0.600 mmol) were added to the DMF while being stirred. Then, methanol (9.0 mL, pipetted) and $Mg(NO_3)_2 \cdot 6H_2O$ (0.153 g, 0.600 mmol) were added to stirring mixture. The solution was stirred for ten minutes or until reactants were fully dissolved. The Teflon liner was put into the stainless steel container, sealed tightly, and was kept at 160°C for 48 hours. The autogenous pressure produced in the vessel during the reaction was 1.19 atm. The autoclave was taken out of the oven with a non-nitrile glove, set to the side, and cooled to room temperature for 4-6 hours. Reaction yielded small blue/purple fragmented crystals. Powder was light purple in color. The solvent was decanted off, and the crystals were stored in a sealed glass vial. The molecular weight of the structure was determined to be 1237.05 g/mole.

4.2 $[Mg]_3[SDBA]_3[DMF]_3[EtOH]$ [2]

In a 23 mL Teflon-lined steel container, 4,4'-sulfonyldibenzoic acid (0.183 g, 0.600 mmol) and 4,4'-bipyridine (0.093 g, 0.600 mmol) were added to dimethylformamide (9.0 mL) while being stirred. Then, ethanol (9.0 mL) was pipetted into the stirring solution. Next $Mg(NO_3)_2 \cdot 6H_2O$ (0.153 g, 0.600 mmol) was added to the mixture. The Teflon liner was put into the stainless steel vessel and sealed tightly. The vessel was kept at 160°C for 48 hours. The autogenous pressure produced in the vessel during the reaction was 1.19 atm. The reaction was taken out of the oven with a non-nitrile glove, set to the side, and cooled to room temperature for 4-6 hours or cool to the

touch. Reaction yielded lightly tinted, pinkish fragmented crystals, along with a white powder. The solvents were decanted off, and the crystals were stored in a sealed glass vial. The molecular weight of the structure was determined to be 1248.12 g/mole.

4.3 $[Mg]_3[SDBA]_3[DMF]_3[EtOH]\cdot H_2O$ [3]

In a 23 mL Teflon-lined steel container, 4,4'-sulfonyldibenzoic acid (0.183 g, 0.600 mmol) and 4,4'-bipyridine (0.093 g, 0.600 mmol) were added to dimethylformamide (9.0 mL) while being stirred. Then, ethanol (9.0 mL) was pipetted into the stirring solution. Next $Mg(NO_3)_2\cdot 6H_2O$ (0.153 g, 0.600 mmol) and 2.0 mL of distilled H_2O were added to the mixture. The Teflon liner was put into the stainless steel vessel and sealed tightly. The vessel was kept at 160°C for 48 hours. The autogenous pressure produced in the vessel during the reaction was 1.07 atm. The reaction was taken out of the oven with a non-nitrile glove, set to the side, and cooled to room temperature for 4-6 hours or cool to the touch. Reaction yielded lightly tinted, pinkish fragmented crystals, along with a white powder. The solvents were decanted off, and the crystals were stored in a sealed glass vial. The molecular weight of the structure was determined to be 1233.31 g/mole.

4.4 $[Mg]_3[SDBA]_3[DMF]_4$ [4]

To complete a solvothermal synthesis, 18.0 mL of dimethylformamide was pipetted into a Teflon-lined steel container. Then, 4,4'-sulfonyldibenzoic acid (0.183 g, 0.600 mmol), 4,4'-bipyridine (0.093 g, 0.600 mmol), and magnesium nitrate hexahydrate (0.153 g, 0.600 mmol) were added to the DMF while being stirred. The solution stirred for at least ten minutes, or until the reactants were fully dissolved. The Teflon liner was set in the stainless steel vessel, and then the autoclave was closed tightly and kept at

160°C for 48 hours. The autogenous pressure produced in the vessel during the reaction was 1.19 atm. The autoclave was taken out with a non-nitrile glove, set aside, and cooled to room temperature for 4-6 hours. The reaction yielded blue/pinkish fragmented crystals, and light blue powder. The DMF was decanted off the crystals and they were stored in a sealed glass vial until further use. The molecular weight of the structure was determined to be 1271.84 g/mole.

4.5 [SDBA][Bipy] [5]

This solvothermal synthesis was a scaled up version of **[4]** however the byproduct was what was of interest. Initially 156.0 mL of DMF is added to a Teflon-lined stainless steel autoclave. 4,4'-sulfonyldibenzoic acid (0.842 g, 2.75 mmol), 4,4'-bipyridine (0.428 g, 2.74 mmol), and $Mg(NO_3)_2 \cdot 6H_2O$ (0.704 g, 2.77 mmol were added to dimethylformamide (156 mL) while being stirred. The solution was stirred for at least 10 minutes, or until the reactants were fully dissolved. The Teflon container was put into the stainless steel vessel, sealed tightly, and then put in oven at 160°C for 48 hours. The autogenous pressure produced in the vessel during the reaction was 0.624 atm. The vessel was taken out and cooled to room temperature for 8-12 hours. Reaction yielded lightly tinted, bluish fragmented crystals with white precipitate. There was approximately 50.0 mL of brown solvent left over from the reaction. The solvent sat out in a beaker for 1-2 weeks in a fume hood with substantial air flow. Light brown needle-like crystals formed and dried in room temperature air. Powder had a light brown color.

4.6 Ball Milled Product [6]

The product was from a mechanochemical synthesis reaction. 4,4'-sulfonyldibenzoic acid (0.183 g, 0.600 mmol), 4,4'-bipyridine (0.093 g, 0.600 mmol), and magnesium nitrate hexahydrate (0.153 g, 0.600 mmol) were added to a stainless steel ball mill vessel with two 7 mm stainless steel balls. The vessel was sealed tightly and the mixture was milled for 30 minutes. Once the vessel cooled to room temperature, the product was taken out of the vessel and grounded with mortar and pestle for approximately two minutes. The product was stored in a glass vial.

4.7 Al_2O_3 Pellet

A pellet press was used to produce an alumina disc. A metal pellet holder was filled 1/3-1/2 of the way up with alumina (50-200 μm). The holder was assembled and put into the press. The lever was attached and pumped down until the pressure gauge read 2000 psi. Next, the pellet was released by turning the assembly over and putting it back into the press and a plastic cylinder was placed on top of the assembly. A vacuum was created in the press by using the pump once again. The vacuum pulled the pellet up and out of the holder, pellet was taken out, and vacuum and holder were released. The pellet was then sintered in a programmable oven for two hours at 1200°C. The oven was programmed to step up from room temperature to 1200°C and then back down to 70°C in two hours. Once taken out of the oven, the pellet was cooled to room temperature. If needed, to make the pellet even and open pores, the one side of the pellet was sanded several times evenly across the surface with 2400 grit sand paper.

4.8 $[Mg]_3[SDBA]_3[DMF]_3MeOH$ [1] on Al_2O_3 Pellet

6.0 mL of DMF was pipetted into a Teflon-lined stainless steel autoclave. An alumina pellet was put into a Teflon vessel containing 6.0 mL of dimethylformamide (DMF) and soaked for five minutes. The pellet was then taken out of the DMF, 4,4'-sulfonyldibenzoic acid, SDBA, (0.061 g, 0.200 mmol) and 4,4'-bipyridine (0.031 g, 0.200 mmol) were added to the DMF and stirred until dissolved. The alumina pellet was then put into the stirred solution and soaked for 20 minutes. Again the pellet was taken out of solution and transferred to a beaker that contained 6.0 mL of methanol, and soaked for five minutes. The pellet was taken out of the methanol, magnesium nitrate, $Mg(NO_3)_2$, (0.051 g, 0.200 mmol) was added to the methanol and stirred until dissolved. The pellet was put into the methanol solution and soaked for 20 minutes, and then taken out once again. The methanol solution was transferred into the Teflon vessel which contained the DMF solution and they were stirred together for 10 minutes. The alumina pellet was added back into the Teflon vessel with the mixed solutions and soaked for 5 minutes. The vessel was sealed in the stainless steel autoclave and put into the oven for 48 hours at 160°C. The autogenous pressure produced in the vessel during the reaction was 0.594 atm. The vessel was taken out of the oven with a non-nitrile glove, set aside, and cooled to room temperature for 8-12 hours. The alumina pellet was taken out of the vessel and dried in a 60°C oven over night. Once taken out of the drying oven, the alumina pellet had noticeable bluish crystals and was stored in a glass vial.

Chapter 5: Results

5.1 Macroscopic Observations

The crystals that were produced from the solvothermal synthesis reactions were various colors. The pure organic structures were brown and clear colored crystals. The crystals shapes were different from one another, with reactions producing blocked-shaped, rod-shaped, and fragment-like crystals. The Mg-MOF products demonstrated a distinct color change in the visible spectra. The materials would consistently change color from pink, to light purple, to a light blue. When dried, the crystals appeared light blue in color. A white precipitate was intermixed, which might suggest a phase change in the structure. It was known that the crystals were not starting materials because magnesium nitrate and 4,4'-sulfonyl dibenzoic acid have clear crystal color when recrystallized. When the crystals were dried in air, white precipitate formed on the crystals' surface, as a result of de-solvation. Once an outer layer of precipitate formed, the wet product underneath received insufficient air to dry completely, even when put into a 60-100°C oven for more than 24 hours. To achieve dry crystals with little precipitate, they were dried under vacuum, in a dewar, for 24 hours. Even this type of drying caused the crystals to de-solvate, but they did retain their light blue color, giving validation to move forward with the study. To further explore the material, additional characterization techniques were utilized.

5.2 Results

Although the area of MOFs is widely researched, there is still much opportunity for "trial and error" synthesis. Not every reaction produces a successful MOF and more commonly produced are one- and two- dimensional coordination polymers with no

framework structure. Coordination complexes are also produced, with individual metal complexes not covalently interconnected with each other. Sometimes the reaction fails to incorporate any metal into the structure formed, i.e., formation of structures consisting of only ligand and solvate molecules. Although these are not the intended product they still contain interesting properties.

Some MOFs produced with magnesium as the metal form trinuclear metal clusters as their centers.[36] The examples found with magnesium metals forming trinuclear clusters contain only linear linkers.[50-55] A trinuclear magnesium clustered MOF has not been produced which contains a bent ligand shape. The advantages of the bent shaped ligand is to provide more space between the metal centers and give the structure a three dimensional shape.[37]

To confirm that three-dimensional magnesium clustered MOFs were successfully produced collaborative studies of the structures in the MOF complexes have been undertaken. In joint work with Dr. Matthias Zeller, Research Staff Scientist of Youngstown State University and Dr. Koteswara Rao Vandavasi, Post-Doctoral Researcher at Youngstown State University, single-crystal X-ray crystallographic analyses were taken. The extended structures and further characterization methods are discussed in this section.

When working with carboxylates of MOFs, there are specific binding modes in which the carboxylates bind to the metal centers. The different sizes and shapes of the linkers and coordination of the metal, help form the specific coordination mode.[51] A scheme of the coordination modes is below, Scheme 5-1.

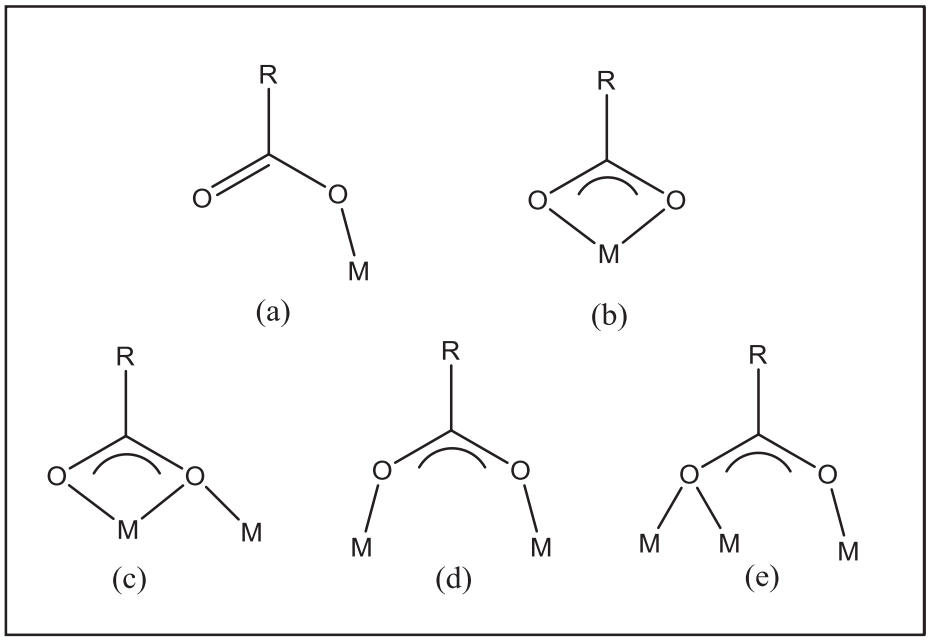

Scheme 5-1: Schematic representation of selected binding modes of carboxylate ligands: (a) terminal, (b) unidentate, (c) unidentate bridging, (d) bidentate, and (e) bidentate bridging.

Table 5-1: Summary of products

Formula	Sample Contents	Notes
[1] $[Mg]_3[SDBA]_3[DMF]_3MeOH$	Magnesium nitrate hexahydrate, 4,4'-sulfonyldibenzoic acid, and 4,4'-bipyridine with dimethylformamide and methanol as solvents.	Purple/Bluish Least disorder
[2] $[Mg]_3[SDBA]_3[DMF]_3EtOH$	Magnesium nitrate hexahydrate, 4,4'-sulfonyldibenzoic acid, and 4,4'-bipyridine with dimethylformamide and ethanol as solvents.	Transparent Pinkish
[3]$[Mg]_3[SDBA]_3[DMF]_3EtOH{\cdot}H_2O$	Magnesium nitrate hexahydrate, 4,4'-sulfonyldibenzoic acid, and 4,4'-bipyridine with ethanol, distilled water, and dimethylformamide as solvents.	Pinkish/White Uncoordinated water molecule
[4] $[Mg]_3[SDBA]_3[DMF]_4$	Magnesium nitrate hexahydrate, 4,4'-sulfonyldibenzoic acid, and 4,4'-bipyridine with dimethylformamide as solvent.	Purple/Blue/ Pinkish Most Stable
[5][SDBA][Bipy]byproduct from [1]	Magnesium nitrate hexahydrate $[Mg(NO_3)_2{\cdot}6H_2O]$, 4,4'-sulfonyldibenzoic acid (SDBA), and 4,4'-bipyridine (bipy) with methanol and dimethylformamide as solvents.	Brown
[6] Ball Milled sample	Magnesium nitrate hexahydrate $[Mg(NO_3)_2{\cdot}6H_2O]$, 4,4'-sulfonyldibenzoic acid (SDBA), and 4,4'-bipyridine (bipy)	Light Grey, no solvent

5.2.1 $[Mg]_3[SDBA]_3[DMF]_3MeOH$

Synthesis of a magnesium based MOF, $[Mg]_3[SDBA]_3[DMF]_3MeOH$ [1], from magnesium nitrate hexahydrate, 4,4'-sulfonyldibenzoic acid, and 4,4'-bipyridine

[1] was synthesized from magnesium nitrate hexahydrate [$Mg(NO_3)_2 \cdot 6H_2O$], 4,4'-sulfonyldibenzoic acid (SDBA), and 4,4'-bipyridine (Bipy) in DMF and methanol as seen in Scheme 5-2:

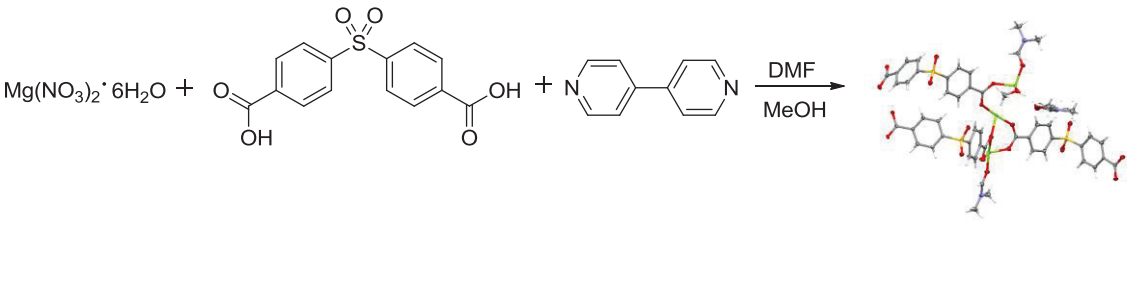

Scheme 5-2 [1]

The carboxylate groups on SBDA are deprotonated under solvothermal conditions as magnesium metal cation binds with the oxides (O^{2-}). The mixture was stirred in a 23 mL Teflon-lined stainless steel autoclave until reactants were dissolved and the vessel was sealed and put into an oven at 160°C for 48 hours. Upon completion of the reaction, the solvent was decanted off and crystals were dried in air, resulting in purple crystals along with some unidentified white precipitate. The molecular structure of [1] determined by single crystal X-ray analysis is shown in Figure 5-1 and the selected bond lengths and angles are shown in Table 5-2.

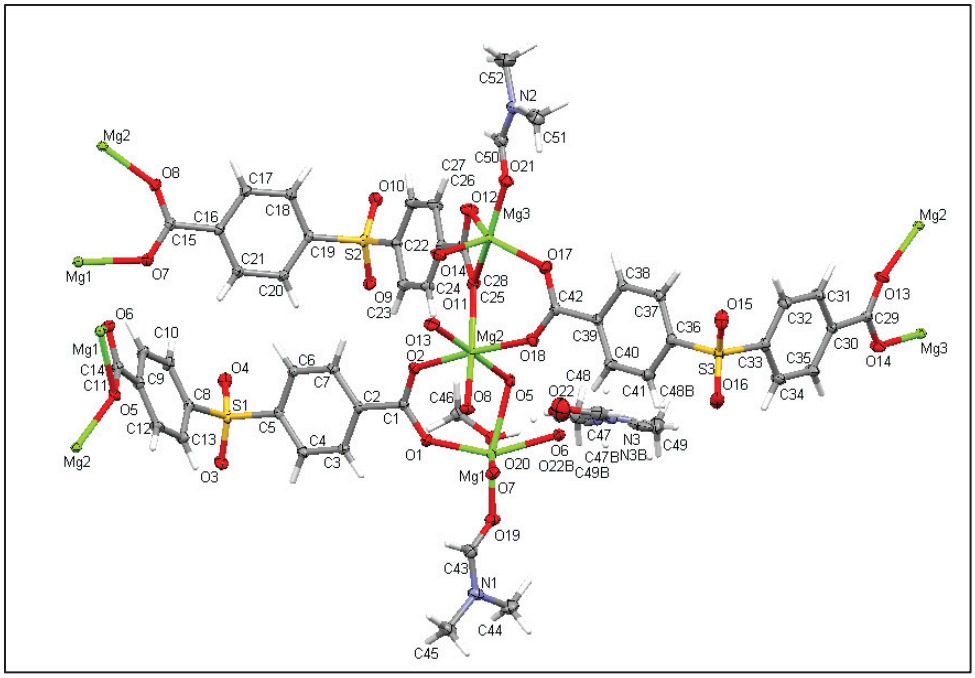

Figure 5-1: Molecular structure of [1] with 50% thermal ellipsoids.

The molecular structure consists of three independent magnesium atoms that are arranged in a co-planer trinuclear cluster (Mg trimer), three coordinated SDBA molecules, three DMF molecules, and a coordinated methanol molecule. For this structure and the following three structures the metals bond to the organic ligands in a repeating pattern. Recent papers have shown that linear organic carboxylate linkers can bond to trinuclear metal clusters and create high symmetry within the structures.[50-54] Unlike successful linear trinuclear metal clustered MOFs, the organic linkers in [1] are non-linear, or bent shaped, making the structure more complex. Each magnesium cluster contains three organic linkers which are bonded in a bidentate or unidentate bridging coordination environment (refer to Scheme 5-2). Three other organic linkers, each from a neighboring unit cell, bridge to the trinuclear magnesium cluster. Overall each magnesium cluster has six coordinated organic linkers.

The Mg-O distances for the Mg1 and Mg2 atom range from 1.979(11)-2.164(11) Å whereas the Mg-O distances for the Mg3 atom range from 1.932(12) -2.298(11) Å. The bond valence sum of the Mg-O bonds showed that Mg1, Mg2, and Mg3 have a valence of + 2.12, +2.14, and +2.068, respectively, which indicates Mg atoms are in +2 oxidation state.

Table 5-2: Selected Bond Lengths (Å) and Angles (°) for [1].

Bond	Bond Length	Valence
Mg1-O19	2.0173(11)	0.416579
Mg1-O20	2.1551(12)	0.286892227
Mg1-O1	1.9792(11)	0.461638587
Mg1-O7	2.0485(11)	0.383099911
Mg1-O6	2.0686(11)	0.361961938
Mg1-O5	2.2635(11)	0.213686938
Valence Sum	**Mg1**	**2.123859**
Bond	**Bond Length**	**Valence**
Mg2-O11	2.1636(11)	0.279998
Mg2-O18	2.0910(11)	0.341067
Mg2-O8	2.0270(11)	0.405472
Mg2-O2	2.0977(11)	0.334675
Mg2-O5	2.0519(11)	0.378981
Mg2-O13	2.0245(11)	0.40767
Valence Sum	**Mg2**	**2.147863**
Bond	**Bond Length**	**Valence**
Mg3-O11	2.2981(11)	0.194926
Mg3-O12	2.0292(12)	0.403286
Mg3-O21	1.9678(11)	0.475569
Mg3-O14	1.9725(12)	0.470455
Mg3-O17	1.9319(12)	0.524166
Valence Sum	**Mg3**	**2.068403**

Bond Angles	Amplitude	Bond Angle	Amplitude	Bond Angle	Amplitude
O1 Mg1 O19	102.48(5)	O13 Mg2 O8	85.32(5)	O17 Mg3 O21	94.90(5)
O1 Mg1 O7	93.02(5)	O13 Mg2 O5	177.85(5)	O17 Mg3 O14	116.29(6)
O19 Mg1 O7	88.65(5)	O8 Mg2 O5	94.97(5)	O21 Mg3 O14	98.83(5)
O1 Mg1 O6	152.09(5)	O13 Mg2 O18	95.72(5)	O17 Mg3 O12	126.54(6)
O19 Mg1 O6	104.29(5)	O8 Mg2 O18	86.78(4)	O21 Mg3 O12	95.51(5)
O7 Mg1 O6	95.35(5)	O5 Mg2 O18	86.43(4)	O14 Mg3 O12	113.56(5)
O1 Mg1 O20	88.84(5)	O13 Mg2 O2	89.98(5)	O17 Mg3 O11	92.81(5)
O19 Mg1 O20	87.75(5)	O8 Mg2 O2	92.67(4)	O21 Mg3 O11	154.25(5)
O7 Mg1 O20	176.23(5)	O5 Mg2 O2	87.88(4)	O14 Mg3 O11	99.67(5)
O6 Mg1 O20	84.47(5)	O18 Mg2 O2	174.21(5)	O12 Mg3 O11	60.58(4)
O1 Mg1 O5	91.59(4)	O13 Mg2 O11	82.98(5)		
O19 Mg1 O5	163.74(5)	O8 Mg2 O11	166.94(5)		
O7 Mg1 O5	98.84(4)	O5 Mg2 O11	96.94(4)		
O6 Mg1 O5	60.84(4)	O18 Mg2 O11	88.63(4)		
O20 Mg1 O5	84.37(4)	O2 Mg2 O11	93.10(4)		

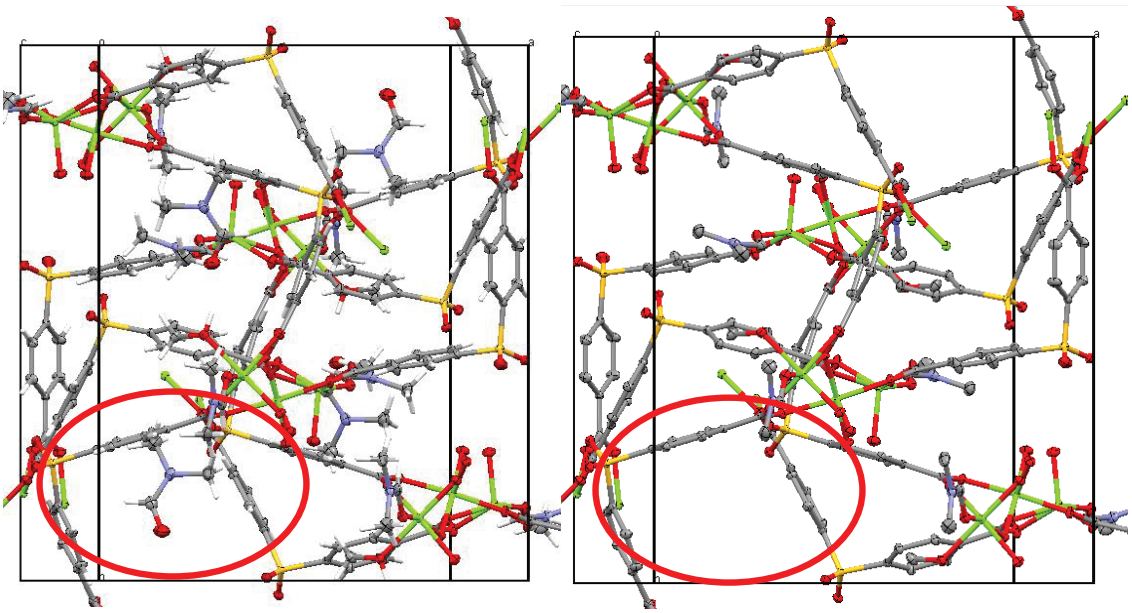

Figure 5-2: Packed cell of [1] along the *c**-axis (50% thermal ellipsoids).

In Figure 5-2, the left image shows the uncoordinated DMF molecules along with the hydrogen bonds, which were eliminated in bottom image for clarity. For elements: nitrogen (blue), carbon (gray), oxygen (red), sulfur (yellow), and magnesium (green). It is suggested that by removing the uncoordinated DMF molecules from the structure possible pore space can be created. There is no known way as of yet to remove the uncoordinated DMF molecules effectively and further research is suggested. Solvent exchange was attempted unsuccessfully by trying to exchange the DMF molecules with dichloromethane.

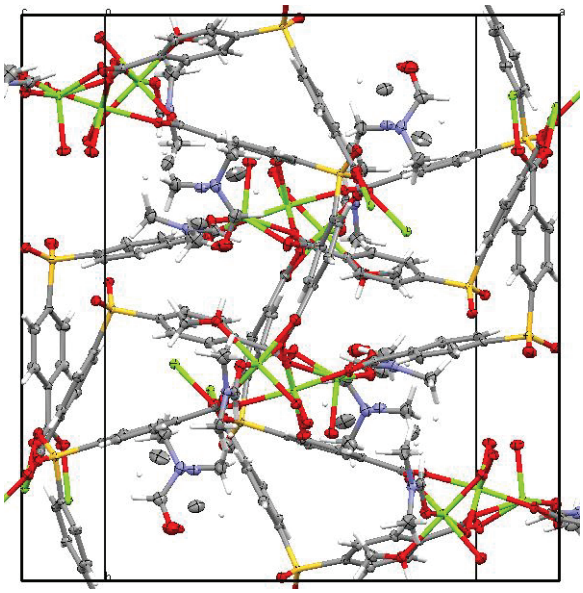

Figure 5-3: Packed cell of [1] with view along *c**-axis. The disorder that is noticed within the packed cell of [1] is the least disorder of the four MOFs produced.

Variation of the solvents causes change in flexibility, stability, and dihedral angles within the MOFs. The amount of disorder in the crystal structure depends upon the solvent utilized. As the solvents become more non-polar the disorder will increase, the flexibility of the structure increases, and the stability of the structure increases. MOF [1] uses solvents of methanol and DMF and contains one DMF with disorder. Although from a molecular standpoint this seems to be the best-behaved crystal out of the four MOFs.

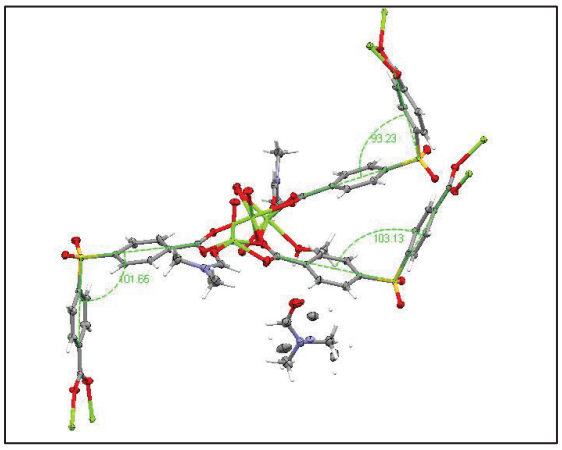

Figure 5-4: Molecular structure with organic linker angle measurements, thermal ellipsoids at 50%.

The dihedral angles present in the SDBA linkers from Mg1-Mg3, are shown in Table 5-3. The angles were calculated by specifically choosing atoms in Mercury® software. The linkers have torsion angles, rotating at the sulfur-carbon bonds. The formation of the crystal is one possibility of a three-dimensional structure. The flexibility and orientation of the phenylene rings and carboxyl groups with arrangement of the solvent molecules leads to a variety of possible structures.

Table 5-3: Dihedral Angles of [1].

Linker	Atoms	Angle
SDBA(1) of Mg1	C1 S1 C14	93.23
SDBA(2) of Mg2	C15 S2 C28	103.13
SDBA(3) of Mg3	C29 S3 C42	100.56

SDBA was dissolved into a 1:1 ratio of DMF to methanol. The crystals from that reaction were a light blue color, and the single crystal diffraction results collected were good data with a high collection rate. To reveal the presence of possible macro-voids in the materials, SEM images at different magnifications were taken of the new material. At different locations of the material, it is shown that some of the crystal kept its shape and some of the DMF precipitated out of the crystal, causing de-solvation. Figure 5-5 (a) and (b) demonstrate the morphology of the bulk material. Note that there appears to be a smooth surface on the outside of the product. Figure 5-6 confirms that there are areas where the material is suggested to have de-solvated because of the DMF precipitate. To determine if the structure has pores or channels in the crystalline lattice further characterization is required, e.g., transmission electron microscopy.

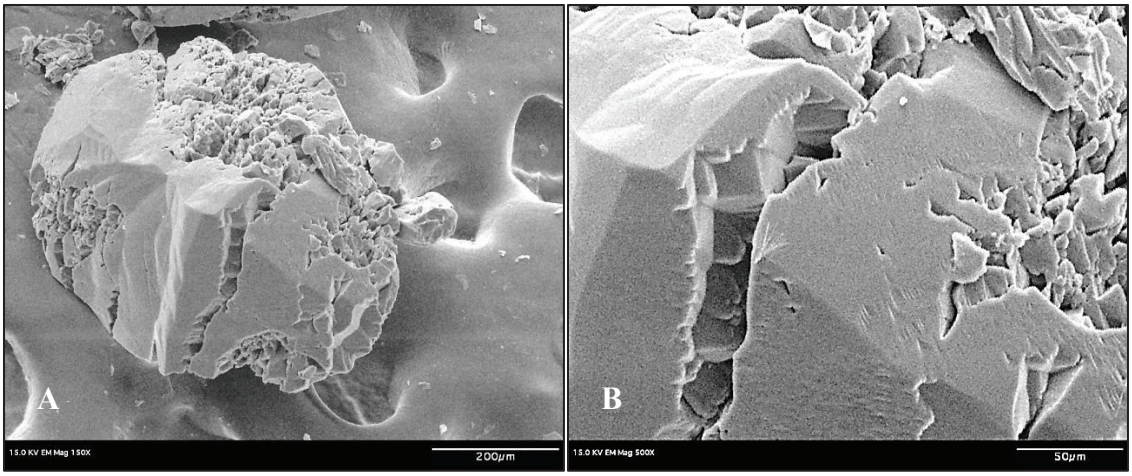

Figure 5-5: SEM images of material [1] with visible channels, magnification of 150X and 500X, respectively.

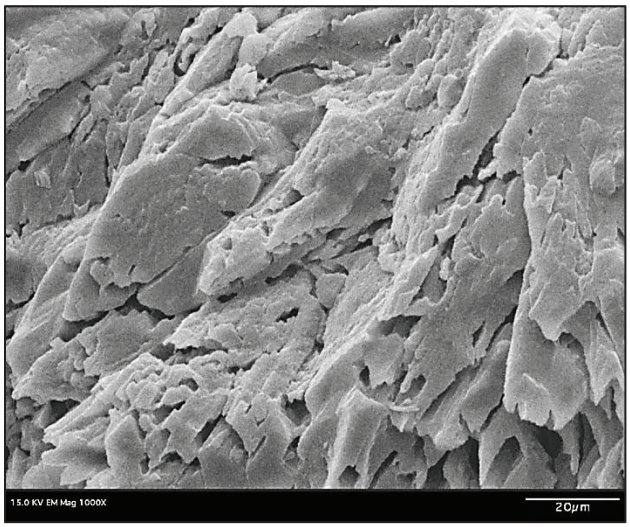

Figure 5-6: SEM image of [1], with a magnification of 1000X.

Energy dispersive spectroscopy was used to confirm the elements in the products as well as check for minute impurities. Because of the tendencies of the material, there can be limitations from the EDS detector. Light atomic elements, such as nitrogen are not well recognized by the detector and not included in the EDS spectra. Also, due to the depth of the continuous X-ray signal there can be overlap of different phases. Spectra of materials [1], [2], and [4] indicate trace amounts of impurities of manganese, aluminum, and silicon possibly due to the 99.3% purity of the magnesium nitrate hexahydrate

starting material. The Fischer Scientific label states that there is 0.001% manganese in the reactant. These impurities did not appear when single crystal diffraction determination and refinement data were collected, and each impurity is in such low amount that their presence is of no importance.

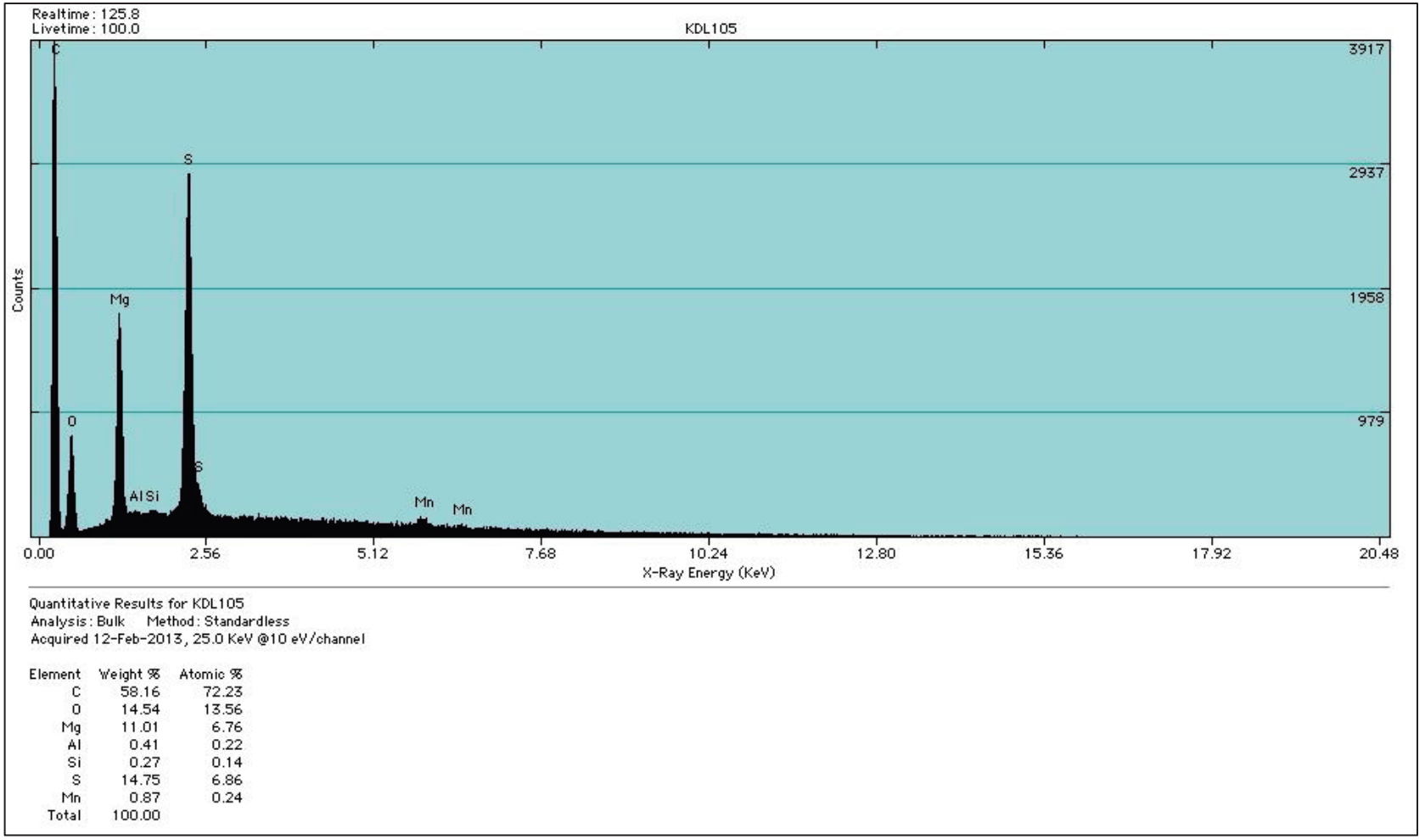

Figure 5-7: EDS spectra of [1] confirms the product contains elements of the starting materials.

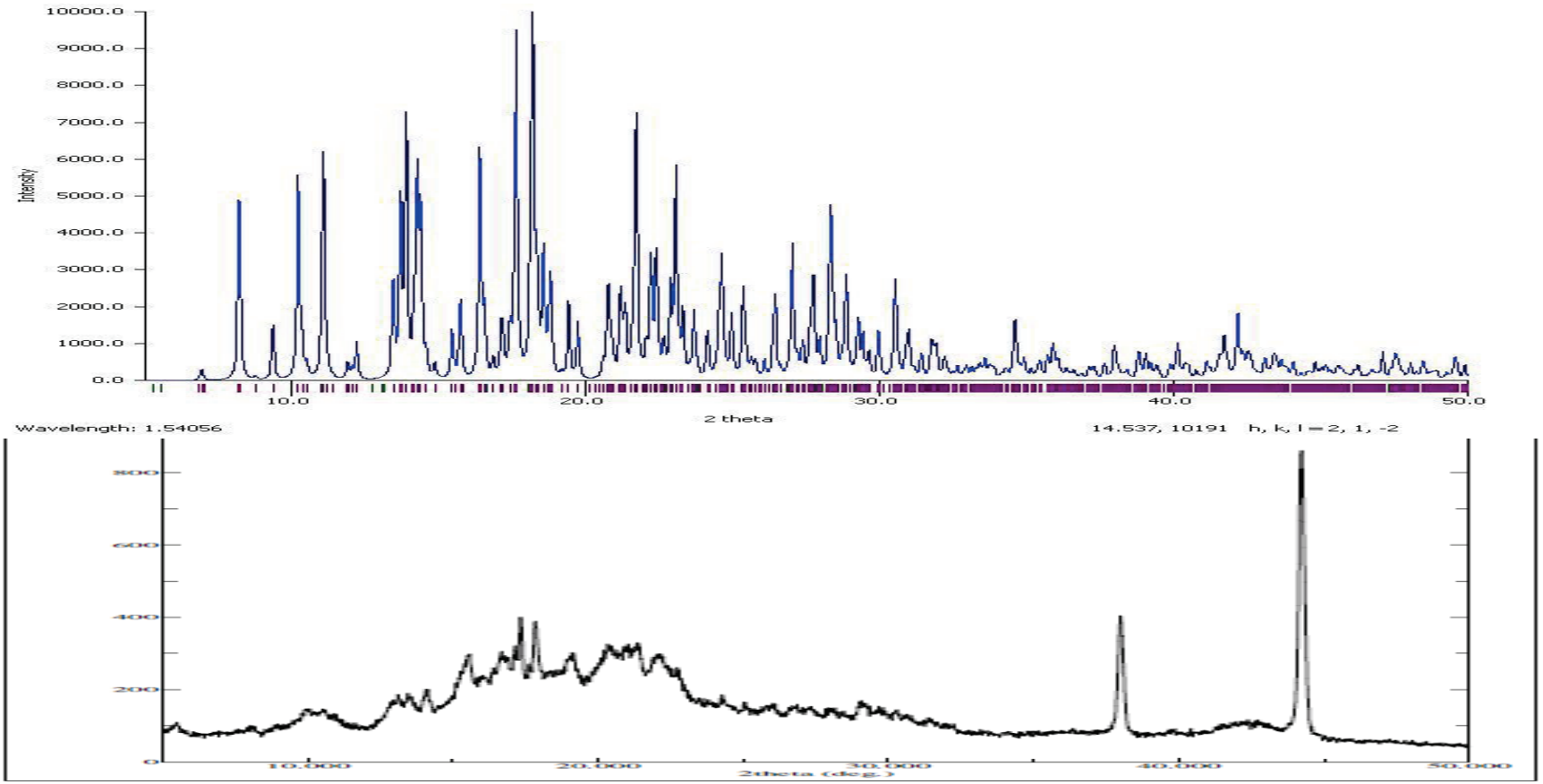

Figure 5-8: Simulated (top) and actual (bottom) PXRD of [1].

Figure 5-8 shows the PXRDs of the simulated and actual graphs of [1]. The simulated (top) PXRD is when the material is in its wet state, it is crystalline and the DMF has not precipitated out. The actual (bottom) PXRD is when the material is dry. As the material dries white precipitate begins to form, and is suggested to be DMF coming out of the material, causing the MOF to de-solvate and become non-crystalline. Because of the large amount of DMF de-solvating and the non-crystallinity of the dry material the PXRDs are difficult to interpret and compare.

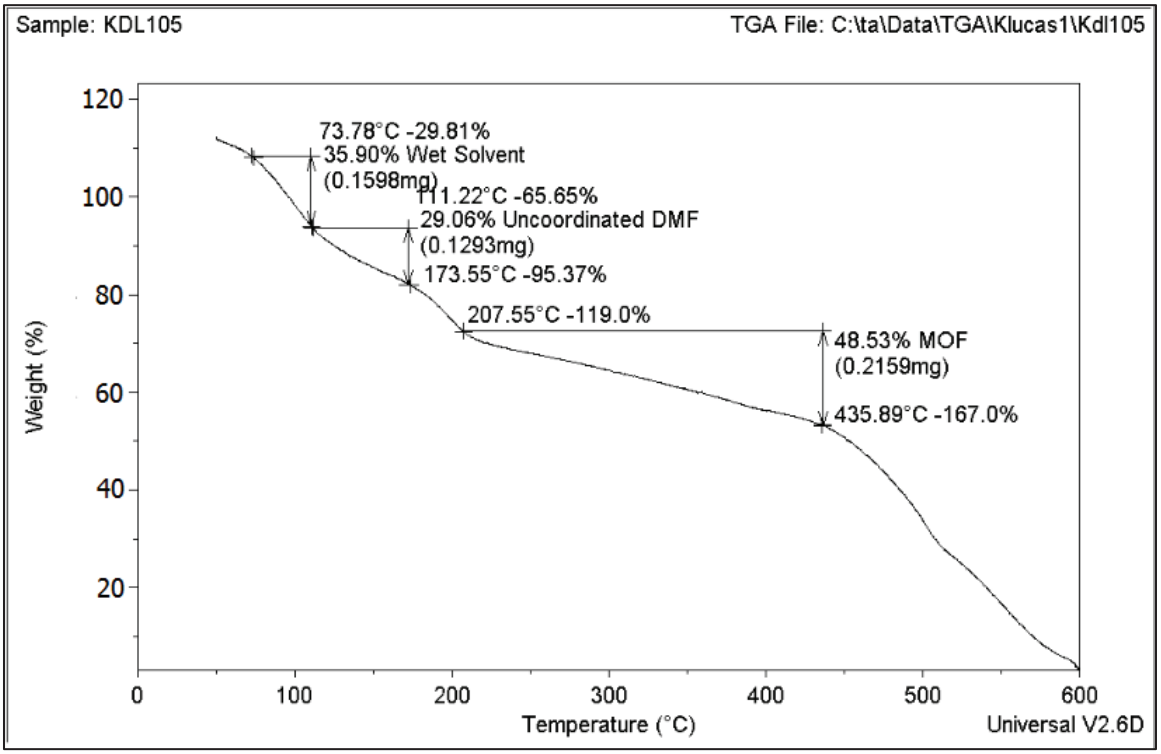

Figure 5-9: TGA of [1].

The TGA above suggests that material [1] decomposes as it is heated. It loses the wet solvent and DMF from ~73°C to ~173°C. It then slowly continues to decompose the MOF, mainly the carboxylates, until ~436°C. Although it has high quality crystal data, the TGA confirms that the material has little stability when heated, and would not be a good MOF for CO_2 adsorption at high temperatures.

5.2.2 $[Mg]_3[SDBA]_3[DMF]_3EtOH$

Synthesis of a magnesium based MOF, $[Mg]_3[SDBA]_3[DMF]_3EtOH$ [2], from magnesium nitrate hexahydrate, 4,4'-sulfonyldibenzoic acid, and 4,4'-bipyridine

[2] was synthesized from magnesium nitrate hexahydrate [$Mg(NO_3)_2 \cdot 6H_2O$], 4,4'-sulfonyldibenzoic acid (SDBA), and 4,4'-bipyridine (Bipy) in DMF and ethanol as seen in Scheme 5-3:

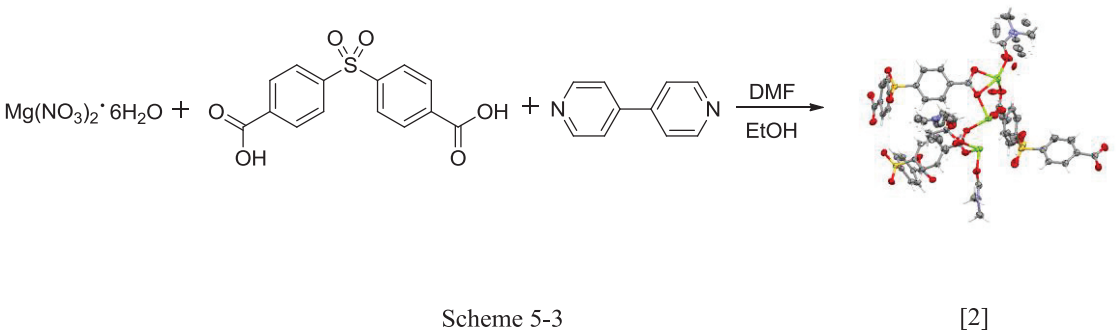

Scheme 5-3 [2]

The carboxylate groups on SBDA are deprotonated under solvothermal conditions as magnesium metal cation binds with the oxides (O^{2-}). The solvents become a part of the product because of intercalation. The ethanol solvent in the mixture is a 1:1 ratio with the DMF solvent. The mixture was stirred in a 23 mL Teflon-lined stainless steel autoclave until all reactants were dissolved and the vessel was sealed and placed in an oven at 160°C for 48 hours. Upon completion of the reaction, the solvent was decanted off and crystals were dried in air resulting in bluish/pink crystals with white precipitate. The crystals de-solvate when left in solution too long, it is suggested that this is due to the DMF acquiring water from the air. The molecular structure of [2] determined by single crystal X-ray analysis is shown in Figure 5-10 and the selected bond lengths and angles are shown in Table 5-5.

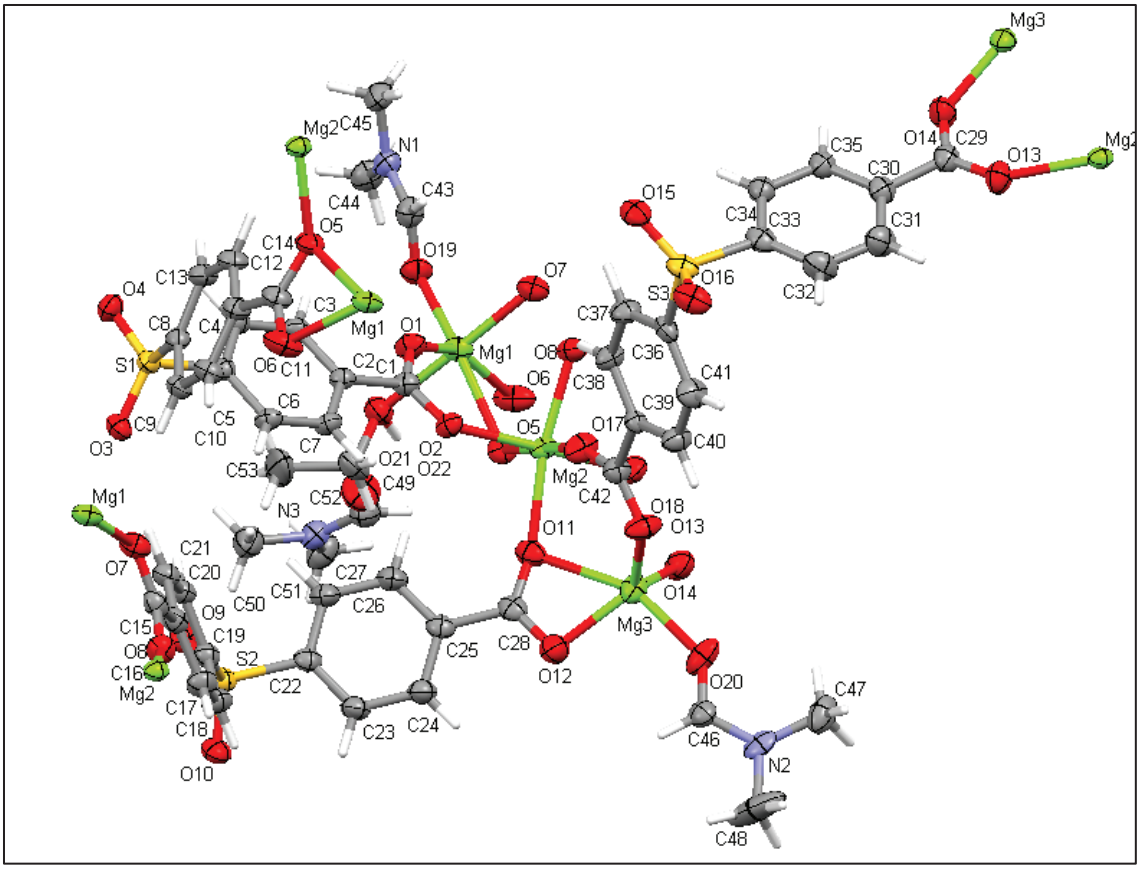

Figure 5-10: Molecular structure of [2] with 50% thermal ellipsoids.

The Mg-O distances for the Mg1 and Mg2 atom range from 1.946(19)-2.0946(17) Å whereas the Mg-O distances for the Mg3 atom range from 2.015(4) -2.103(2) Å. The valence sum of the Mg-O bonds showed that Mg1, Mg2, and Mg3 have a valence of + 2.23, +2.25, and +1.86, respectively, which indicates Mg atoms are in +2 oxidation state.

Table 5-4: Selected Bond Lengths (Å) and Angles (°) for [2].

Bond	Bond Length	Valence
Mg1 O1	1.9893(12)	0.448964791
Mg1 O19	2.0268(12)	0.40569154
Mg1 O7	2.0387(13)	0.392851216
Mg1 O6	2.0822(14)	0.349276331
Mg1 O22	2.162(13)	0.281515557
Mg1 O5	2.2674(12)	0.211732322
Valence Sum	**Mg1**	**2.090031757**
Bond	**Bond Length**	**Valence**
Mg2 O17	2.0193(13)	0.413999
Mg2 O5	2.0464(11)	0.38476
Mg2 O8	2.0508(12)	0.380212
Mg2 O13	2.0826(13)	0.348899
Mg2 O2	2.0928(12)	0.339412
Mg2 O11	2.1731(13)	0.273196
Valence Sum	**Mg2**	**2.140477**
Bond	**Bond Length**	**Valence**
Mg3 O14	1.9435(14)	0.508125
Mg3 O18	1.9544(15)	0.493375
Mg3 O12	2.0002(14)	0.435931
Mg3 O20	2.008(8)	0.426838
Mg3 O11	2.3650(14)	0.16264
Valence Sum	**Mg3**	**2.026909**

Bond Angles	Amplitude	Bond Angles	Amplitude	Bond Angles	Amplitude
O1 Mg1 O19	101.74(5)	O17 Mg2 O5	177.98(7)	O14 Mg3 O18	116.35(8)
O1 Mg1 O7	94.16(5)	O17 Mg2 O8	85.66(6)	O14 Mg3 O12	123.67(6)
O19 Mg1 O7	88.90(5)	O5 Mg2 O8	95.55(5)	O18 Mg3 O12	115.78(8)
O1 Mg1 O6	151.77(5)	O17 Mg2 O13	96.30(7)	O14 Mg3 O20	93.3(4)
O19 Mg1 O6	105.22(5)	O5 Mg2 O13	85.39(5)	O18 Mg3 O20	99.6(8)
O7 Mg1 O6	94.58(6)	O8 Mg2 O13	86.84(5)	O12 Mg3 O20	97.9(9)
O1 Mg1 O22	89.5(3)	O17 Mg2 O2	90.05(6)	O14 Mg3 O11	91.20(5)
O19 Mg1 O22	88.5(3)	O5 Mg2 O2	88.27(5)	O18 Mg3 O11	100.26(6)
O7 Mg1 O22	175.9(3)	O8 Mg2 O2	93.05(5)	O12 Mg3 O11	59.86(5)
O6 Mg1 O22	83.1(3)	O13 Mg2 O2	173.62(5)	O20 Mg3 O11	155.2(9)
O1 Mg1 O5	91.28(5)	O17 Mg2 O11	82.13(6)	O18B Mg3 O11	89.1(4)
O19 Mg1 O5	163.84(5)	O5 Mg2 O11	96.80(5)		
O7 Mg1 O5	99.77(5)	O8 Mg2 O11	166.75(5)		
O6 Mg1 O5	60.79(4)	O13 Mg2 O11	89.39(5)		
O22 Mg1 O5	82.0(3)	O2 Mg2 O11	92.09(5)		

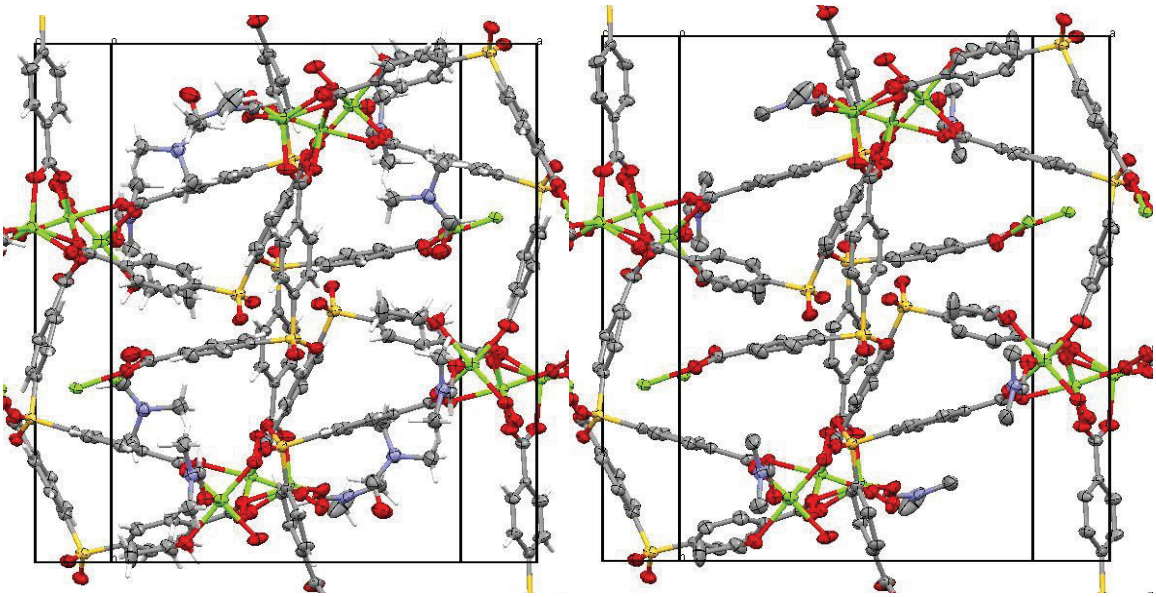

Figure 5-11: Extended structure of [2] along the *c**-axis (50% thermal ellipsoids). The uncoordinated DMF molecules along with the hydrogen bonds were eliminated in right image for clarity. For elements: nitrogen (blue), carbon (gray), oxygen (red), sulfur (yellow), and magnesium (green).

If the uncoordinated DMF molecules are able to be taken out of the structure then there will be more space for possible gas adsorption, Figure 5-11. The formation of crystal [2] is isostructural to known zinc MOF by Li *et al.* The molecular structure consists of three independent magnesium atoms that are arranged in a linear trinuclear cluster (Mg trimer), three coordinated SDBA molecules, two coordinated DMF molecules, one uncoordinated DMF molecule, and a coordinated ethanol molecule. The molecular and extended structures follow the same pattern as [1] in terms of connectivity and metal to ligand bonding.

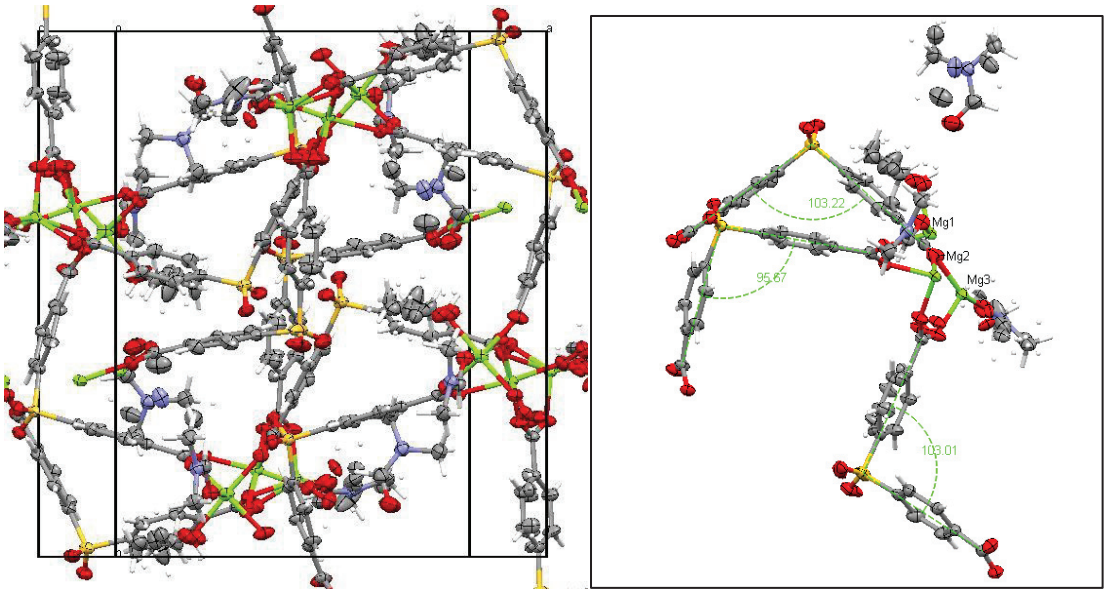

Figure 5-12: Packed cell of [2] with view along *c**-axis (left) and then the dihedral angles in the unit cell of [2] with thermal ellipsoids at 50% (right).

Table 5-5: Dihedral angles of [2].

Linker	Atoms	Angle
SDBA(1) of Mg1	C1 S1 C14	95.67
SDBA(2) of Mg2	C15 S2 C28	103.22
SDBA(3) of Mg3	C29 S3 C42	103.01

The disorder that is noticed within the packed cell of [2] is due to the ethanol solvent, Figure 5-12. There is also a disordered phenylene ring because of the flexibility of the structure. The dihedral angles of [2] are 95.67°, 103.22°, and 103.01° from Mg1 to Mg3, respectively, and are slightly different than [1] because of the solvents utilized in the reaction and then seen in the product. It is noticed that there is more flexibility with a less polar solvent and that creates slightly larger angles.

The presence of macro-voids in the system suggested that larger porosity could be engendered with less DMF solvent. It is known from papers that other solvents were used

to create Mg-MOFs in previous research.[4,15-23] It was assumed that since SDBA dissolves into DMF, another solvent could be added and the reaction would take place.

Once under the SEM, Figure 5-13(a) shows a magnification at 133X and gives the illusion that there are multiple phases in the material. Figure 5-13(b) reveals that there are more rod-like fragments protruding from the layer underneath, and the sample could have different products. There are long rods that cover the main part of the material, which cover a solid crystalline-type area.

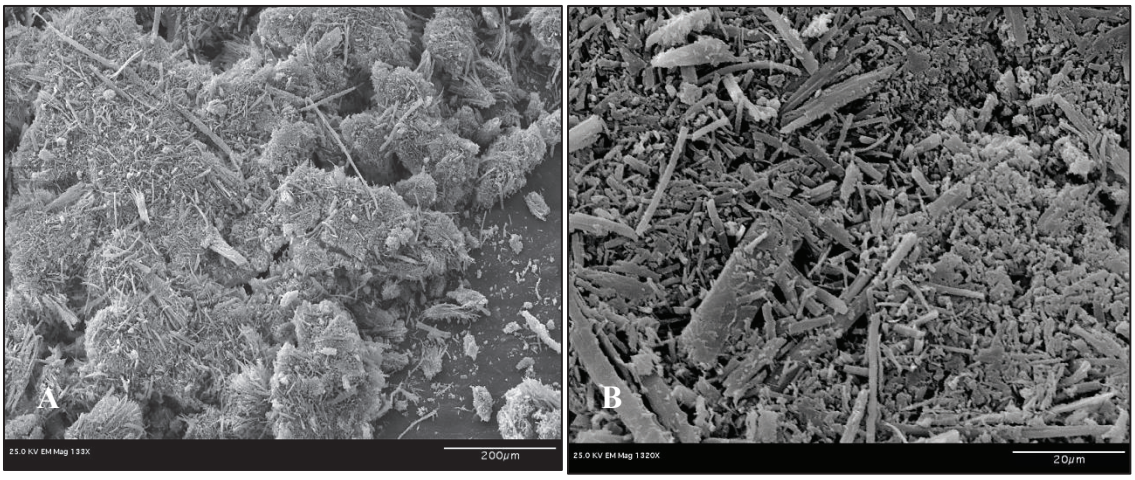

Figure 5-13: SEM images of [2].

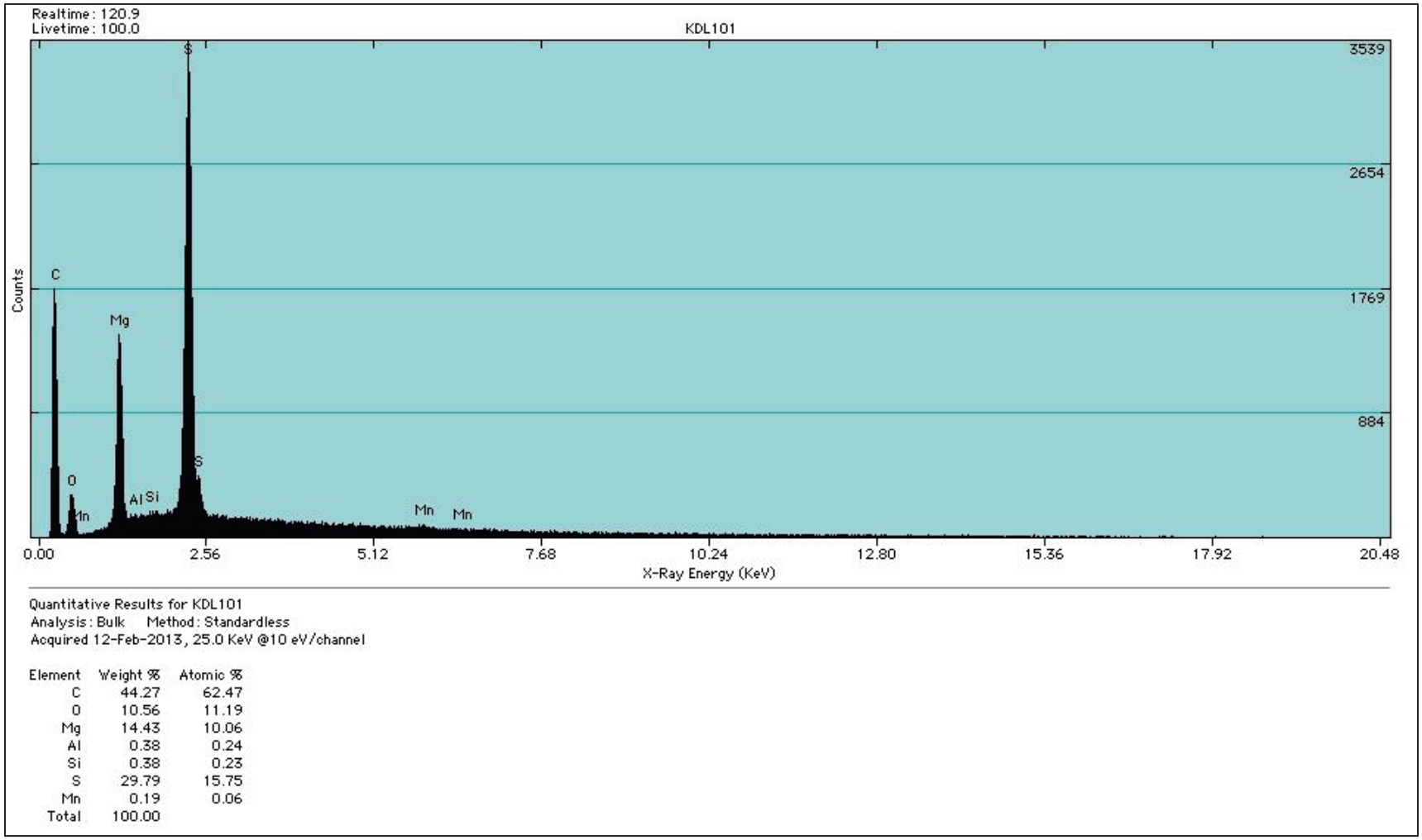

Figure 5-14: EDS spectra of [2].

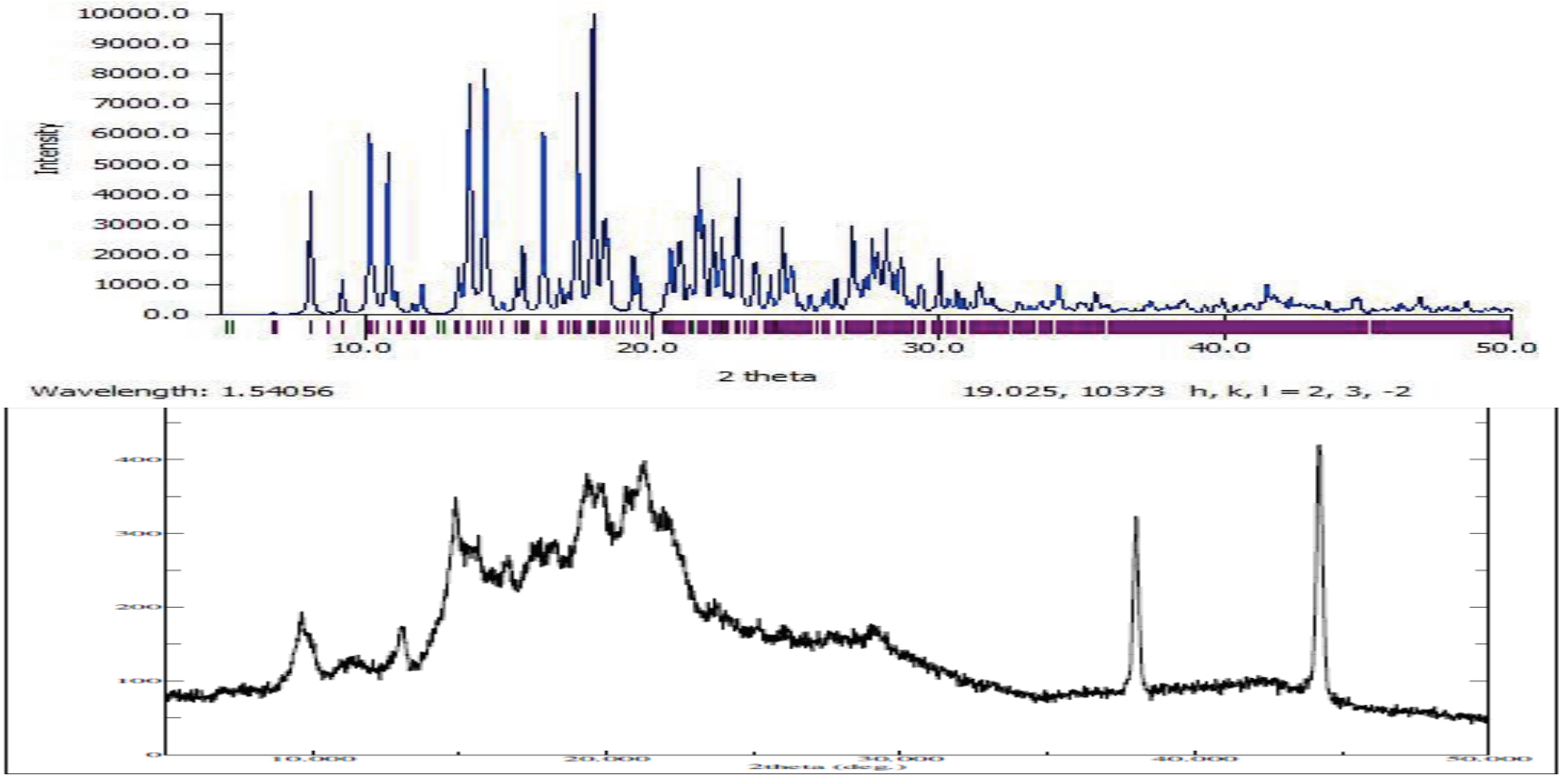

Figure 5-15: Simulated (top) and actual (bottom) PXRD of [2].

The PXRDs of [2] in Figure 5-15 show the simulated and actual graphs of the material. As in [1], it is difficult to see the similarities between the graphs because of the DMF that de-solvates when the material is dried. It is suggested that the crystal DMF will de-solvate when in air for a period of time, approximately 1-2 hours. The de-solvation of the DMF causes the material to become non-crystalline and results in low quality PXRD graphs. Also, it is possible that [2] undergoes a phase change when dried in air. The PXRD peaks do not seem to correlate but they differ where important peaks should be showing in the actual compared to the simulated graphs.

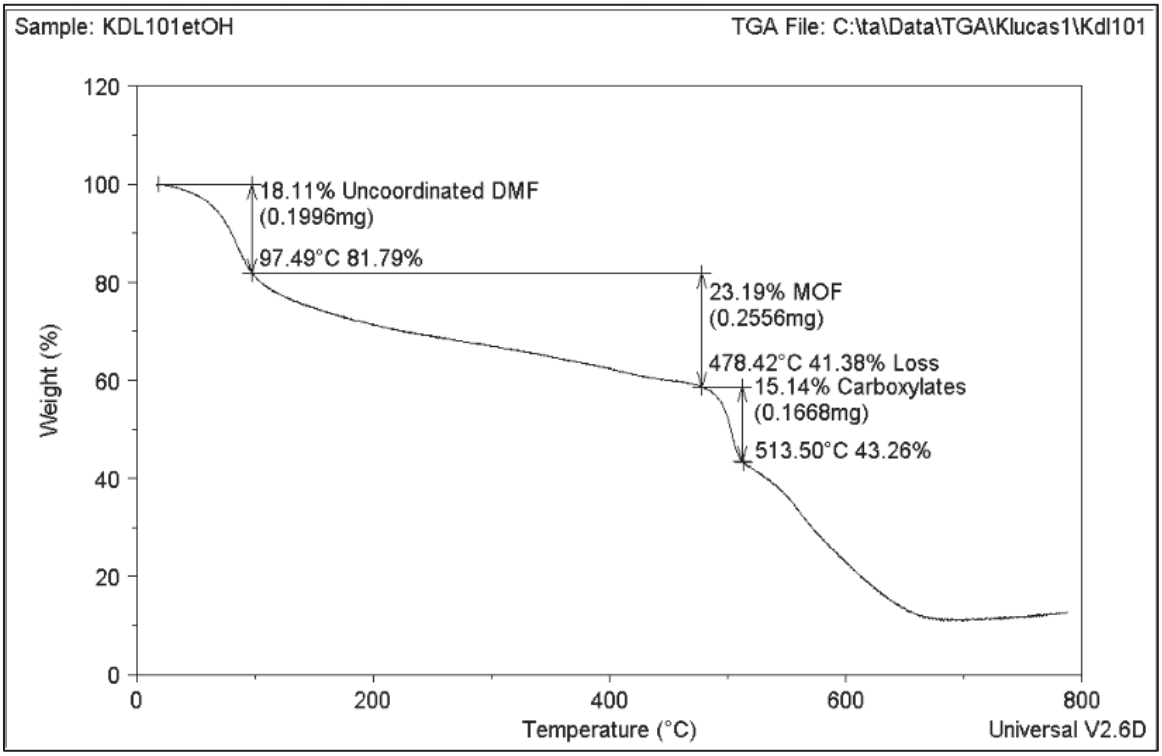

Figure 5-16: TGA of [2].

The TGA in Figure 5-16 shows the decomposition of [2] from room temperature to 780°C. It is suggested that the MOF is more stable in an ethanol/DMF solvent than in the methanol/DMF solvent. In each MOF the uncoordinated DMF and the wet solvent are decomposed first as the material is heated. The MOF [2] decomposes over a longer

period of time than [1] and a higher range of temperature (from 97.49°C-478.42°C). We propose that the carboxylates decompose at approximately 513.50°C.

5.2.3 $[Mg]_3[SDBA]_3[DMF]_3EtOH{\cdot}H_2O$

Synthesis of a magnesium based MOF, $[Mg]_3[SDBA]_3[DMF]_3EtOH{\cdot}H_2O$ [3], from magnesium nitrate hexahydrate, 4,4'-sulfonyldibenzoic acid, and 4,4'-bipyridine

[3] was synthesized from magnesium nitrate hexahydrate [$Mg(NO_3)_2{\cdot}6H_2O$], 4,4'-sulfonyldibenzoic acid (SDBA), and 4,4'-bipyridine (bipy) in DMF, ethanol, and distilled water as seen in Scheme 5-4:

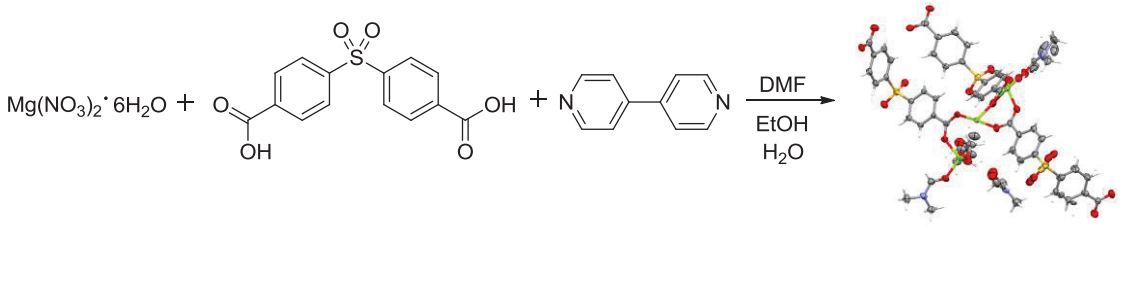

Scheme 5-4 [3]

The reaction follows the same path as material [2], however there is distilled water added as a co-solvent. The water is shown in the product coordinated to a magnesium atom along with the ethanol solvent. The mixture was stirred in a 23 mL Teflon-lined stainless steel autoclave until all reactants were dissolved and the vessel was sealed and placed in an oven at 160°C for 48 hours. Upon completion of the reaction, the solvent was decanted off and crystals were kept in a sealed vial at room temperature. The molecular structure of [3] determined by single crystal X-ray analysis is shown in Figure 5-17 and the selected bond lengths and angles are shown in Table 5-7.

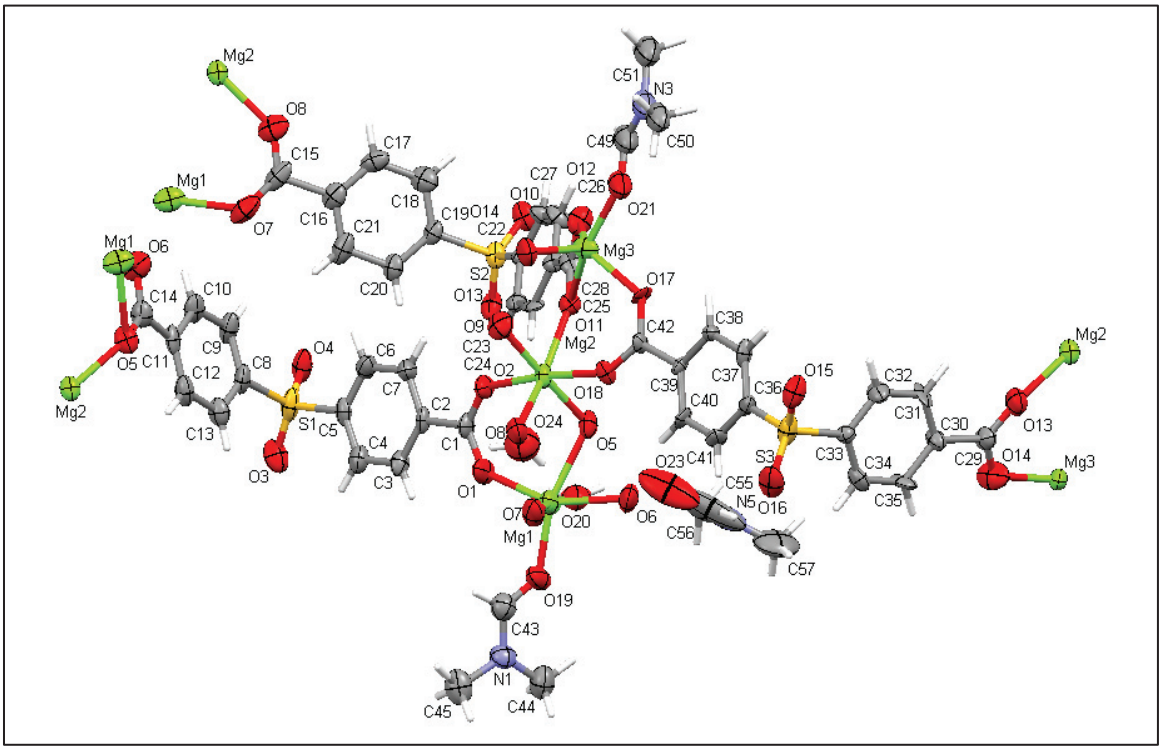

Figure 5-17: Molecular structure of [3] with 50% thermal ellipsoids.

As shown in Figure 5-17, the molecular structure consists of three independent magnesium atoms that are arranged in a coplanar trinuclear cluster (Mg trimer), three coordinated SDBA molecules, two coordinated DMF molecules, one uncoordinated DMF molecule, a coordinated ethanol solvent molecule, and a coordinated water solvent molecule. Each metal cation has a +1.97, +2.17, and +2.18 charge from Mg1-Mg3, respectively, which indicates the Mg atoms are in a +2 oxidation state.

Table 5-6: Selected Bond Lengths (Å) and Angles (°) for [3].

Bond	Bond Length	Valance
Mg1 O1	1.9832(19)	0.456428
Mg1 O7	2.031(2)	0.401112
Mg1 O6	2.072(2)	0.359039
Mg1 O5	2.2541(19)	0.219482
Mg1 C14	2.471(3)	0.122126
Mg1 O19	2.0192(19)	0.414111
Valence Sum	**Mg1**	**1.972298**
Bond	**Bond Length**	**Valence**
Mg2 O13	2.020(2)	0.413216
Mg2 O5	2.0485(17)	0.382583
Mg2 O8	2.0493(18)	0.381756
Mg2 O2	2.0864(18)	0.345334
Mg2 O11	2.153(2)	0.288447
Mg2 O18	2.0727(19)	0.35836
Valence Sum	**Mg2**	**2.169697**
Bond	**Bond Length**	**Valence**
Mg3 O14	1.944(2)	0.507439
Mg3 O12	1.973(2)	0.469186
Mg3 O11	2.403(2)	0.146766
Mg3 O21	1.923(8)	0.537073
Mg3 O17	1.937(2)	0.517131
Valence Sum	**Mg3**	**2.177594**

Bond Angles	Amplitude	Bond Angles	Amplitude	Bond Angles	Amplitude
O1 Mg1 O19	102.25(8)	O13 Mg2 O5	178.28(10)	O21 Mg3 O17	101.3(5)
O1 Mg1 O7	94.71(9)	O13 Mg2 O8	86.06(9)	O21 Mg3 O14	102.4(5)
O19 Mg1 O7	89.72(8)	O5 Mg2 O8	95.56(8)	O17 Mg3 O14	115.39(11)
O1 Mg1 O6	152.34(8)	O13 Mg2 O18	95.32(10)	O21 Mg3 O12	86.7(5)
O19 Mg1 O6	103.81(8)	O5 Mg2 O18	85.33(8)	O17 Mg3 O12	123.85(10)
O7 Mg1 O6	94.54(8)	O8 Mg2 O18	87.05(8)	O14 Mg3 O12	116.73(12)
O1 Mg1 O20	88.0(5)	O13 Mg2 O2	90.85(9)	O21 Mg3 O11	145.0(5)
O19 Mg1 O20	87.2(5)	O5 Mg2 O2	88.51(7)	O17 Mg3 O11	90.88(8)
O7 Mg1 O20	176.3(4)	O8 Mg2 O2	93.37(7)	O14 Mg3 O11	101.56(9)
O6 Mg1 O20	84.2(6)	O18 Mg2 O2	173.83(8)	O12 Mg3 O11	59.72(8)
O1 Mg1 O5	91.89(7)	O13 Mg2 O11	82.25(9)		
O19 Mg1 O5	162.79(8)	O5 Mg2 O11	96.18(8)		
O7 Mg1 O5	98.96(8)	O8 Mg2 O11	167.37(9)		
O6 Mg1 O5	60.91(7)	O18 Mg2 O11	89.29(8)		
O20 Mg1 O5	83.4(5)	O2 Mg2 O11	91.57(8)		

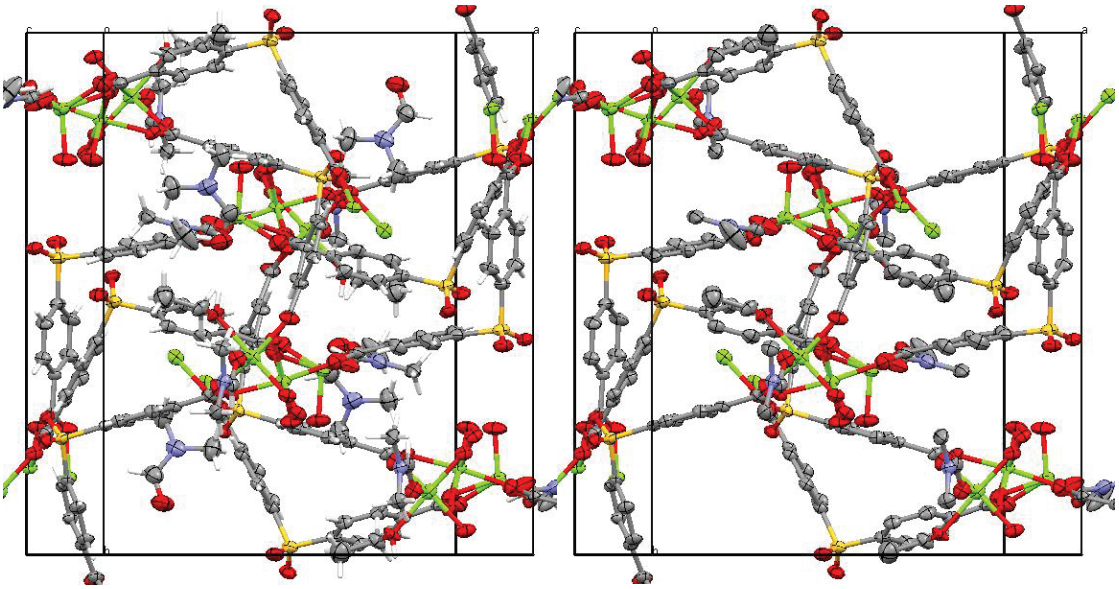

Figure 5-18: Extended structure of [3] along the *c**-axis (50% thermal ellipsoids). The uncoordinated DMF molecules along with the hydrogen bonds were eliminated in bottom image for clarity. For elements: nitrogen (blue), carbon (gray), oxygen (red), sulfur (yellow), and magnesium (green).

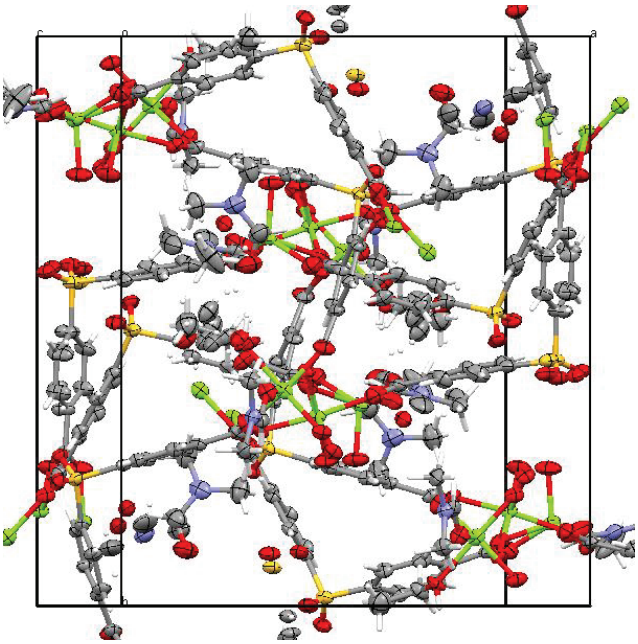

Figure 5-19: Packed cell of [3] with view along *c**-axis.

Materials [2] and [3] are closely related, and the only differences in the structures are the additional water solvent molecule, the disorder, and the dihedral angles due to the flexibility and variation of solvents. There is slightly more disorder in the structure because of the disordered water molecule. The dihedral angles of the organic linkers in [3] have slight differences than the values in the previous materials, [1] and [2]. The angle values are 95.90°, 103.03°, and 102.71° from the Mg1 to Mg3 metal cation, respectively. The differences are noticeable due to the disorder of the solvent molecules. The addition of the water solvent molecule creates strain on the organic linkers and causes the dihedral angle of SDBA (3) to be less than the dihedral angle of SDBA (3) in material [2]. A summary of the dihedral angles can be seen in Table 5-8.

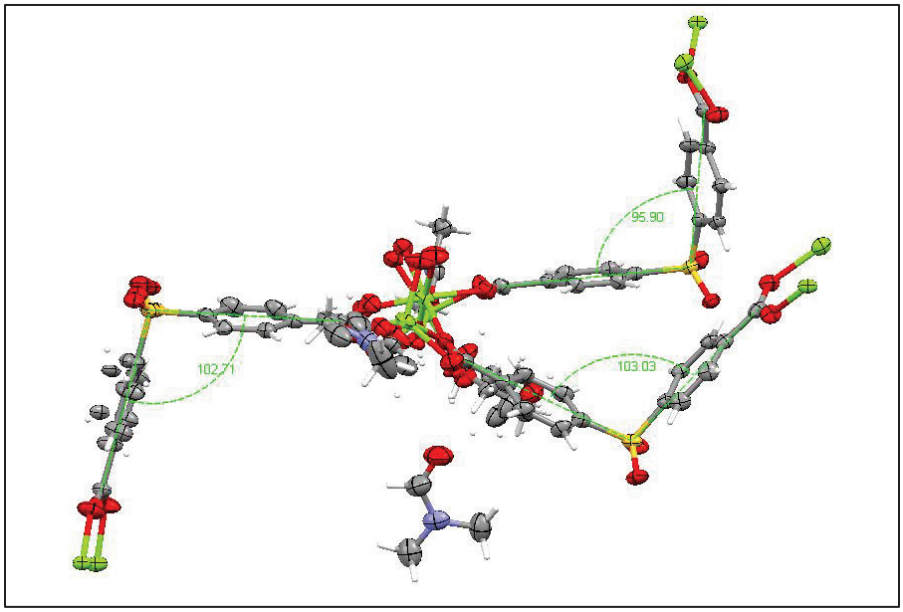

Figure 5-20: Molecular structure showing dihedral angles of [3].

Table 5-7: Dihedral angles of [3].

Linker	Atoms	Angle
SDBA(1) of Mg1	C1 S1 C14	95.90
SDBA(2) of Mg2	C15 S2 C28	103.03
SDBA(3) of Mg3	C29 S3 C42	102.71

5.2.4 $[Mg]_3[SDBA]_3[DMF]_4$

Synthesis of a magnesium based MOF, $[Mg]_3[SDBA]_3[DMF]_4$ [4], from magnesium nitrate hexahydrate, 4,4'-sulfonyldibenzoic acid, and 4,4'-bipyridine.

[4] was synthesized from magnesium nitrate hexahydrate [$Mg(NO_3)_2 \cdot 6H_2O$], 4,4'-sulfonyldibenzoic acid (SDBA), and 4,4'-bipyridine (Bipy) in DMF as seen in Scheme 5-5:

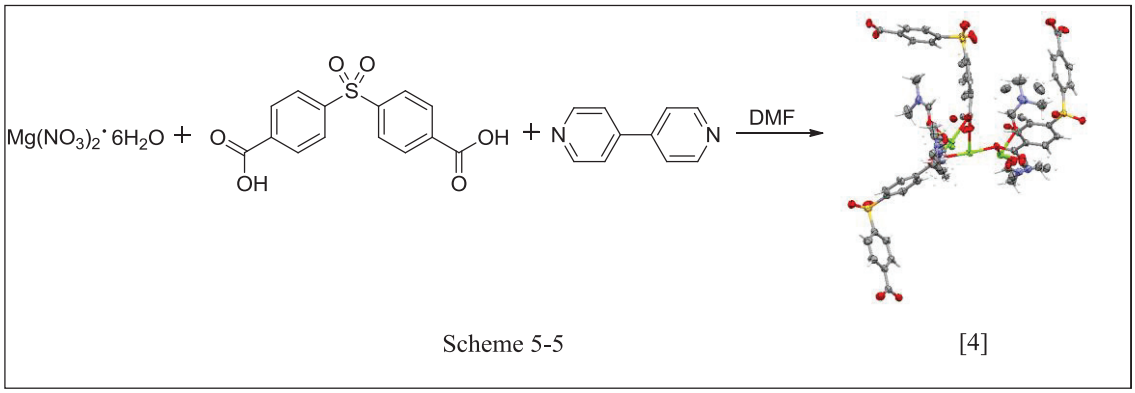

Scheme 5-5 [4]

The carboxylate groups on SBDA are deprotonated under solvothermal conditions as magnesium metal cation binds with the oxides (O^-). The mixture was stirred in a 23 mL Teflon-lined stainless steel autoclave until reactants were dissolved and the vessel was sealed and placed in an oven at 160°C for 48 hours. DMF was the only solvent used in the reaction. Upon completion of the reaction, the solvent was decanted off and crystals were dried under vacuum, resulting in purple crystals along with some unidentified white precipitate. The molecular structure of [4] determined by single crystal X-ray analysis is shown in Figure 5-21 and the selected bond lengths and angles are shown in Table 5-9.

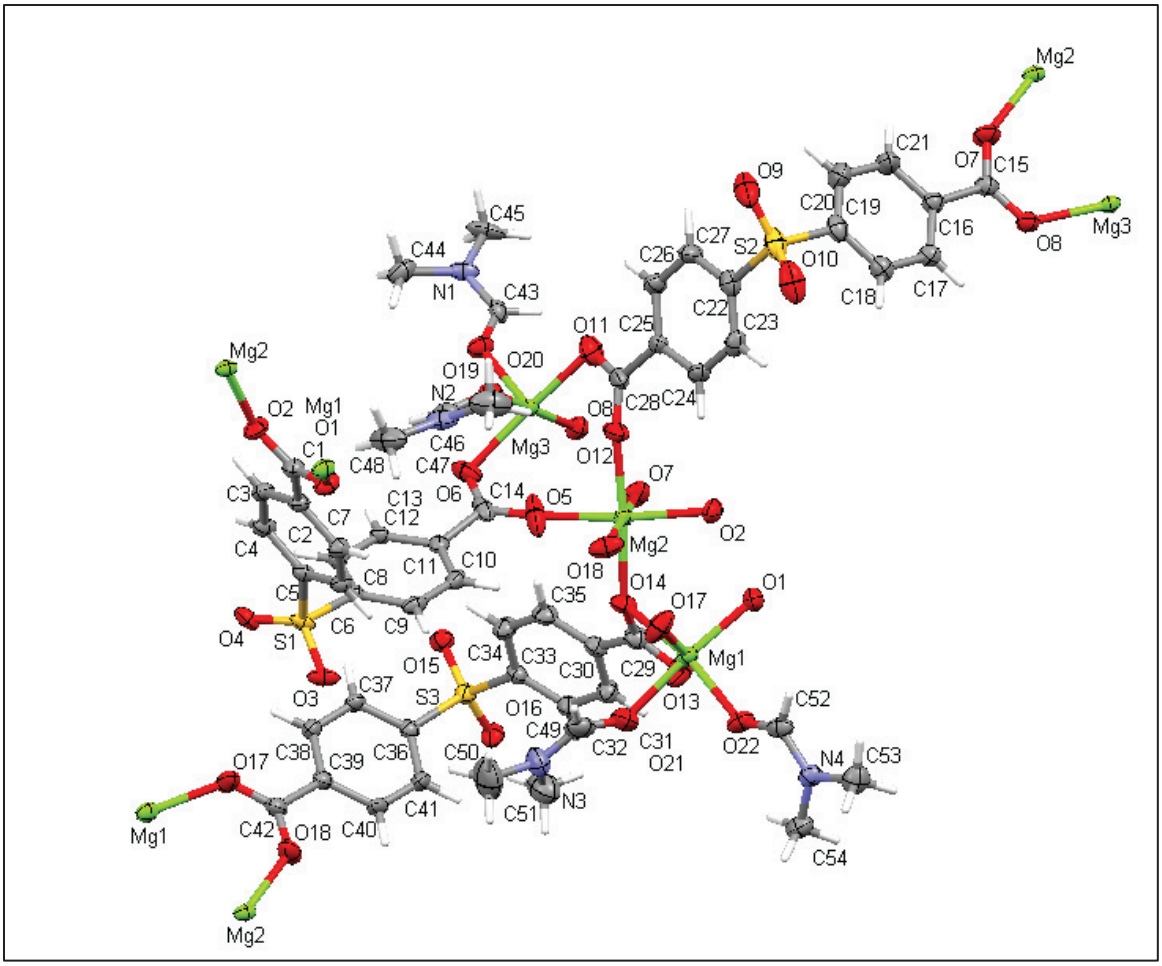

Figure 5-21: Molecular structure of [4] with no disorder and thermal ellipsoids at 50%.

The structure of [4] is a three-dimensional framework consisting of magnesium ions, SDBA ligands, coordinated and uncoordinated DMF solvent molecules. As shown in Figure 5-22, the extended structure consists of three independent magnesium atoms that are arranged in a linear trinuclear cluster (Mg trimer), three coordinated SDBA molecules, and four DMF molecules.

The Mg-O distances for the Mg1 and Mg2 atom range from 1.9946(19)-2.0946(17) Å whereas the Mg-O distances for the Mg3 atom range from 2.015(4) - 2.103(2) Å. The valence sum of the Mg-O bonds showed that Mg1, Mg2, and Mg3 have

a valence of + 2.23, +2.25, and +1.86, respectively, which indicates Mg atoms are in +2 oxidation state.

Table 5-8: Selected Bond Lengths (Å) and Angles (°) for [4].

Bond	Bond Length	Valence
Mg1 O21	2.063(5)	0.3678794
Mg1 O22	2.020(4)	0.4132164
Mg1 O14	2.2400(18)	0.2280071
Mg1 O13	2.094(2)	0.338313
Mg1 O17	1.9946(19)	0.4425795
Mg1 O1	1.9966(17)	0.4401936
Valence Sum	**Mg1**	**2.2301892**
Bond	**Bond Length**	**Valence**
Mg2 O5	2.038(3)	0.3935952
Mg2 O2	2.0811(17)	0.3503163
Mg2 O7	2.0186(18)	0.4147829
Mg2 O12	2.0516(19)	0.3793905
Mg2 O14	2.0946(17)	0.3377648
Mg2 O18	2.0566(18)	0.3742981
Valence Sum	**Mg2**	**2.2501478**
Bond	**Bond Length**	**Valence**
Mg3 O6	2.069(2)	0.361962
Mg3 O8	2.0472(19)	0.383929
Mg3 O11	2.062(2)	0.368875
Mg3 O20	2.103(2)	0.330183
Mg3 O19	2.015(4)	0.418838
Valence Sum	**Mg3**	**1.863787**

Bond Angles	Amplitude	Bond Angles	Amplitude	Bond Angles	Amplitude
O17 Mg1 O1	95.90(9)	O7 Mg2 O5	90.91(16)	O19 Mg3 O6	95.4(2)
O17 Mg1 O22	103.23(18)	O7 Mg2 O12	91.39(9)	O8 Mg3 O6	97.08(8)
O1 Mg1 O22	93.02(17)	O5 Mg2 O12	86.15(12)	O11 Mg3 O6	165.97(10)
O17 Mg1 O21	94.16(17)	O7 Mg2 O18	175.07(9)	O19 Mg3 O20	93.02(12)
O1 Mg1 O21	169.93(17)	O5 Mg2 O18	86.57(16)	O8 Mg3 O20	171.46(8)
O22 Mg1 O21	84.1(2)	O12 Mg2 O18	92.66(9)	O11 Mg3 O20	83.51(8)
O22B Mg1 O13	107.6(13)	O7 Mg2 O2	88.70(8)	O6 Mg3 O20	85.44(8)
O17 Mg1 O13	154.17(8)	O5 Mg2 O2	174.35(12)	O19 Mg3 O5	148.9(2)
O1 Mg1 O13	94.57(9)	O12 Mg2 O2	88.22(8)	O8 Mg3 O5	92.22(11)
O22 Mg1 O13	99.72(16)	O18 Mg2 O2	94.23(8)	O11 Mg3 O5	116.13(11)
O21 Mg1 O13	76.47(18)	O7 Mg2 O14	86.18(7)	O6 Mg3 O5	53.61(10)
O17 Mg1 O14	94.82(7)	O5 Mg2 O14	88.93(12)	O20 Mg3 O5	82.68(12)
O1 Mg1 O14	96.33(7)	O12 Mg2 O14	174.48(9)	O19 Mg3 O12	146.0(2)
O22 Mg1 O14	158.70(14)	O18 Mg2 O14	89.54(7)	O8 Mg3 O12	94.43(7)
O21 Mg1 O14	83.39(15)	O2 Mg2 O14	96.66(7)	O11 Mg3 O12	53.15(7)
O13 Mg1 O14	60.54(7)	O19 Mg3 O8	94.85(12)	O6 Mg3 O12	115.74(9)
		O19 Mg3 O11	93.8(2)	O20 Mg3 O12	77.17(7)
		O8 Mg3 O11	92.68(8)	O5 Mg3 O12	62.97(10)

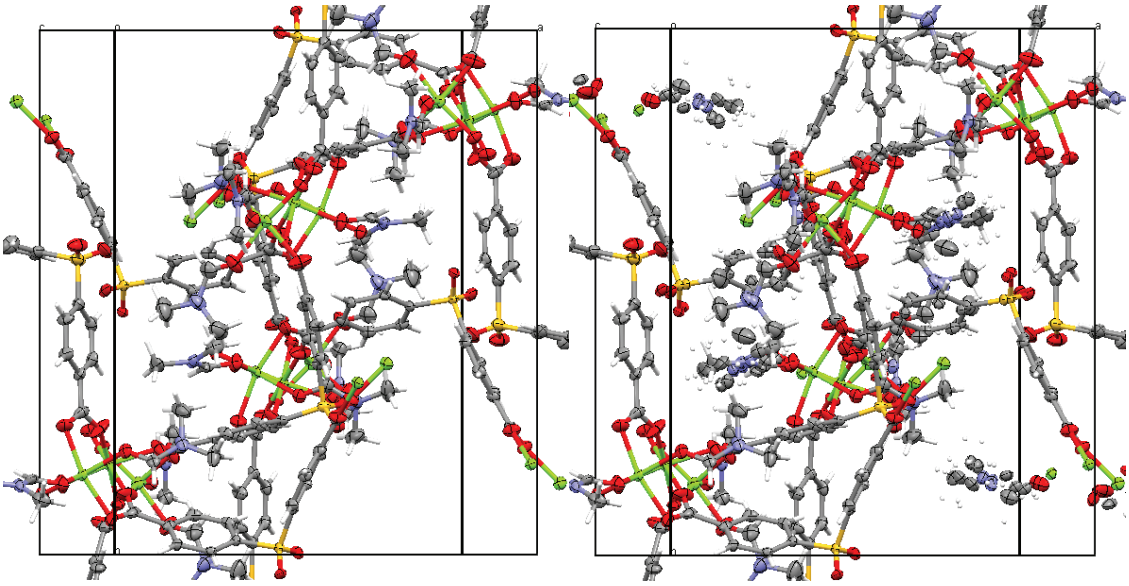

Figure 5-22: Extended structure of [2] along the *c**-axis (left image, 50% thermal ellipsoids). Extended structure of [4] showing disorder (right image, thermal ellipsoids at 50%). For elements: nitrogen (blue), carbon (gray), oxygen (red), sulfur (yellow), and magnesium (green). There are no uncoordinated DMF molecules, that are not disordered, which can be eliminated from the structure. It is suggested that due to the way the crystal structure formed there are two major channels instead of four smaller ones as in the previous structures.

The disorder in the structure, shown in Figure 22 (right), demonstrates the limited space when the uncoordinated disordered DMF molecule is in the structure. Further research is needed to discover a process to remove the uncoordinated DMF molecules without collapsing the framework or de-solvation of the coordinated DMF. Due to the solvent only being DMF the structure is flexible and the most stable of the four MOFs produced. The dihedral angles are measured at 104.11°, 104.46°, and 99.36° from Mg1 to Mg3, respectively, shown in Figure 5-23. A summary of the measured angles can be found in Table 5-10. The dihedral angles of [4] are different then the repeating angle

pattern of the previous materials. The third organic linker dihedral angle is the smallest of the three and not the first as it is for the other MOFs. Also the other two angles are the largest that has been measured so far. It suggests that there is more flexibility within the structure.

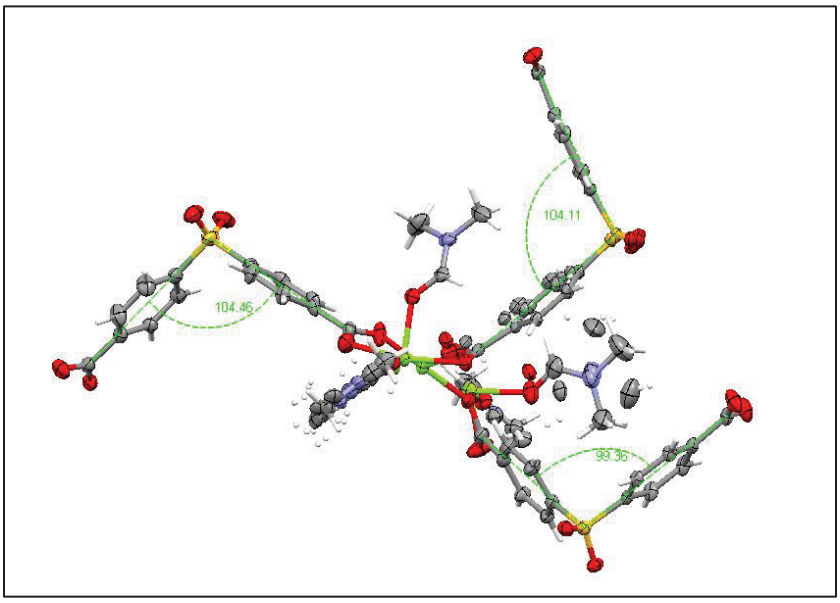

Figure 5-23: Dihedral angles in unit cell of [4] with thermal ellipsoids at 50%.

Table 5-9: Dihedral and Torsion Angles of [4].

Linker	Atoms	Angle
SDBA (Mg1)	C1 S1 C14	104.11
SDBA (Mg2)	C15 S2 C28	104.46
SDBA (Mg3)	C29 S3 C42	99.36

Figure 5-24 contains images of material [4] and was predicted to be a three-dimensional Mg-MOF. The solvent used in the reaction was DMF, with the goal to create voids within the material to adsorb gas molecules. Figure 5-24 (a) and (b) have a magnification of 150X and 1000X, respectively. In Figure 5-24(b), the ridges seem to resemble cracks in the material i.e. stress-related, but the black spots are macro-voids and are examined more closely.

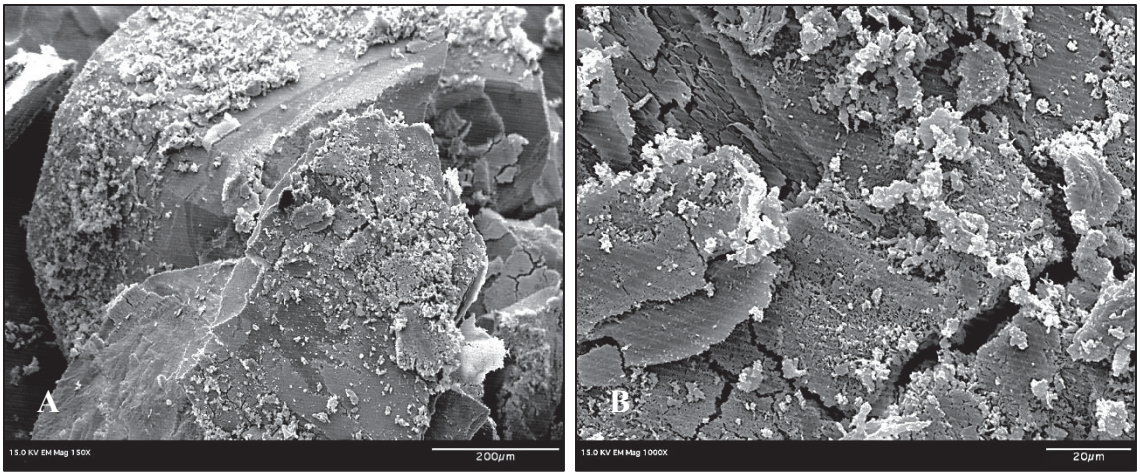

Figure 5-24: SEM images of [4].

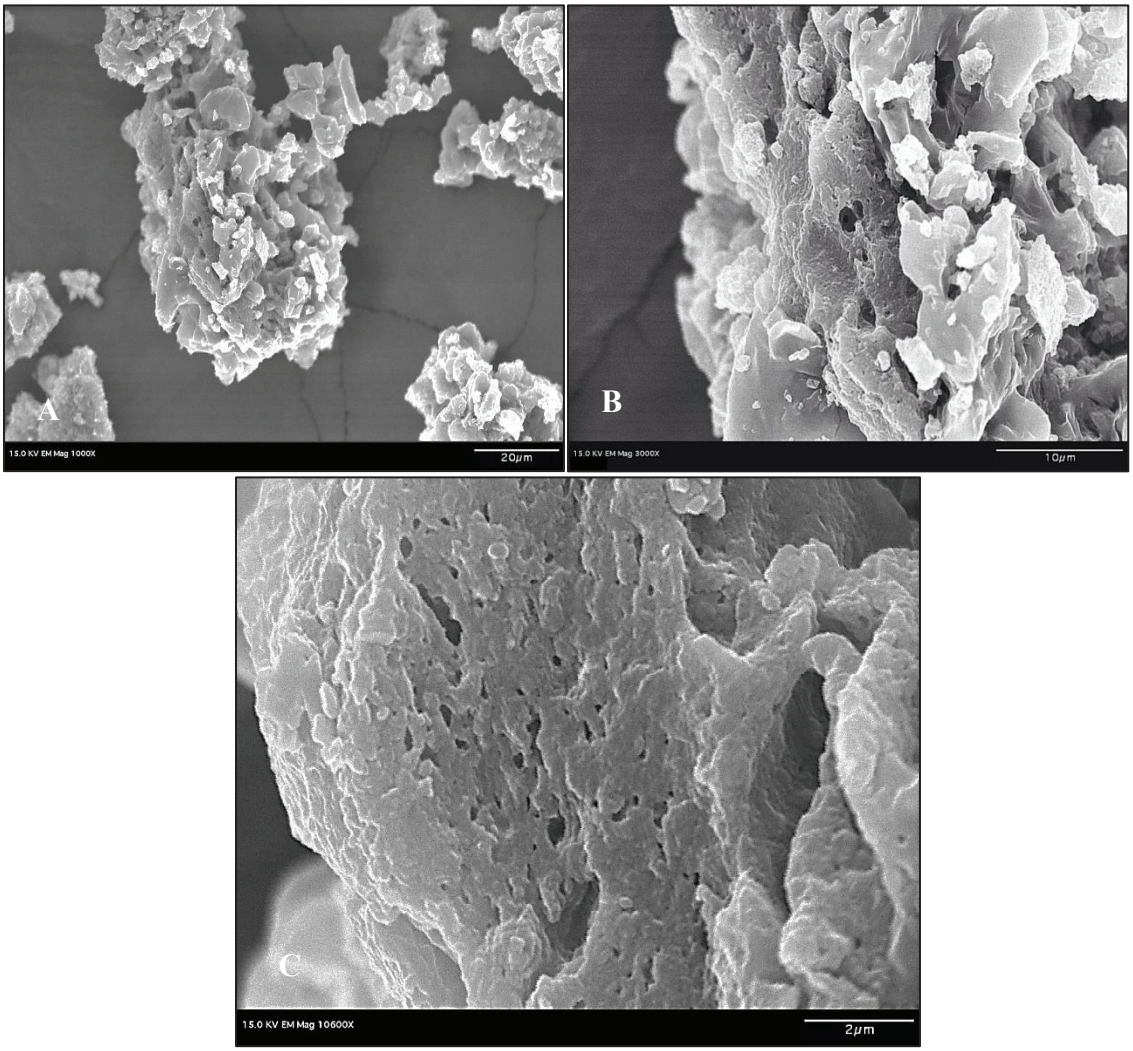

Figure 5-25: SEM images of [4] macro-voids.

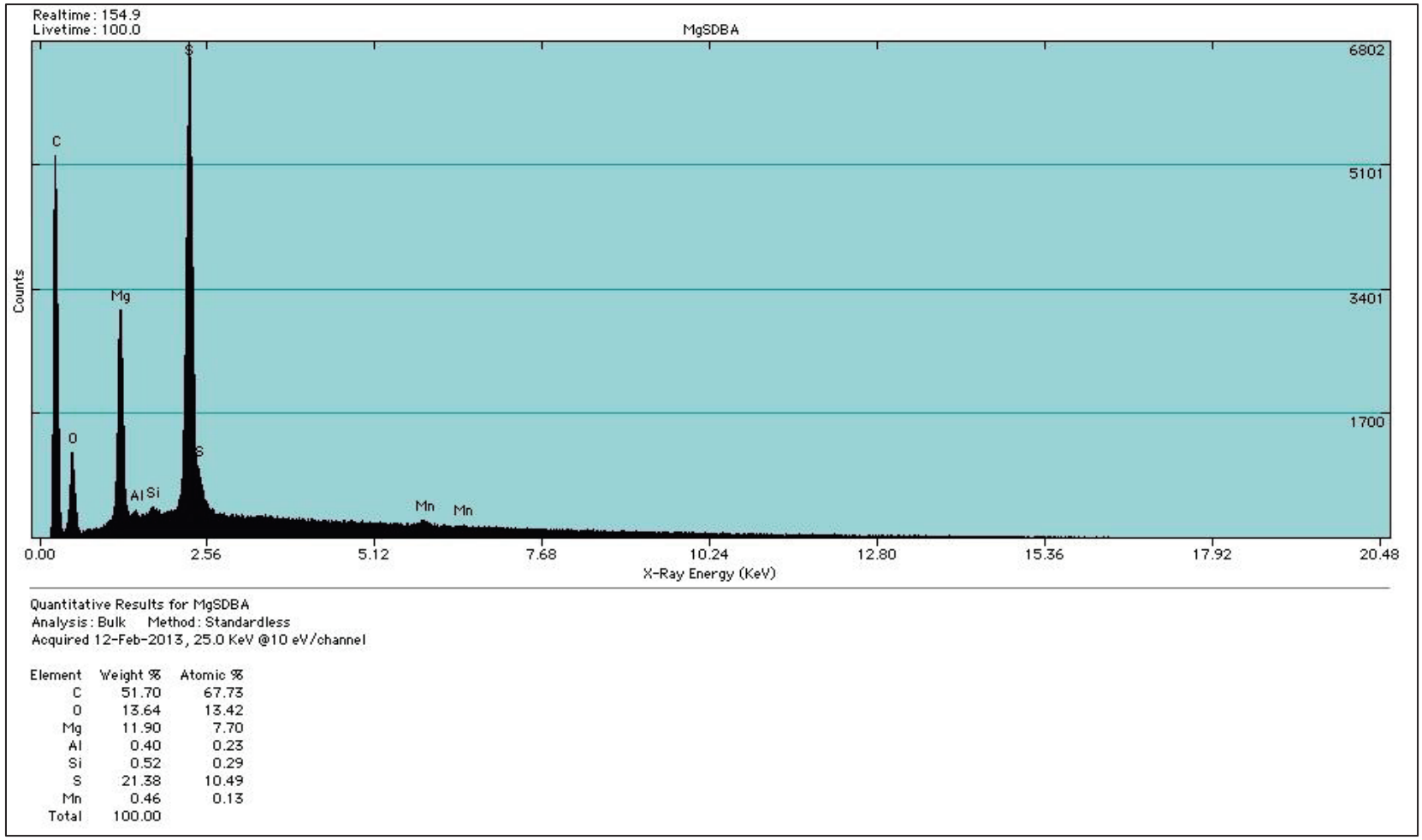

Figure 5-26: EDS spectra of [4].

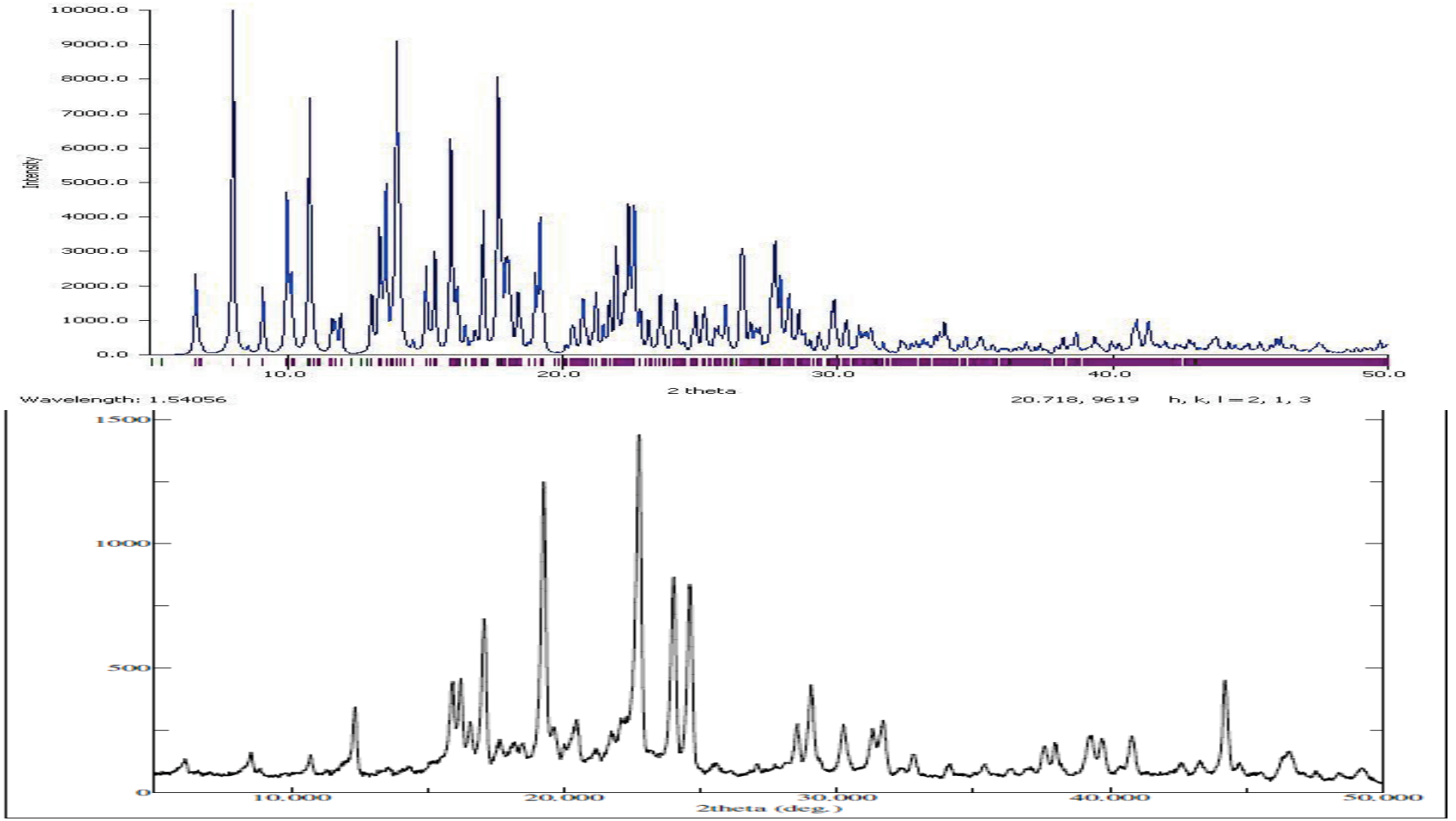

Figure 5-27: Simulated (top) and actual (bottom) PXRD of [4].

Figure 5-27 shows the simulated and actual PXRD of [4]. When the material is dried it is suggested that de-solvation of DMF occurs and changes the phase of the material. As the actual PXRD is compared to the simulated there are slight similarities and it is confirmed a phase change does occur due to the drying process. Material [4] was dried under vacuum and the PXRD is noticeably more readable, resulting in more DMF evaporating during the drying process.

Elemental maps were taken of [4] to verify elements, and determine where the elements were in the sample. In Figure 5-28, it is important to note that the intensities of the dots are of importance, not the number of dots in the image. Figure 5-28(a) demonstrates each element and that the sample contains the elements suspected. The elements in the material and color coordinated to those elements are as follows, magnesium (blue), sulfur (red), carbon (yellow), nitrogen (green), and oxygen (light blue). When separating the elements, trends in the images are noted. Figure 5-28(b), shows only magnesium and sulfur, and there is a high intensity of many dots of both elements. Parts of the image overlap, which results in a purplish color selection of dots. Magnesium and sulfur dots form an outline of the actual image, Figure 5-28(f).

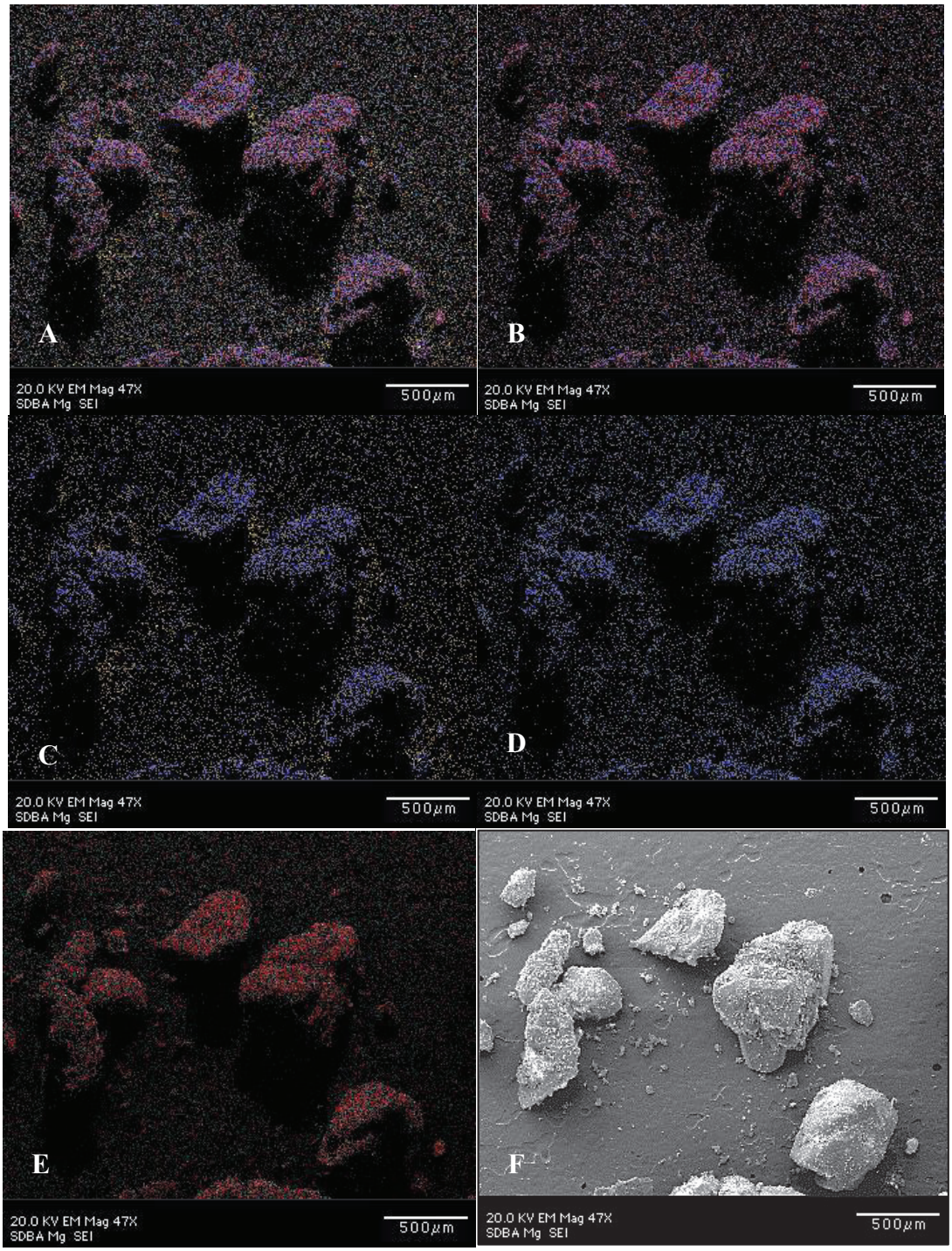

Figure 5-28: Elemental mapping images of [4].

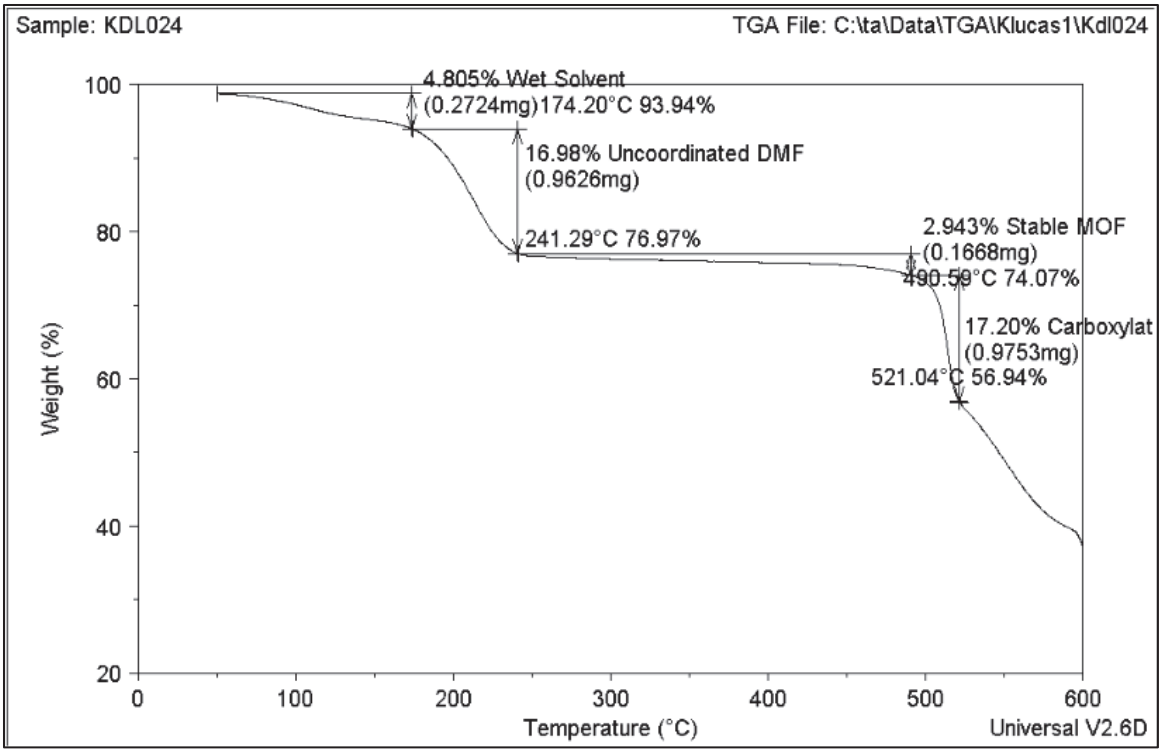

Figure 5-29: TGA of [4].

In Figure 5-29 the TGA shows that there is decomposition of wet solvent and uncoordinated DMF molecules from room temperature to 241.29°C. There is a stable MOF from ~242°C to 490.59°C with little to no decomposition. It is suggested that the carboxylates decompose around 521.04°C. The stability of the structure confirmed by the TGA show that MOF [4] is the most stable when heated to high temperatures, however, if scaled up could be harmful to the environment due to the volatility of the solvent.

5.2.5 [SDBA][Bipy]byproduct from [1]

[5] was synthesized from magnesium nitrate hexahydrate [$Mg(NO_3)_2 \cdot 6H_2O$], 4,4'-sulfonyldibenzoic acid (SDBA), and 4,4'-bipyridine (bipy) as seen in Scheme 5-6:

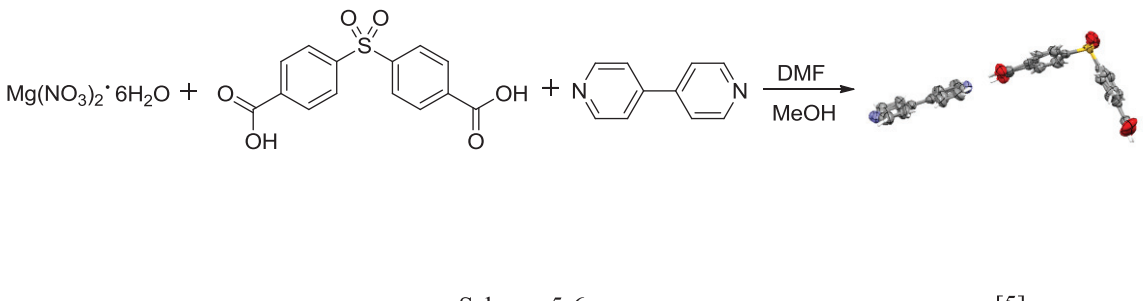

Scheme 5-6 [5]

Once there was confirmation of replication of product [1], the amount of product produced in each reaction was increased. By using a 200 mL autoclave the amounts of each reactant were increased from a 1 to 8.5 ratio equivalent. Due to the low ratio of magnesium hexahydrate in the reaction process, the metal cation did not take place in the final structure. However a pure organic compound was obtained. The mixture was stirred until all reactants are dissolved and the reaction was placed in an oven overnight. The structure and properties of the single crystal are intriguing with multiple phase changes and π-π stacking throughout the extended structure. The single crystal data was obtained and the molecular structure is shown in Figure 5-30.

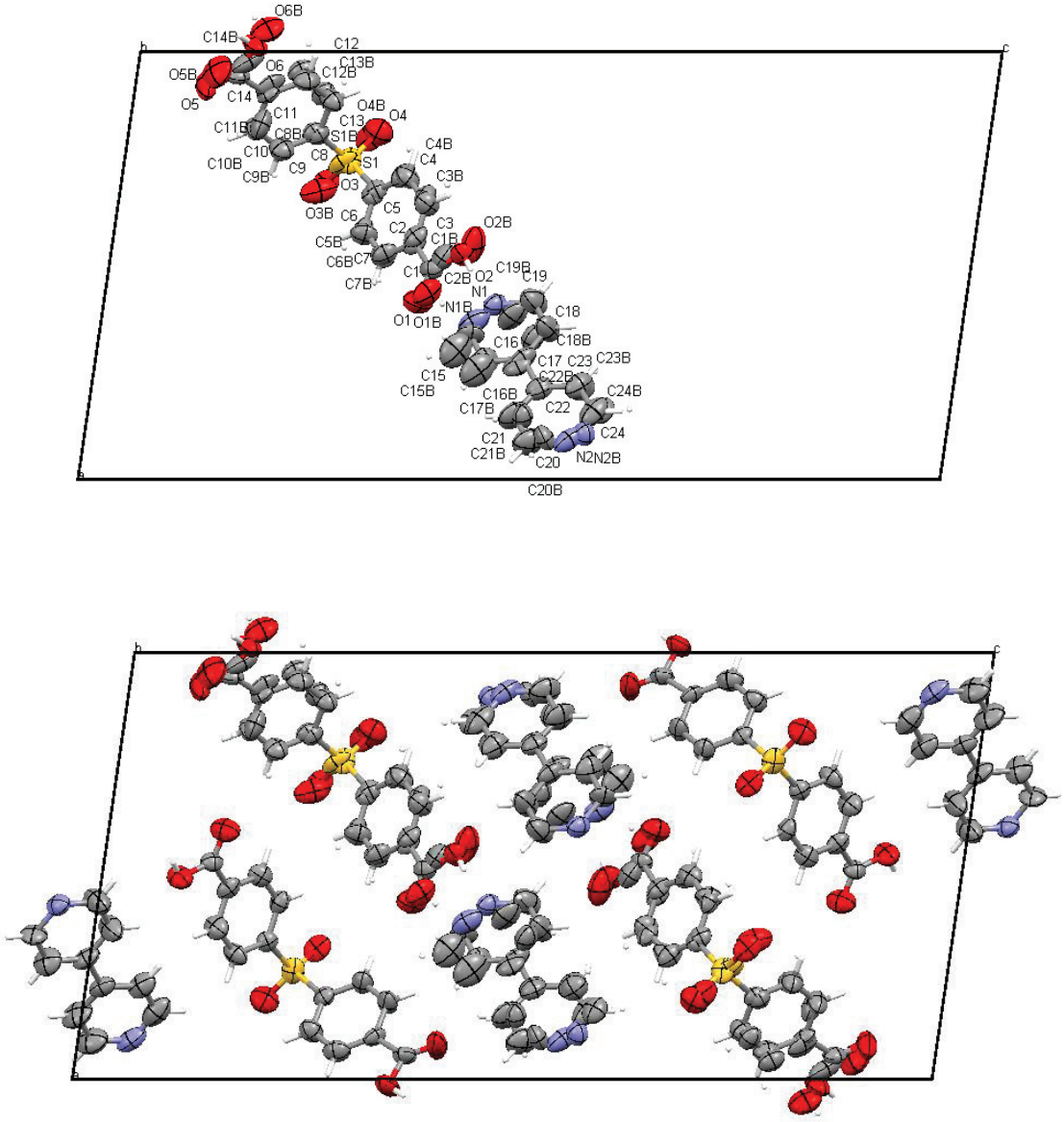

Figure 5-30: Molecular structure of [5] (top) and packed structure (bottom) with a view down the *b*-axis and thermal ellipsoids at 50%. Elements: carbon (gray), oxygen (red), sulfur (yellow), nitrogen (blue), and hydrogen (white).

The reaction yielded lightly tinted, pinkish fragmented crystals and lots of brown solvent. The solvent then became of interest and was put into a beaker and set in a fume hood for 1-2 weeks. Light brown needle-like crystals formed and dried in room

temperature air. The light brown needle-like crystals were the byproduct of the reaction. It is suggested that an insufficient amount of the magnesium salt was put into the reaction and the MOF did not completely form.

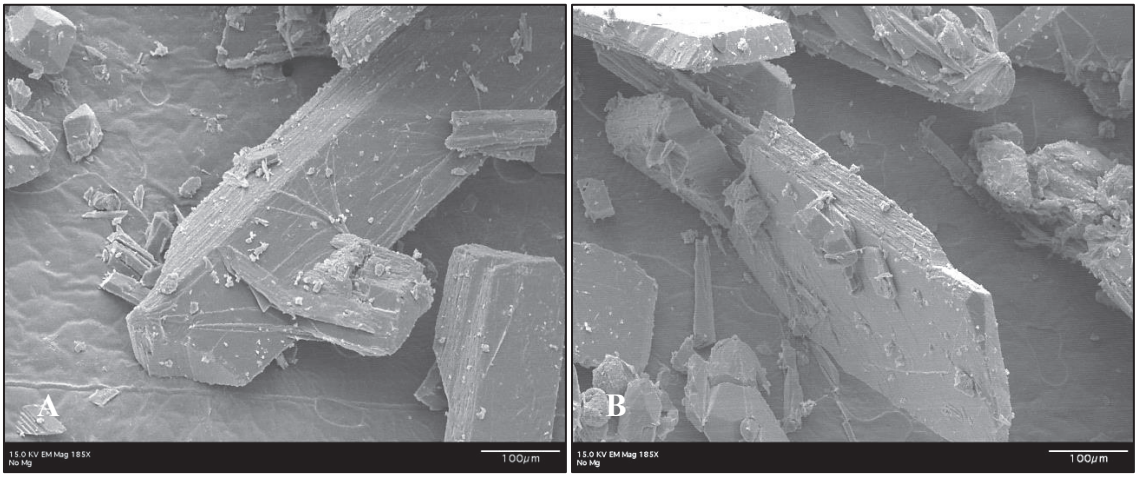

Figure 5-31: SEM images of [5] at 185X magnification.

Figure 5-31(a) shows the crystal placed on the carbon tape, whereas Figure 5-31(b) is of another crystal standing on its side. It is noted in Figure 5-31(a) and (b) there are different morphologies of crystal within the material. There are small fragmented crystals or possible particles of different shapes and sizes and then there are rectangular blocked shaped crystals.

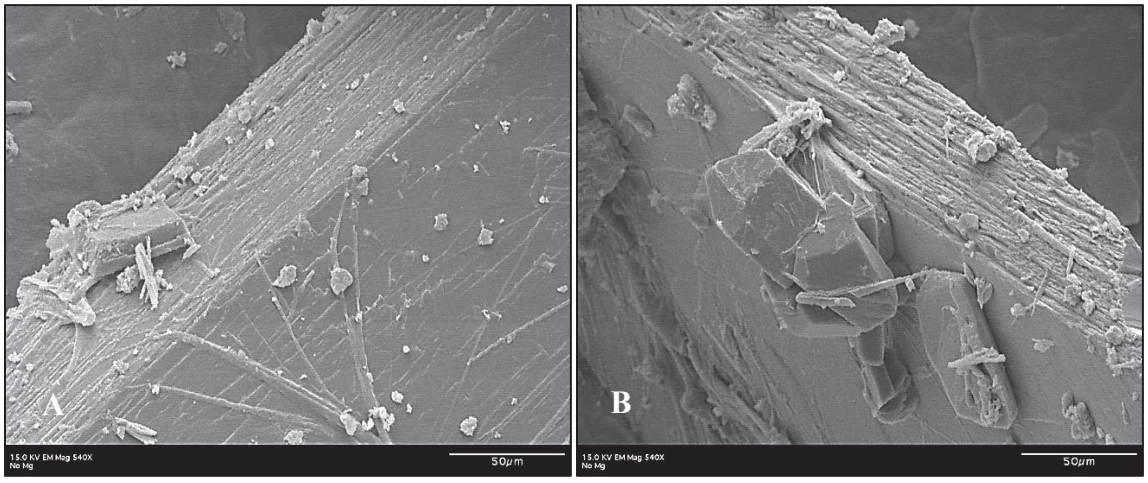

Figure 5-32: SEM images of [5] material at 540X magnification.

Figure 5-32, shows images taken at slightly higher magnification to visualize the morphology in the crystal. In Figure 5-33(b) the morphology of the material demonstrates texture. Figure 5-33 shows magnified images of 1860X their original size. Both images give excellent definition and conformation that the rectangular block crystals are formed. With the small fragments magnified, it is possible that there are different phases of the material.

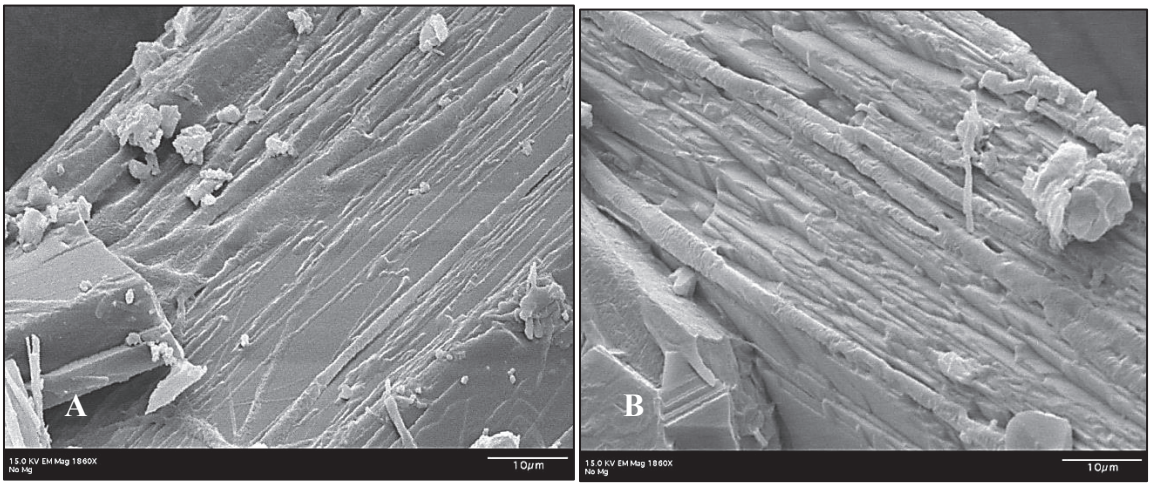

Figure 5-33: SEM images of [5] at 1860X magnification.

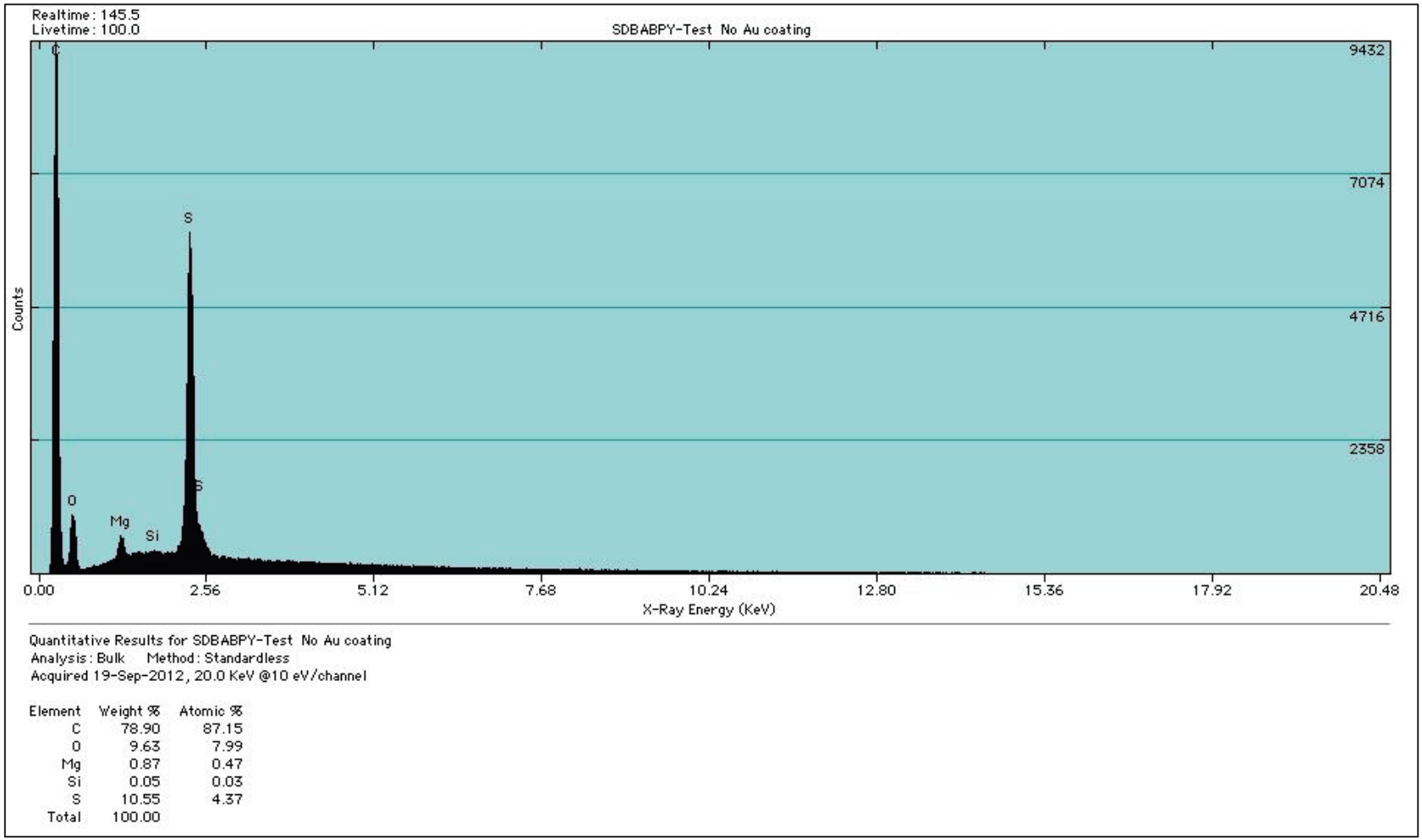

Figure 5-34: EDS Spectra of [5].

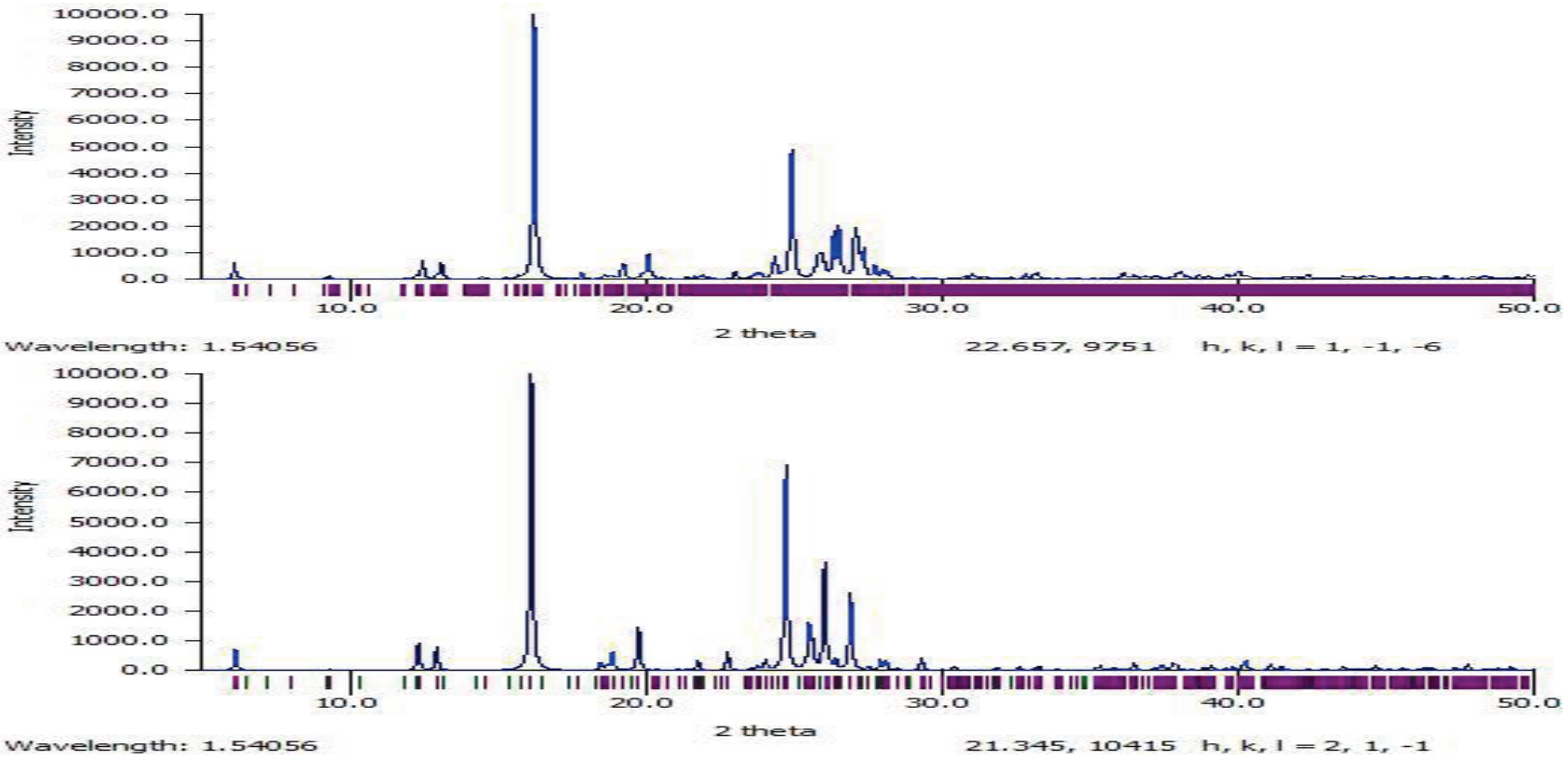

Figure 5-35: Simulated PXRDs of [5] at two different phases.

5.2.6 Ball Mill Product [7]

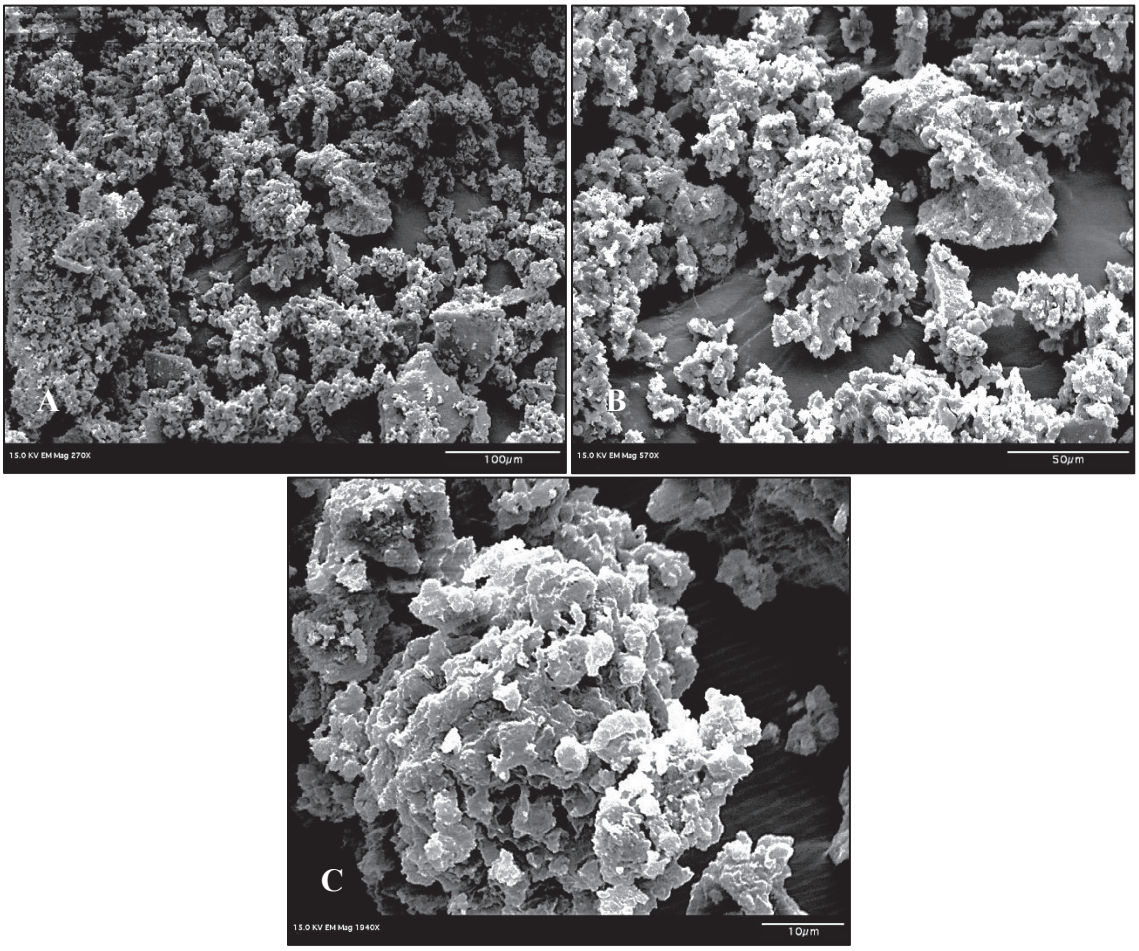

Figure 5-36: SEM images of [6] at different magnifications, 270X, 570X, and 1940X, respectively.

Figure 5-36 demonstrates the different morphologies obtained from a mechanochemical process. It is unknown how the materials are formed together, and further characterization is needed.

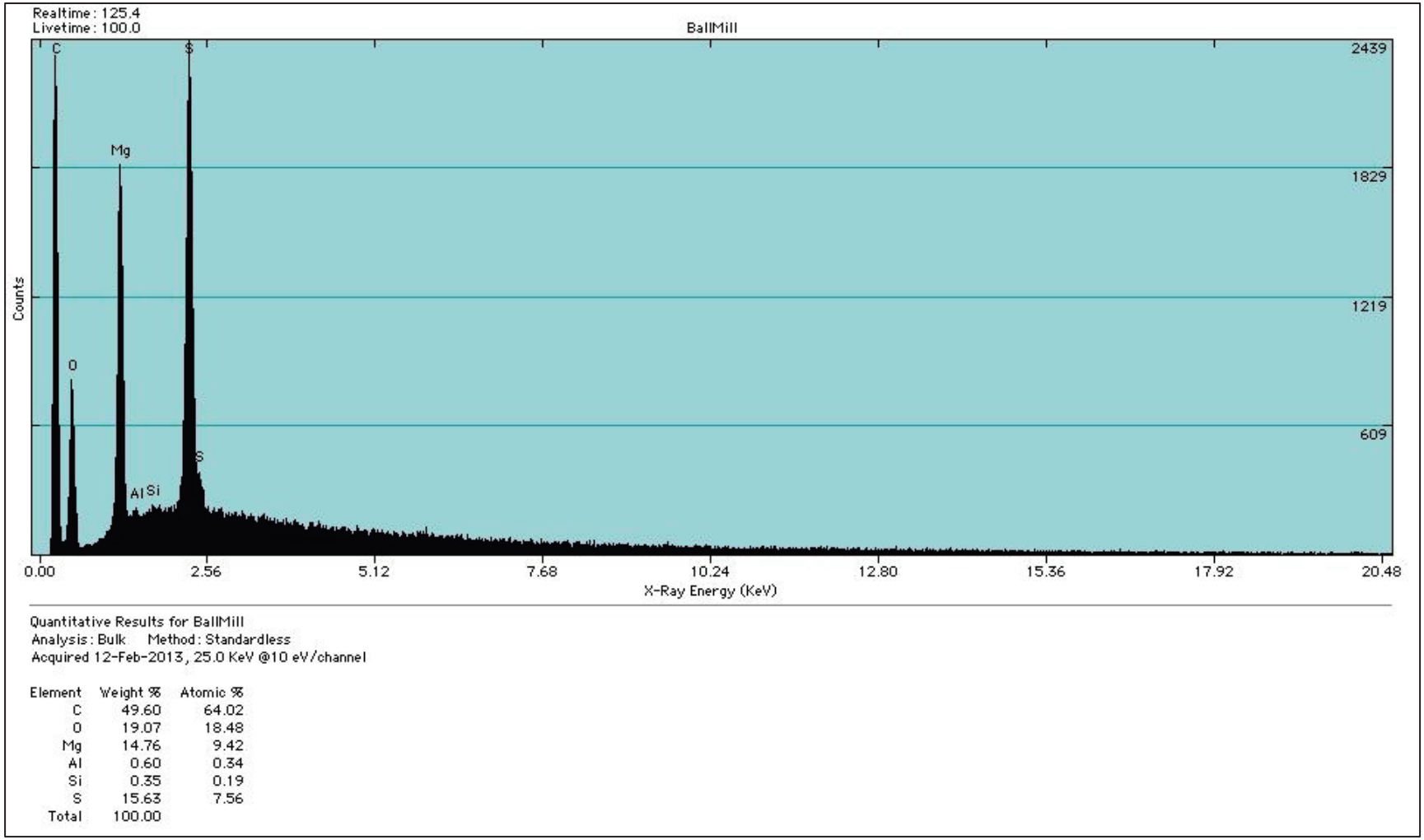

Figure 5-37: EDS spectrum of Ball Mill Product, [6].

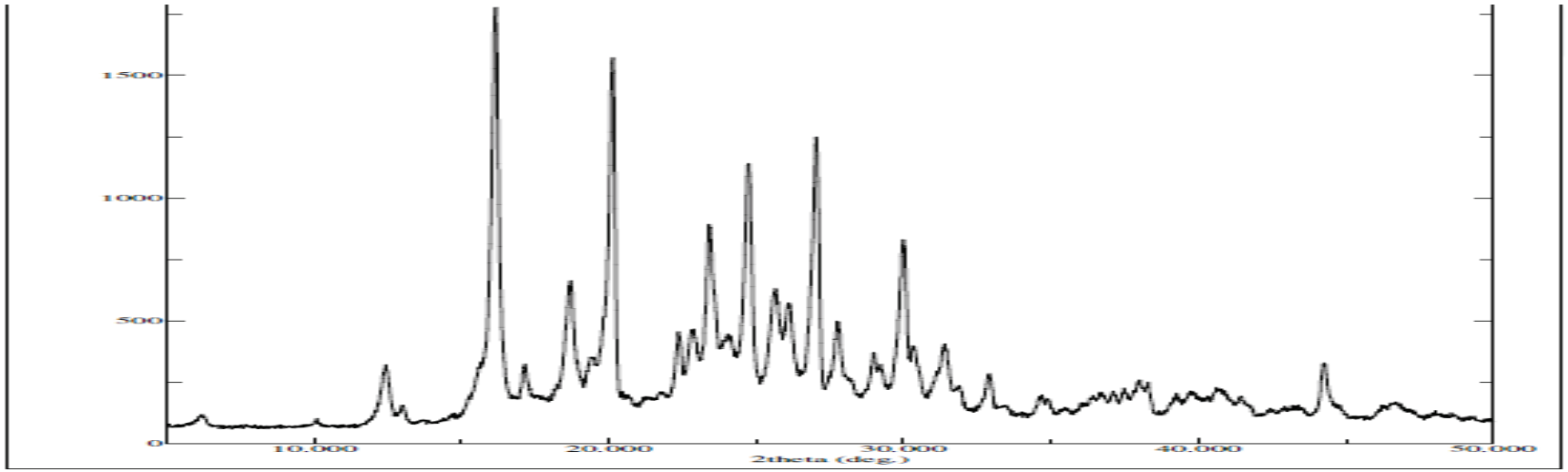

Figure 5-38: Actual PXRD of Ball Mill Product, [6].

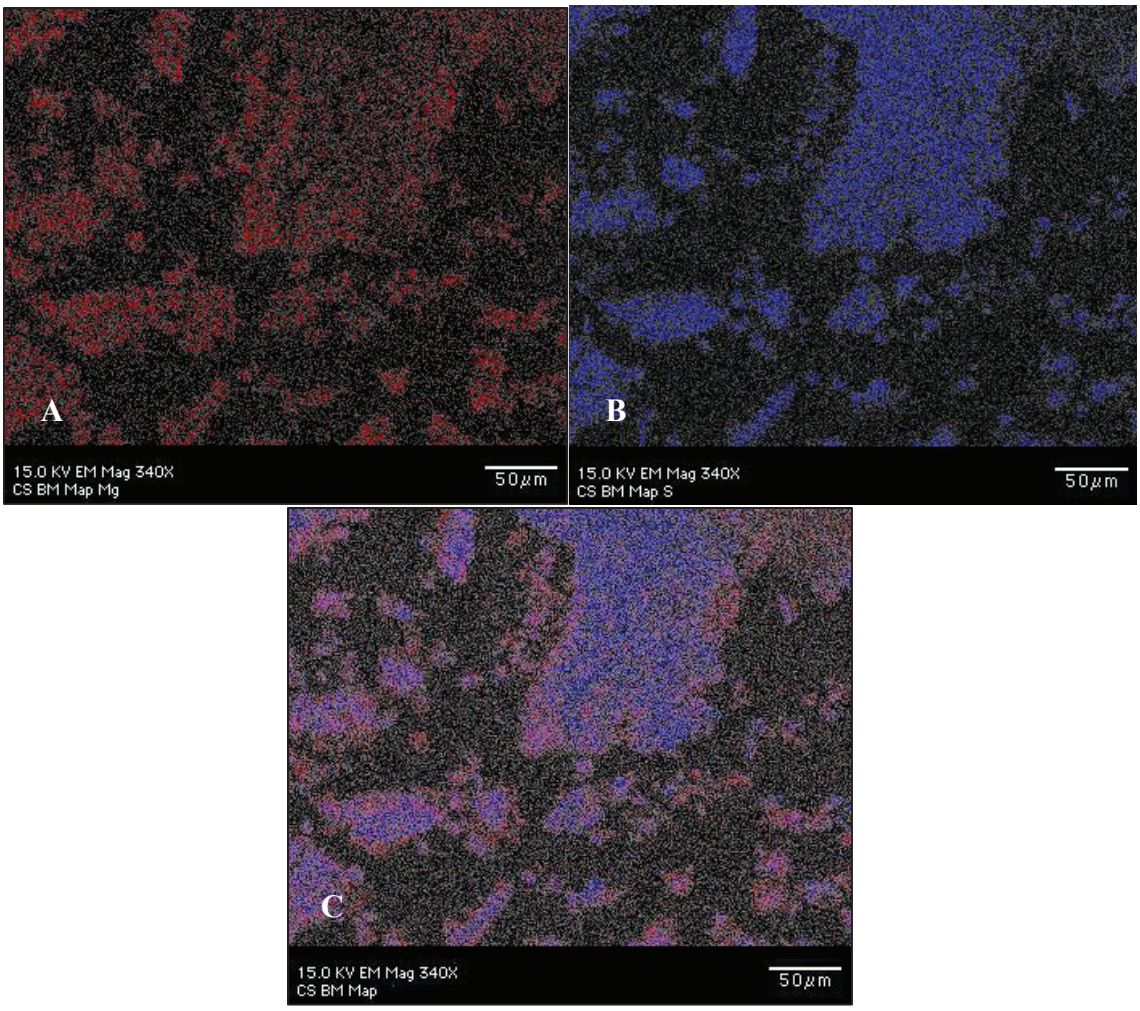

Figure 5-39: Elemental maps of the cross section of Ball Milled Product [6]. The magnesium, red, encompasses the sulfur, blue, which can be seen in image (c).

Elemental maps were completed on a cross section from one of the crystalline materials. In the maps, it is suggested that the SDBA and $Mg(NO_3)_2 \cdot 6H_2O$ were fused together because of the heat that occurred during the reaction. The intensities of the dots are all the same throughout the maps, which show that the elements are evenly distributed throughout the material.

A TGA with temperatures ranging from 15.4°C to 500°C was taken, on the ball mill product, [6]. Figure 5-40 shows that there is no stability in the material, and as it is

heated it steadily decomposes. For SDBA and magnesium metal, mechanochemical synthesis is not the route to attempt when trying to form a stable MOF.

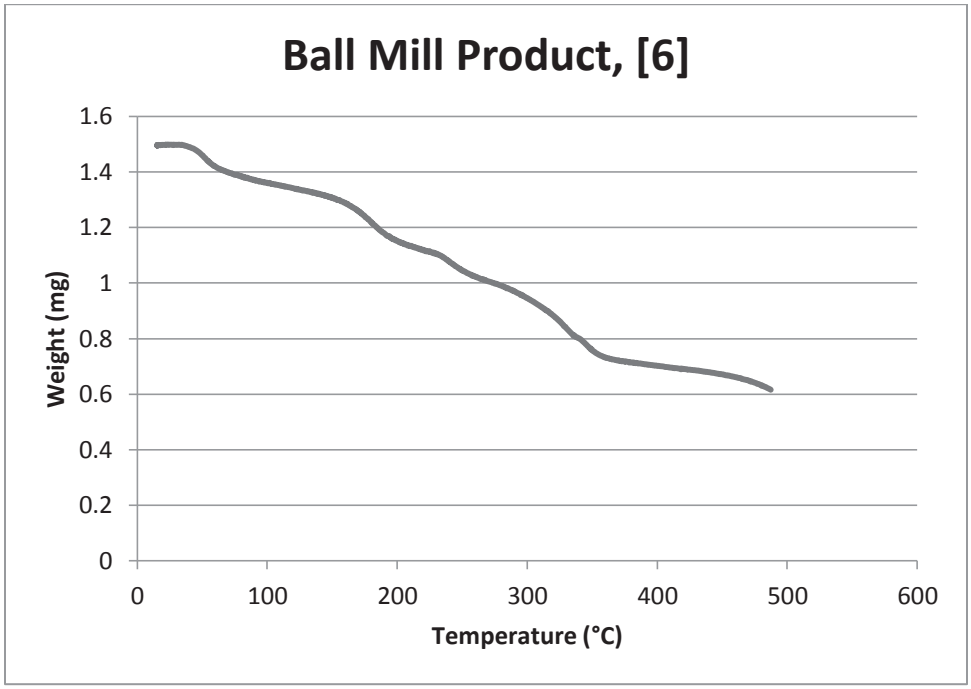

Figure 5-40: TGA of [6].

5.2.7 Alumina Pellet Support

Characterizations are better achieved if the MOF is grown on a support, which could be gold, aluminium, etc. There are different types of methods for growing MOFs on supports, i.e. nucleation, evaporation. For the materials produced in this project, a seeding method was utilized. HKUST-1 was added to an alumina support through reactive seeding and was successful in growing HKUST-1 on the support.[37] The reaction was attempted with one product, [1], and an Al_2O_3 pellet.

To notice a change in the alumina pellet before and after the reaction took place SEM images were taken and can be seen in Figure 5-41 and Figure 5-42. It is noted that from the visible eye, MOF crystals formed on the front and back of the alumina pellet. Figure 5-41(a) shows the image of the alumina pellet before the reaction at 100X and

then Figure 5-41(b) is after the reaction at 50X. There is a difference in the two alumina pellet images. The alumina pellet before the reaction appears uniform all the way across Figure 5-42(a), however after the reaction there are darker areas along the pellet, Figure 5-42(b), which do not have a smooth surface.

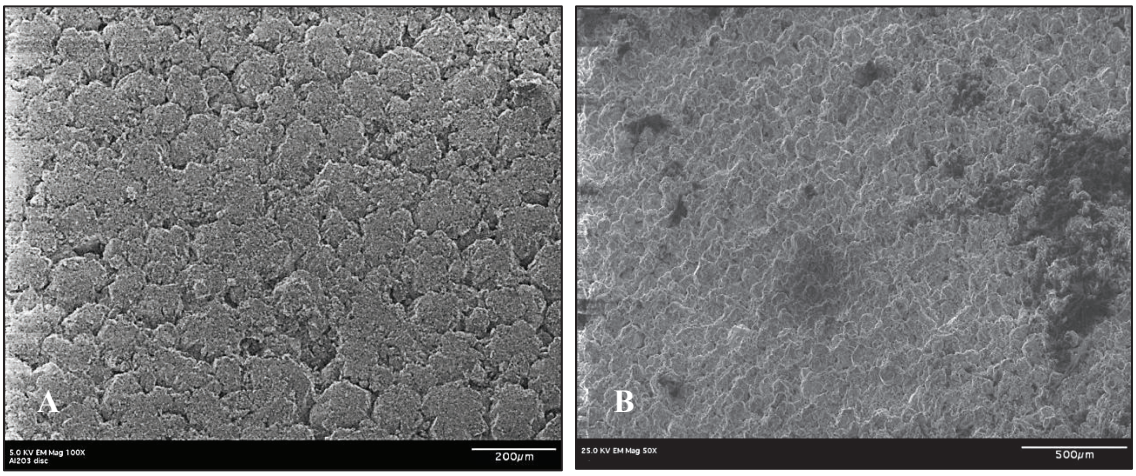

Figure 5-41: Alumina pellet before and after the reaction with [1].
Image A is 100X and Image B is 50X.

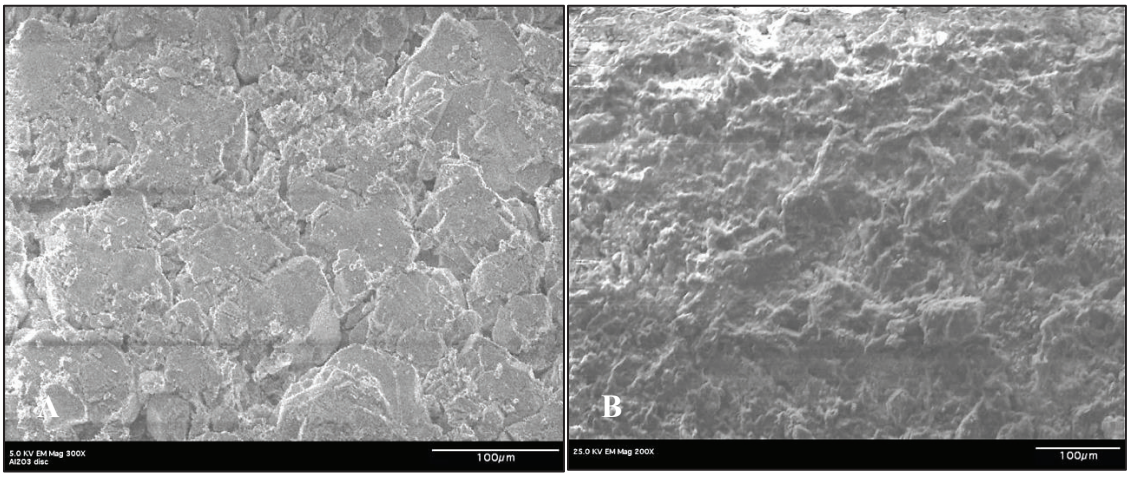

Figure 5-42: Alumina pellet before (a) and after the reaction (b).

In Figure 5-42 there is an obvious change in the morphology of the alumina pellet after the reaction occurs. There are visible differences between the before and after treatment of the alumina pellet, which suggest that a reaction took place and a product formed on the alumina support. It appears as if the pellet is shaped from multiple platelets

or plateaus that formed together. In Figure 5-42(b), it is noted that the platelets of the alumina pellet have crystalline fragments growing off of them.

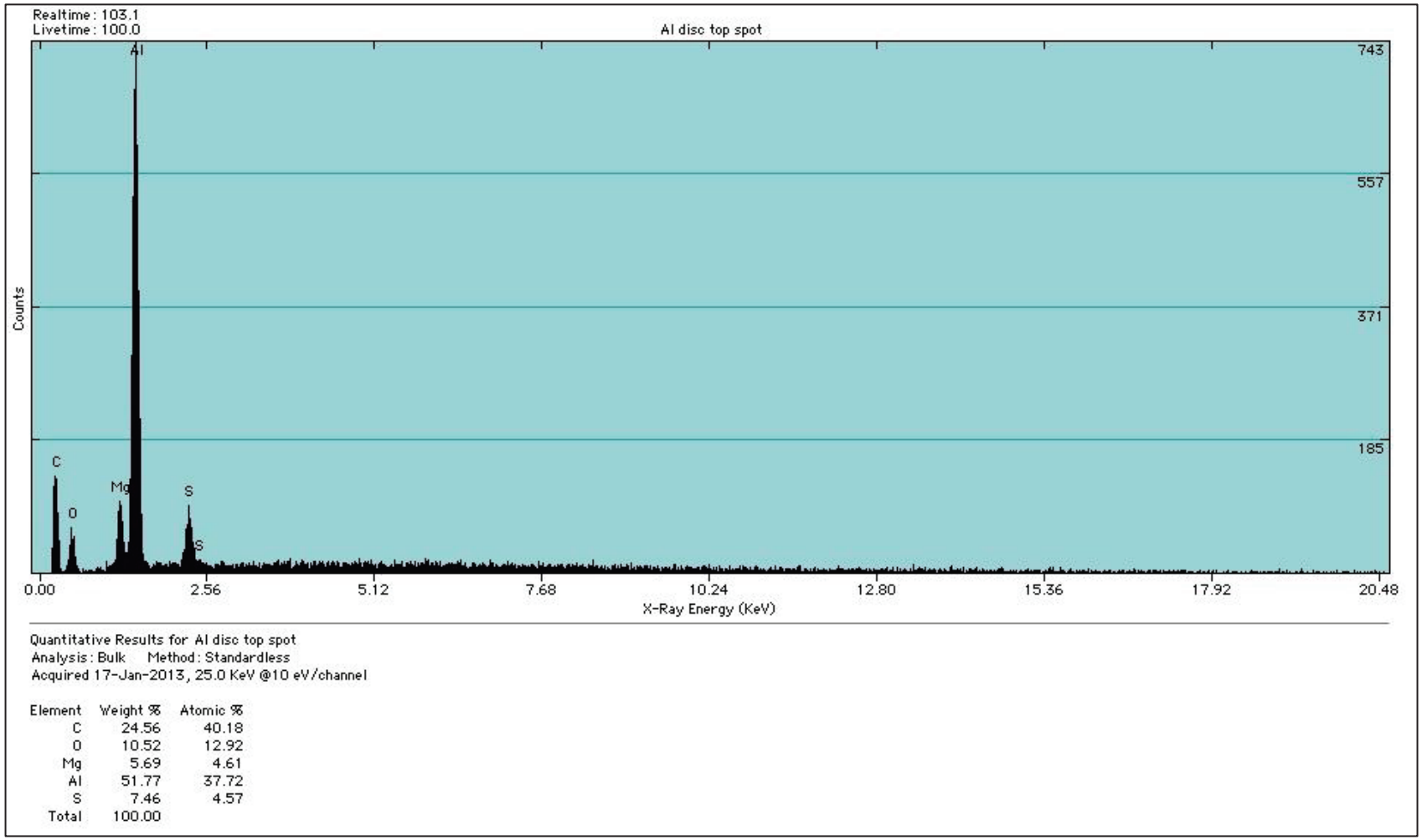

Figure 5-43: EDS spectra of [1] onto Al_2O_3 Pellet.

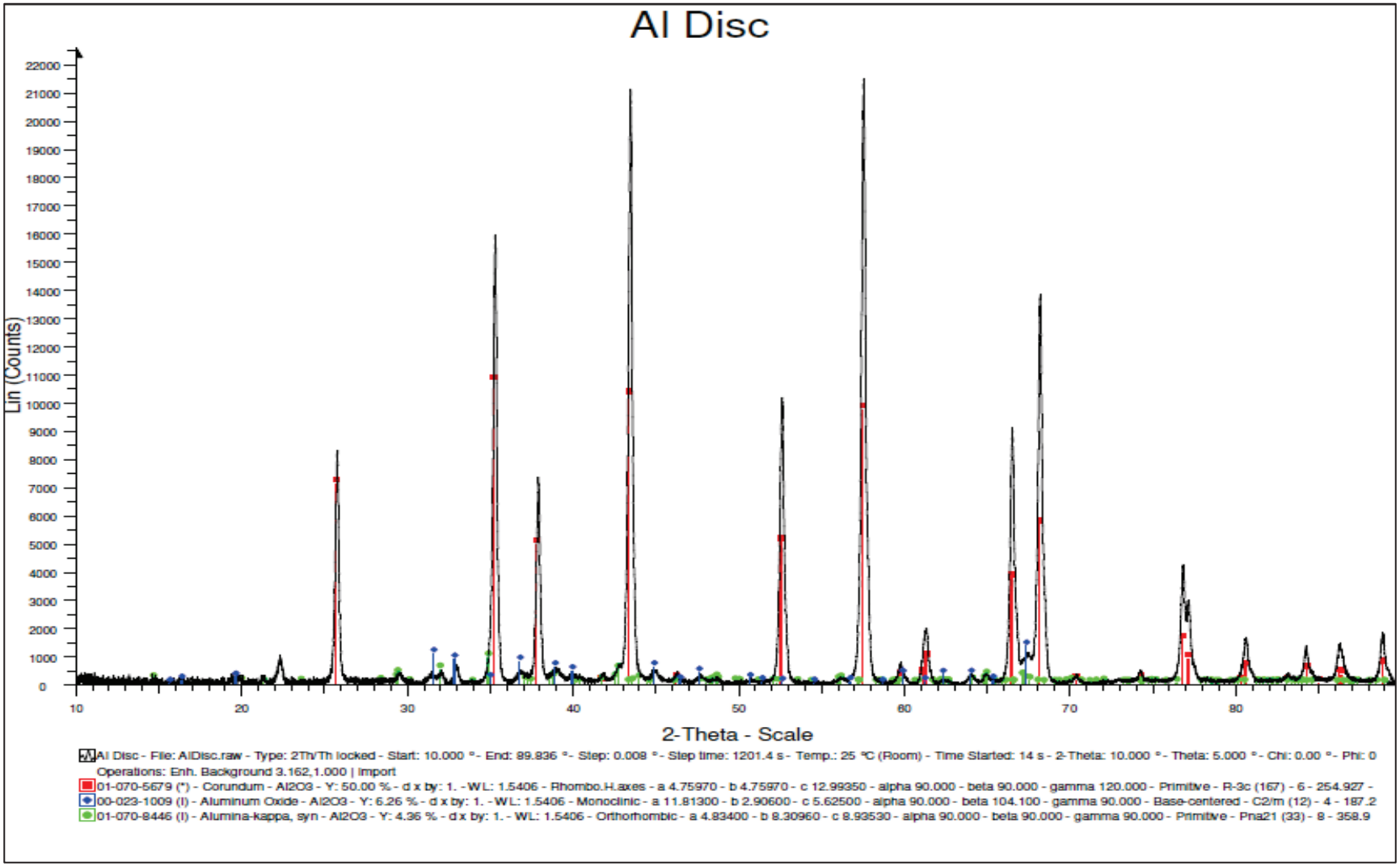

Figure 5-44: PXRD of Alumina Pellet. Note that there are multiple phases of the alumina, however no MOF can be seen in the PXRD.

In Figure 5-43, an EDS spectra of the alumina pellet is shown. Notice that there is substantial evidence that the MOF reactants are located within the pellets surface. However, a PXRD shows that there are no peaks of the MOF or any of its starting material. It is suggested that the DMF de-solvated and cause the possible MOF crystals to become non-crystalline. Once the PXRD was taken, the MOF crystals did not diffract and could be a reason why they did not show on the PXRD, Figure 5-44.

Figure 5-45 shows the elemental maps that were taken of the alumina pellet to confirm that there is MOF material on its' surface. When completing the elemental mapping of the reacted alumina pellet, the area of interest was the edge of the pellet. In the SEM image below (black and white), the edge of the pellet seemed like it was charging more than the surface, and had a rough morphology. The charging might be from organic components in the alumina, in particular the MOF. Once a map was taken on the edge it was noted that there were other elements than the aluminium and oxygen, including carbon, sulfur, and magnesium. The maps revealed that the elements seem to coagulate in one spot and then disperse throughout the pellet, as seen in the bottom image.

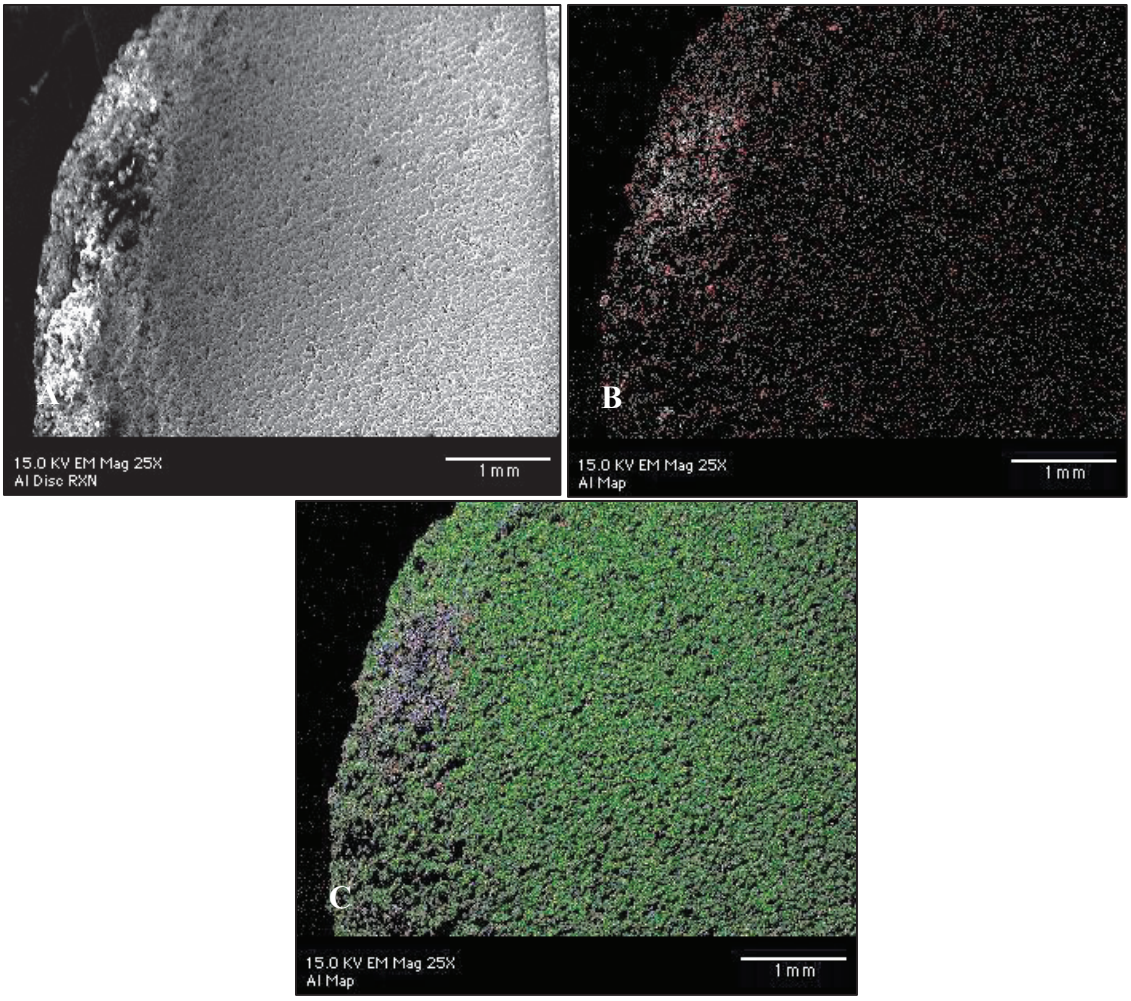

Figure 5-45: Elemental Maps of [1] on alumina support. Elements mapped consist of magnesium (red), sulfur (blue), oxygen (yellow), aluminum (green), and nitrogen (white).

Chapter 6: Discussion and Conclusion

6.1 Metal-Organic Frameworks

The results provided by the microscopic and crystal diffraction data offer solid support for the three metal-organic frameworks produced. The SEM images and EDS spectra suggest the porosity and purity of these simple solvothermal synthetic products. The pores and channels that the SEI show of the products provide ample support that it is possible for the three dimensional frameworks to adsorb some type of common gas. Furthermore, the depth of the pores and the number of spaces within the frameworks might result in good adsorption or surface areas. The interpenetration that is sometimes said to harm the product, actually aids in the stability of the product in these cases.[4] The EDS spectrum show in detail trace amounts of impurities that are in the sample after the reaction. It is noted that the impurities may be due to the magnesium salt that was used as starting material. Otherwise, the EDS give solid data that the MOFs contain the reactants that were used for the reaction.

The disadvantages of the syntheses with [1] through [4] are 1) the DMF that precipitates out of the material during the drying process. The DMF makes it difficult for powder XRD characterizations, limiting the diffraction on the actual product because of the amount of DMF that is ground within the material. Unfortunately, how to remove the DMF solvent and still produce the same product is unresolved. 2) The solvent itself is a disadvantage because of its volatility; the MOF will never be able to be produced commercially. It would be harmful to workers in the industry if the chemicals were scaled to industrial size.

The high quality crystal data gives much information on the weight, size, dimensions of the structure, etc. It is noted that MOF material is difficult to crystallize, and when single crystals occurred good data were attained. The disorder in most of the structures shows flexibility in the structure. Even under high and low temperatures the structure will adjust to keep itself stable, which can result in good characteristics for adsorbing gases at different temperatures and pressures.

6.2 [SDBA][Bipy] [5] and Ball Milled Product [6]

The by-product, [SDBA][Bipy], stemmed a novel crystalline product. The structure has multiple phase changes when heated or cooled, and was an unexpected result. It is noted that if there is not enough magnesium nitrate in the reaction then the reaction will not fully take place but form a phase of the by-product. SDBA is a difficult compound to crystallize, but when 4,4'-bipyridine and DMF are added into the reaction mixture, SDBA will crystallize with bipy by evaporation.

The ball milled product, [6], was not successful in producing a MOF. The reactants used did not work well in the ball mill because they need high pressures and temperatures for the reaction to fully take place. When DMF solvent was placed into the reaction mixture, the results were not able to be characterized because of the state of the material. The product was a mixture of agglomerates of the different starting materials and had no stability when heated. It is not suggested to continue ball mill reactions with SDBA as an organic linker. It is advised to use a nitrogen-based organic linker because they are more reactive when heat is applied and would bond to the metal cation more easily.

6.3 Alumina Support

The reaction of [1] on the alumina disc was successful, however was limited by the amount of crystal MOF that formed on the disc. The characterizations supported the accusations that the reaction did take place and the MOF is on the alumina support. The elemental maps suggest that there is MOF crystal formation on the disc by showing magnesium, sulfur, carbon, etc. in absence of aluminum. The SEM images reveal that the disc has a different morphology before and after the reaction. When comparing the support to HKUST-1 support similarities and differences are noticed, Figure 6-1.

Although the alumina support was successful, the amount of crystal that actually formed on the surface is unknown, but from the visible eye, it is not enough for the disc to be put into any application. The next step would be to see if there was a better way to get more crystallization on the alumina disc.

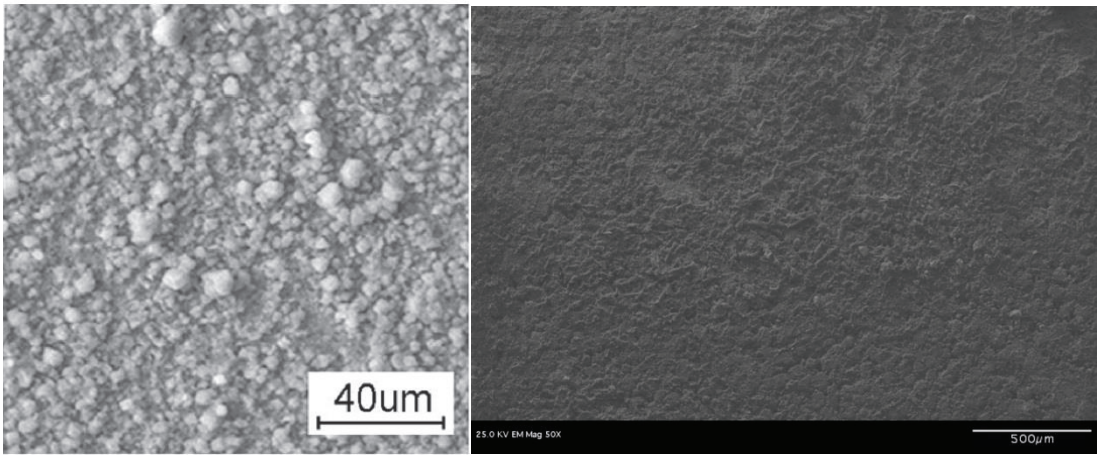

Figure 6-1: Left image is of HKUST-1 support from Nan et al.[26] and right image is the alumina support at 50X.

To produce the alumina disc a pellet press was used and the disc was put under a maximum of 2000 psi, which gave a very "soft" pellet that is able to fall apart easily. To make a more stable disc, it would be necessary to have a higher psi of 160X more the

applied pressure. It is necessary to be aware of the pores that are formed in the disc when high pressure is applied. The pore size has a large impact on the reaction because the MOF will form in the pores of the disc.

6.4 Conclusion

Overall the goal to produce novel three-dimensional MOFs and characterize them was successful. Four three-dimensional MOFs were produced and characterized along with two other novel products. Throughout the project there were many trial and errors to find the correct synthesis which produced the best results. To achieve good data it was necessary to have single crystal formation in the product. Five of the reactions resulted in single crystal, most were powder samples, which could not be fully characterized.

Once crystalline products were produced and their crystal structures determined, SEM images were taken to verify that the structures contained voids. To have good adsorption properties, ample sized pores and large surface areas are necessary. EDS spectra were also taken on the products to prove that the materials contained trace amounts of impurities and that all the reactants were in the products. All of the materials produced did verify those requirements.

TGA and DSCs data were gathered to show if any materials had stability when heated. Material [4] demonstrated that it was stable from 250-500°C, however none of the other materials had better stability. Mostly the products showed decomposition in the TGA and DSC when heated, however all materials had stability at room temperature. The PXRDs that were taken had broad peaks making the footprint of the material difficult to interpret. Future work would be achieving quality PXRD data by preventing the DMF to precipitate during the drying process.

In conclusion, three-dimensional MOFs, [1] through [4], a by-product [SDBA][Bipy], and a ball mill product [6] were produced. MOF [1] was successfully placed onto an Al_2O_3 pellet. Elemental mapping suggested the MOF formed on the side of the pellet. It was determined that the ball mill product was not able to be characterized in detail and better reactants are needed to produce a MOF with a mechanochemical reaction. The SEM images were successful in showing the morphology and topology of the crystalline structures. While more research is necessary to determine the gas adsorption properties and BET surface areas of the MOFs, the microstructural characteristics show successful data in producing novel materials.

6.5 Future Work

Currently, there are many areas that MOFs are used for in the industry other than gas adsorption which involve, sensory MOFs, catalysis, drug delivery, etc. It would be beneficial to take a MOF that is produced and use it for catalysis. The frameworks of the MOF can be tailored by adjusting the linkers, which will alter the porosity. Utilizing different organic linkers that includes chirality has an important role in working with MOFs. The chirality of the linkers can react differently to cations when working with catalysis.

Starting with an MOF that has coordinately unsaturated metal sites (CUSs), Chang and Férey *et al.* presents a new method for selective coordination of electron-rich functional groups to chromium (III) for example, in MIL-101.[12] MIL-101 had the water molecules removed by vacuum, which left a dehydrated porous structure, and by adding an electron-rich functional group, ethylenediamine, the structure was then filled and can be used in further reactions. Also, different cations can be added into a MOF that has

porous unsaturated metal sites. By taking out reacted cations, i.e. Cu^{2+} or Zn^{1+}, then adding Li^{1+} or another reactive cation, more reactions can be completed with the MOF and the research can go further. The new cation might be able to help stabilize the MOF or give it better adsorption properties.

Other future work can be producing different mesoporous materials. By adding more organic or more inorganic reactants diverse materials can be produced. The materials formed might not need a metal cation to be stable and interpenetration might be what is keeping the material from collapsing. Without a metal cation the mesoporous material could have better reactivity when adsorbing host molecules because of the electronegativity of the structure.[4] If the structure contains inorganic materials, it is possible that the crystal structure could be simulated on a computer before the reaction takes place. That will help determine the outcome of the experiment and decrease trial and error experiments, along with systematic chemistry.

Chapter 7: References

1. Apple Inc. (**2013**, April 8). Apple and the Environment. Retrieved from Apple: http://www.apple.com/environment/our-footprint/.
2. Exelon Corp. (**2013**, April 8). Exelon Corporation 2011 Sustainability Report. Retrieved from Exelon: http://www.exeloncorp.com/assets/newsroom/downloads/docs/dwnld_Exelon_CSR.pdf.
3. Bao, Z.; Yu, L.; Ren, Q.; Lu, X.; Deng, S. *Journal of Colloid and Interface Science* "Adsorption of CO_2 and CH_4 on a magnesium-based metal organic framework." **2011**, 353, 549–556.
4. Editor: Farrusseng, D. Contributors: Aguado, S.; Alaerts, L.; Allendorf, M.D.; Barea, E.; Bauer, C.A.; Bétard, A.; Böhringer, B.; Canivet, J.; Coudert, F.-X.; Czaja, A.; Dailly, A.; Delle Rocca, J.; Denayer, J.F.M.; De Vos, D.; Fischer, R.; Fischer, R.A.; Horcajada, P.; Horike, S.; Kaskei, S.; Kitagawa, S.; Küsgens, P.; Leflaive, P.; Leung, E.; Lin, W.; Llewellyn, P.L.; Lohe, M.R.; Martens, J.A.; McKinlay, A.C.; Morris, R.E.; Müller, U.; Perry IV, J.J.; Pirngruber, G.D.; Quadrelli, A.; Rodriquez Navarro, J.A.; Rose, M.; Serre, C.; Trukhan, N.; Turra, F.; Wee, L.H. *Metal-Organic Frameworks: Applications from Catalysis to Gas Storage* **2011**. Weinheim, Germany: Wiley-VCH Verlag & Co., KGaA, Boschstr.
5. Baker, R.W. and Lokhandwala, K. *Ind. Eng. Chem. Res.* "Natural Gas Processing with Membranes: An Overview." **2008**, 47, 2109-2121.
6. Cavenati, S.; Grande, C.A.; Rodrigues, A.E. *Ind. Eng. Chem. Res*. "Metal Organic Framework Adsorbent for Biogas Upgrading." **2008**, 47, 6333–6335.
7. Koch, W.R.; Kumar, R.; Sircar, S.; Vansloun, J.K. (March 8, **1989**) Google Patents: Recovery of methane from land fill gas. Retrieved from: IFI CLAIMS: http://www.google.com/patents/EP0305919A1?cl=en.
8. Samanta, A.; Zhao, A.; Shimizu, G.K.H.; Sarkar, P.; Gupta, R. *Ind. Eng. Chem. Res.* "Post-Combustion CO2 Capture Using Solid Sorbents: A Review." **2012**, 51, 1438–1463.
9. Palomino, M.; Corma, A.; Rey, F.; Valencia, S. *Langmuir* "New Insights on CO2-Methane Separation Using LTA Zeolites with Different Si/Al Ratios and a First Comparison with MOFs." **2010**, 26(3), 1910–1917.
10. Yamamoto, K. and Tatsumi, T. *Chem. Mater*. "ZOL: A New Type of Organic–Inorganic Hybrid Zeolites Containing Organic Framework." **2008**, 20, 972–980.
11. Peralta, D.; Chaplais, G.; Simon-Masseron, A.; Barthelet, K.; Chizallet, C.; Quoineaud, A.-A.; Pirngruber, G.D. *J. Am. Chem. Soc.* "Comparison of the Behavior of Metal−Organic Frameworks and Zeolites for Hydrocarbon Separations." **2012**, 134, 8115−8126.

12. Fang, Q.-R.; Makal, T.A.; Young, M.D.; Zhou, H.-C. *Comments on Inorganic Chemistry* "Recent Advances in the study of Mesoporous Metal-Organic Frameworks." **2010** 31, 165-195.
13. Melo, R.A.A.; Giotto, M.V.; Rocha, J.; Urquieta-González, E.A. *Materials Research* "MCM-41 ordered mesoporous molecular sieves synthesis and characterization." **1999** 2(3), 173-179. Retrieved April 08, 2013, from http://www.scielo.br/scielo.php?script=sci_arttext&pid=S1516-14391999000300010&lng=en&tlng=en. 10.1590/S1516-14391999000300010.
14. Yaghi, O.M.; Li, H.; Davis, C.; Richardson, D.; Groy, T.L. *Acc. Chem. Res.* "Synthetic Strategies, Patterns, and Emerging Properties in the Chemistry of Modular Porous Solids." **1998**, 31, 474-484.
15. Eddaoudi, M.; Moler, D.B.; Li, H.; Chen, B.; Reineke, T.M.; O'Keeffe, M.; Yaghi, O.M. *Acc. Chem. Res*. "Modular Chemistry: Secondary Building Units as a Basis for the Design of Highly Porous and Robust Metal-Organic Carboxylate Frameworks." **2001**, 34, 319-330.
16. Editor: Schröder, M. Contributors: Banaerjee, M.; Champness, N.R.; Cooper, A.I.; Das, S.; Fischer, R.A.; Jiang, J.-X.; Kim, K.; Kitagawa, S.; Lin, W.; Ma, L.; Mugnaini, V.; Roques, N.; Schröder, F.; Schröder, M.; Uemure, T.; Veciana, J.; Yoon, M. **2010** *Functional Metal-Organic Frameworks: Gas Storage, Separation and Catalysis* Heidelberg, Germany: Springer.
17. Li, H.; Eddaoudi, M.; O'Keeffe, M.; Yaghi, O.M. *Nature* "Design and synthesis of an exceptionally stable and highly porous metal-organic framework." **1999**, 402, 276-279.
18. Furukawa, H; Ko, N.; Go, Y. B.; Aratani, N.; Choi, S. B.; Choi, E.; Yazaydin, A.O.; Snurr, R. Q.; O'Keeffe, M.; Kim, J.; Yaghi, O.M. *Science* "Ultrahigh Porosity in Metal-Organic Frameworks." **2010**, 329, 424-428.
19. Yaghi, O.M.; Davis, C.E.; Li, G.; Li, H. *J. Am. Chem. Soc.* "Selective Guest Binding by Tailored Channels in a 3-D Porous Zinc(II)-Benzenetricarboxylate Network." **1997**, 119, 2861-2868.
20. Reger, D.L.; Debreczeni, A.; Reinecke, B.; Rassolov, V.; Smith, M.D. *Inorg. Chem.* "Highly Organized Structures and Unusual Magnetic Properties of Paddlewheel Copper(II) Carboxylate Dimers Containing the π-π Stacking, 1,8-Naphthalimide Synthon." **2009**, 48, 8911-8924.
21. Burrows, A.D.; Frost, C.G.; Mahon, M.F.; Winsper, M.; Richardson, C.; Attifield, J.P.; Rodgers, J.A. *Dalton Transactions* "Subtle structure variation in copper metal-organic frameworks: synthesis, structure, magnetic properties, and catalytic behavior." **2008,** *47,* 6788-6795.
22. Qiu, W.; Perman, J.A.; Wojitas, L.; Eddaoudi, M.; Zaworotko, M.J. *Chem Comm* "Structural diversity through ligand flexibility: two novel metal-organic nets via ligand-to-ligand cross-linking of "paddlewheels." **2010**, 46, 8734-8736.

23. Chui, S.S.-Y.; Lo, S.M.-F.; Charmant, J.P.H.; Orpen, G.; Williams, I.D. *Science* "A Chemically Functionalizable Nanoporous Material [Cu3(TMA)2(H2O)3]n." **1999**, 283, 1148-1150.
24. Editor: MacGillivray, L.R. Contributors: Batten, S.R.; Champness, N.R.; Chun, H.; Collins, D.J.; Dubbeldam, D.; Dutta, S.; Eddaoudi, M.; Eubank, J.F.; Friščič, T.; Frost, H.; Fujita, M.; Georgiev, I.G.; Ghosh, S.K.; Hubberstey, P.; Kim, H.; Kim, K.; Kitagawa, S.; Lin, W.; Lin, X.; Ma, S.; Schröder, M.; Snurr, R.Q.; Yazaydin, O.A.; Wu, S.; Zhou, H.-C. **2010**. *Meta-Organic Frameworks: Design and Application*. Hoboken, NJ: John Wiley & Sons, Inc.
25. Bradshaw, D.; Garai, A.; Huo, *J. Chem. Soc. Rev.* "Metal–organic framework growth at functional interfaces: thin films and composites for diverse applications." **2012**, 41, 2344–2381.
26. Nan, J.; Dong, X.; Wang, W.; Jin, W.; Xu, N. *Langmuir* "Step-by-Step Seeding Procedure for Preparing HKUST-1 Membrane on Porous r-Alumina Support." **2011**, 27, 4309–4312.
27. Sakamoto, H.; Matsudab, R.; Kitagawa, S. *Dalton Transactions* "Systematic mechanochemical preparation of a series of coordination pillared layer frameworks." **2012**, 41, 3956-3961.
28. Batten, S.R.; Champness, N.R.; Chen X.-M.; Garcia-Martinez, J.; Kitagawa, S.; Öhrström, L.; O'Keeffe M.; Suhh, M.P.; and Reedijki J. *CrystEngComm*. "Coordination polymers, metal–organic frameworks and the need for terminology guidelines." **2012** 14, 3001.
29. Yaghi, O.M. and Li, H. *J. Am. Chem. Soc.* "Hydrothermal Synthesis of a Metal-Organic Framework Containing Large Rectangular Channels." **1995**, 117, 10401-10402.
30. Vukotic, V.N.; Harris, K.J.; Zhu, K.; Schurko, R. W.; Loeb, S. J. *Nature Chemistry "Metal–organic frameworks with dynamic interlocked components."* **2012**, 4, 456-460.
31. Liua, G.-X.; Chaa, C.-H.; Lia, X.-L.; Zhanga, C.-Y.; Wanga, Y.; Nishiharac, S.; Rena, X.-M. *Inorg. Chem. Comm.* "An unusual two-dimensional 2-fold interpenetrating metal-organic framework based on tetranuclear manganese (II) clusters: Synthesis, structure and magnetic properties." **2011** 14, 6, 867-872.
32. Tranchemontagne, D.J.; Hunt, J.R.; Yaghi, O.M. *Tetrahedron* "Room temperature synthesis of metal-organic frameworks: MOF-5, MOF-74, MOF-177, MOF-199, and IRMOF-0." **2008**, 64, 8553–8557.
33. Calderone, P.J.; Banerjee, D.; Santulli, A.C.; Wong, S.S.; Parise, J.B. *Inorganica Chimica Acta* "Synthesis, characterization, and luminescence properties of magnesium coordination networks using a thiophene-based linker." **2011**, 378, 109–114.

34. Ma, S.; Fillinger, J.A.; Ambrogio, M.W.; Zuo, J.-L.; Zhou, H.-C. *Inorganic Chemistry Communications* "Synthesis and characterizations of a magnesium metal–organic framework with a distorted (10, 3)-a-net topology." **2007**, 10, 220–222.
35. Xiao, D.; Yuan, R.; Chai, Y.; Wang, E. *Eur. J. Inorg. Chem.* "Two (3,10)-Connected 2D Networks Based on Pentanuclear Metal Clusters as Building Blocks." **2008**, 2610–2615.
36. Wu, Z.-F.; Hu, B.; Feng, M.-L.; Huang, X.-Y.; Zhao, Y.-B. *Inorganic Chemistry Communications* "Ionothermal synthesis and crystal structure of a magnesium metal-organic framework." **2011**, 14, 1132–1135.
37. Chen, X.-L.; Gou, L.; Hu, H.-M.; Feng Fu, F.; Han, Z.-X.; Shu, H.-M.; Yang, M.-L.; Xue, G.-L.; Du, C.-Q. *Eur. J. Inorg. Chem.* "New Examples of Metal Coordination Architectures of 4,4-Sulfonyldibenzoic Acid: Syntheses, Crystal Structure and Luminescence." **2008**, 239–250.
38. Prajapati, R.; Mishra, L.; Kimura, K.; Raghavaiah, P. *Polyhedron* "Metal–organic frameworks (MOFs) constructed from ZnII/CdII-2,20-bipyridines and polycarboxylic acids: Synthesis, characterization and microstructural studies." **2009**, 28 600–608.
39. Zhuang, W.J.; Sun, C.-Y.; Jin, L.-P. *Polyhedron* "Assembly and structures of five new Cu(II) complexes based on the V-shaped building block [Cu(dbsf)]." **2007**, 26, 1123-1132.
40. Mietrach, A.; Muesmann, T.W.T.; Christoffers, J.; Wickleder, M.S. *Eur. J. Inorg. Chem.* "Sulfonic Acid Analogs of Terephthalic and Trimesic Acid as Linkers in Metal-Organic Frameworks – Synthesis of Thermally Robust MOFs." **2009**, 5328-5334.
41. Qiu, W.; Perman, J.A.; Wojtas, L.; Eddaoudi, M.; Zaworotko, M.J. *Chem. Commun*. "Structural diversity through ligand flexibility: two novel metal–organic nets via ligand-to-ligand cross-linking of "paddlewheels"." **2010**, 46, 8734-8736.
42. zeolite.utm.mv Retrieved February 28, 2012.
43. Carol J. Hirt. Materials Research Laboratories, Struthers, OH. Internal Standard.
44. Anthony M. Yurcho *Microstructural Investigation of Al/Al-Fe alloy-Al_2O_3 Interpenetrating Phase Composites Produced by Reactive Metal Penetration*, MS Thesis, Youngstown State University, Youngstown, OH, **2011.**
45. Matthias Zeller. *User Guide SMART APEX CCD Diffractometer with Apex2 Software Upgrade and Bruno Robot*, **2009**, 1-53.
46. Rachel L. Kusnic *Solid-State Analytical Chemistry: Surface and Bulk Characterization by Complementary Analytical Methods*, MS Thesis, Youngstown State University, Youngstown OH, **2007.**
47. Perkin Elmer. *Thermogravametric Analysis: A Beginner's Guide*. **2010,** 1-19.

48. Jeffery Long and Omar Yaghi Chem. Soc. Rev. **2009**, 38, 1294-1314.
49. **Bruker** APEXII **CCD diffractometer**. Absorption correction: multi-scan (SADABS; **Bruker** (**2011**). Apex2 v2011.2-0, SHELXTL 6.14 (Bruker, **2003**; Sheldrick, **2008**), SHELXTL 6.14, Shelxle (Hübschle et al., **2011**), SHELXTL 6.14.
50. Coker, E.N.; Boyle, T.J.; Rodriguez, M. A.; Alam, T.M. *Polyhedron* "Structurally characterized magnesium carboxylates with tuned melting points." **2004**, 23, 1739–1747.
51. Yang,K.-C.; Chang, C.-C.; Yeh, C.-S.; Lee, G.-H.; Peng, S.-M. *Organometallics* "Steric and Solvent Effects on the CO_2 Fixation of Magnesium Compounds." **2001**, *20*, 126-137.
52. Chow, E.H. H.; Strobridge, F.C.; Friscic, T. *ChemComm* "Mechanochemistry of magnesium oxide revisited: facile derivatisation of pharmaceuticals using coordination and supramolecular chemistry." **2010**, *46*, 6368–6370.
53. Davies, R.P.; Less, R.J.; Lickiss, P.D.; White, A.J.P. *Dalton Transactions* "Framework materials assembled from magnesium carboxylate building units." **2007**, 2528–2535.
54. Senkovska, I.; Fritsch, J.; Kaskel, S. *Eur. J. Inorg. Chem.* "New Polymorphs of Magnesium-Based Metal–Organic Frameworks $Mg_3(ndc)_3$(ndc = 2,6-Naphthalenedicarboxylate)." **2007**, 5475–5479.
55. Li-Rong, Y.; Huai-Min, Z.; Qian-qian, Y.; Lan-Zhi Wu, L.; Liu, S. S. *CrystEngComm* "Coordination polymers based on 3,3',4,4'-benzophenone-tetracarboxylate and N-containing pillars: syntheses, structures, characterization and properties." **2013** 1-22.
56. Moqing Hu. *"Design, synthesis and applications of Metal Organic Frameworks."* MS Thesis, Worcester Polytechnic Institute, **2011**.

Appendix A

Principal X-ray Emission and Absorption Edge Energies (keV)

Atomic Number	K_α	K_β	$K_{(abs)}$	L_α	$L_{\beta 1}$	$L_{\beta 2}$	$L_{\gamma 1}$	$L_{III(abs)}$	$L_{II(abs)}$	$M_{V(abs)}$	M_α
1 H			0.014								
2 He			0.025								
3 Li			0.055					0.003	0.003		
4 Be			0.112					0.002	0.002		
5 B			0.186					0.003	0.003		
6 C	0.277		0.282					0.002	0.002		
7 N	0.392		0.400					0.008	0.008		
8 O	0.525		0.531					0.009	0.009		
9 F	0.677		0.692								
10 Ne	0.848		0.874					0.019	0.019		
11 Na	1.041	1.067	1.070					0.031	0.031		
12 Mg	1.253	1.295	1.303					0.050	0.050		
13 Al	1.486	1.553	1.559					0.073	0.073		
14 Si	1.739	1.829	1.842					0.102	0.103		
15 P	2.013	2.136	2.142					0.128	0.129		
16 S	2.307	2.464	2.470					0.163	0.164		
17 Cl	2.621	2.815	2.820					0.197	0.199		
18 Ar	2.957	3.190	3.200					0.224	0.246		
19 K	3.312	3.589	3.609					0.295	0.298		
20 Ca	3.690	4.012	4.038	0.341	0.345		0.350	0.346	0.350		
21 Sc	4.088	4.460	4.496	0.395	0.400		0.407	0.403	0.411		
22 Ti	4.508	4.931	4.964	0.452	0.458		0.460	0.454	0.460		
23 V	4.949	5.426	5.464	0.511	0.519		0.520	0.513	0.519		
24 Cr	5.411	5.924	5.987	0.573	0.583		0.583	0.574	0.581		
25 Mn	5.894	6.489	6.537	0.637	0.649		0.652	0.641	0.650		
26 Fe	6.398	7.057	7.111	0.705	0.718		0.721	0.709	0.720		
27 Co	6.924	7.648	7.709	0.776	0.791		0.794	0.779	0.794		
28 Ni	7.471	8.263	8.331	0.851	0.869			0.854	0.871		
29 Cu	8.040	8.904	8.981	0.930	0.950			0.933	0.953		
30 Zn	8.630	9.570	9.661	1.012	1.034			1.022	1.045		
31 Ga	9.241	10.262	10.395	1.098	1.125			1.144	1.171		
32 Ge	9.874	10.979	11.100	1.188	1.218			1.214	1.245		
33 As	10.530	11.722	11.867	1.282	1.317			1.324	1.359		
34 Se	11.207	12.492	12.656	1.379	1.419			1.434	1.475		
35 Br	11.907	13.287	13.470	1.480	1.526			1.552	1.599		
36 Kr	12.631	14.107	14.320	1.586	1.636		1.703	1.674	1.729		
37 Rb	13.373	14.956	15.201	1.694	1.752		2.050	1.806	1.866		
38 Sr	14.140	15.829	16.106	1.806	1.871		2.196	1.941	2.008		
39 Y	14.931	16.731	17.037	1.922	1.995		2.346	2.080	2.155		
40 Zr	15.744	17.660	17.995	2.042	2.124	2.219	2.302	2.221	2.305		
41 Nb	16.581	18.614	18.989	2.166	2.257	2.367	2.461	2.374	2.467		
42 Mo	17.441	19.600	20.002	2.293	2.394	2.518	2.623	2.524	2.629		
43 Tc	18.325	20.608	21.054	2.424	2.536			2.677	2.795		
44 Ru	19.233	21.646	22.117	2.558	2.683	2.835	2.964	2.838	2.966		
45 Rh	20.165	22.712	23.218	2.696	2.834	3.001	3.143	3.002	3.144		
46 Pd	21.121	23.806	24.349	2.838	2.990	3.171	3.328	3.172	3.329		
47 Ag	22.101	24.928	25.512	2.984	3.150	3.347	3.519	3.350	3.522		
48 Cd	23.106	26.081	26.711	3.133	3.316	3.528	3.716	3.538	3.727		
49 In	24.136	27.260	27.937	3.286	3.487	3.713	3.920	3.729	3.937		
50 Sn	25.191	28.467	29.200	3.443	3.662	3.904	4.130	3.928	4.156		
51 Sb	26.271	29.706	30.491	3.604	3.843	4.100	4.347	4.132	4.381		
52 Te	27.377	30.974	31.813	3.769	4.029	4.301	4.570	4.342	4.612		
53 I	28.508	32.272	33.170	3.937	4.220	4.507	4.800	4.559	4.853		
54 Xe	29.666	33.599	34.561	4.109				4.783	5.103		
55 Cs	30.851	34.961	35.983	4.286	4.619	4.935	5.279	5.011	5.359		
56 Ba	32.062	36.354	37.443	4.465	4.827	5.156	5.530	5.247	5.624		
57 La	33.299	37.771	38.932	4.650	5.041	5.383	5.788	5.490	5.897		0.833
58 Ce	34.566	39.223	40.447	4.839	5.261	5.612	6.051	5.729	6.169		0.883
59 Pr	35.860	40.711	41.995	5.033	5.488	5.849	6.321	5.969	6.445		0.929
60 Nd	37.182	42.231	43.577	5.229	5.721	6.088	6.602	6.215	6.728		0.978
61 Pm	38.532	43.783	45.190	5.432	5.960	6.338	6.891	6.462	7.022		
62 Sm	39.911	45.366	46.835	5.635	6.204	6.586	7.177	6.720	7.340		1.081
63 Eu	41.320	46.987	48.498	5.845	6.455	6.842	7.479	6.981	7.633		1.131
64 Gd	42.757	48.642	50.228	6.056	6.712	7.102	7.784	7.243	7.930		1.185
65 Tb	44.226	50.325	51.983	6.272	6.977	7.365	8.100	7.515	8.252		1.240
66 Dy	45.724	52.058	53.840	6.494	7.246	7.634	8.417	7.796	8.588		1.293
67 Ho	47.253	53.813	55.600	6.719	7.524	7.910	8.746	8.067	8.912		1.347
68 Er	48.813	55.606	57.457	6.947	7.809	8.188	9.087	8.357	9.263		1.405
69 Tm	50.406	57.437	59.376	7.179	8.100	8.467	9.424	8.650	9.616		1.462
70 Yb	52.030	59.322	61.313	7.414	8.400	8.757	9.778	8.944	9.979		1.521
71 Lu	53.687	61.235	63.306	7.654	8.708	9.047	10.142	9.242	10.346		1.581
72 Hf	55.382	63.183	65.347	7.898	9.021	9.346	10.514	9.558	10.736		1.644
73 Ta	57.098	65.125	67.406	8.145	9.342	9.650	10.893	9.874	11.129		1.709
74 W	58.856	67.140	69.519	8.396	9.671	9.960	11.284	10.202	11.540	1.809	1.774
75 Re	60.648	69.199	71.678	8.651	10.008	10.274	11.683	10.537	11.960		1.842
76 Os	62.477	71.298	73.866	8.910	10.354	10.597	12.093	10.866	12.380		1.914
77 Ir	64.339	73.438	76.108	9.174	10.706	10.919	12.510	11.210	12.819	2.041	1.978
78 Pt	66.241	75.618	78.386	9.441	11.069	11.249	12.940	11.557	13.266	2.122	2.048
79 Au	68.177	77.840	80.723	9.712	11.440	11.583	13.379	11.919	13.734	2.206	2.120
80 Hg	70.154	80.103	83.113	9.987	11.821	11.922	13.828	12.286	14.213	2.295	2.195
81 Tl	72.167	82.497	85.529	10.267	12.211	12.270	14.289	12.658	14.696	2.389	2.268
82 Pb	74.221	84.859	88.014	10.550	12.612	12.621	14.762	13.039	15.205	2.484	2.342
83 Bi	76.315	87.328	90.471	10.837	13.021	12.978	15.245	13.419	15.715	2.579	2.418
84 Po	78.452	89.781	93.112	11.129	13.445	13.338	15.741	13.817	16.244		
85 At	80.624	92.287	95.740	11.425	13.874		16.249	14.215	16.784		
86 Rn	82.843	94.850	98.418	11.725	14.313		16.768	14.618	17.337		
87 Fr	85.110	97.460	101.147	12.029	14.768	14.448	17.300	15.028	17.904		
88 Ra	87.419	100.113	103.900	12.338	15.233	14.839	17.845	15.444	18.482		
89 Ac	89.773	102.829	106.759	12.650	15.710		18.405	15.865	19.078		
90 Th	92.174	105.591	109.630	12.967	16.199	15.621	18.979	16.299	19.696	3.332	2.991
91 Pa	94.627	108.409	112.581	13.288	16.699	16.022	19.565	16.731	20.311		3.077
92 U	97.131	111.281	115.610	13.612	17.217	16.425	20.164	17.164	20.939	3.552	3.165
93 Np	99.407	113.725	118.619	13.942	17.747	16.837	20.781	17.614	21.596		
94 Pu	101.857	116.943	121.200	14.276	18.291	17.252	21.414	18.066	22.262		
95 Am	104.431	120.350	124.876	14.615	18.849	17.673	22.061	18.525	22.944		

Table Appendix A: Solubility Chart of Solvents

Serial Number	Name	Molecular Formula	Molecular Weight (g/mole)	1-butanol (118°C)	2-butanol (98°C)	1,4-dioxane (101.1°C)	1-hexanol (155-159 °C)	1-pentanol (136-138°C)	1-propanol (97-98 °C)	2-propanol (82.5 °C)	Acetonitrile (82 °C)	Cyclohexanol (160-161 °C)	Diethyl carbonate (126-128°C)	Dimethyl carbonate (90°C)	DMF (153 °C)	Ethanol (78 °C)	Methanol (65 °C)	Piperidine (106 °C)	THF (66°C)	Water (100 °C)
1	**Isophthalic Acid**	$C_8H_6O_4$	166.13	✗		✗	✓	✗	✗	✗					✓	✗	✗		✗	✗
2	**1,4-Cyclohexane Dicarboxylic Acid**	$C_8H_{12}O_4$	172.18	✓		✗	✓	✓	✓	✓					✓	✓	✓		✓	✓
3	**4,4'-Oxybis(Benzoic Acid)**	$C_{14}H_{10}O_5$	258.23	✗		✗	✗	✗	✗	✗					✓	✗	✗		✗	✗
4	**4,4'-Sulfonyldibenzoic Acid**	$C_{14}H_{10}O_6S$	306.29	✗		✗	✗	✗	✗	✗					✓	✗	✗		✗	✗
5	**Terephthalic Acid**	$C_8H_6O_4$	166.13	✗		✗	✓	✗	✗	✗					✓	✗	✗		✗	✗
6	**2,6-Pydridine Dicarboxylic Acid**	$C_7H_5NO_4$	167.12	✗		✗	✗	✗	✗	✗					✓	✗	✗		✗	✗
7	**2,3-Pyridine Dicarboxylic Acid**	$C_7H_5NO_4$	167.12	✗		✗	✗	✗	✗	✗					✓	✗	✗		✗	✗

Appendix B

Experimental details of [1]

Chemical formula	$C_{49}H_{42}Mg_3N_2O_{21}S_3 \cdot C_3H_7NO$
M_r	1237.05
Crystal system, space group	Monoclinic, $P2_1/n$
Temperature (K)	100
a, b, c (Å)	16.2489 (17), 20.219 (2), 17.0937 (18)
β (°)	100.0065 (18)
V (Å^3)	5530.4 (10)
Z	4
F(000)	2568
D_x (Mg m^{-3})	1.486
Radiation type	Mo $K\alpha$
No. of reflections for cell measurement	2969
θ range (°) for cell measurement	2.6–32.0
μ (mm^{-1})	0.25
Crystal shape	Block
Colour	Colourless
Crystal size (mm)	0.39 × 0.34 × 0.32
Diffractometer	Bruker AXS *SMART APEX* CCD diffractometer
Radiation source	sealed tube
Monochromator	Graphite
Scan method	ϕ and ω scans
Absorption correction	Multi-scan Apex2 v2012.4-3 (Bruker, 2012)
T_{min}, T_{max}	0.701, 0.746
No. of measured, independent and observed [$I > 2\sigma(I)$] reflections	34972, 17274, 13721
R_{int}	0.024
θ values (°)	θ_{max} = 32.1, θ_{min} = 1.6
$(\sin\theta/\lambda)_{max}$ (Å^{-1})	0.748
Range of h, k, l	h = -23→22, k = -29→27, l = -8→25
$R[F^2 > 2\sigma(F^2)]$, $wR(F^2)$, S	0.038, 0.097, 1.02
No. of reflections	17274
No. of parameters	806
No. of restraints	37
H-atom treatment	H atoms treated by a mixture of independent and

	constrained refinement
Weighting scheme	$w = 1/[\sigma^2(F_o^2) + (0.0383P)^2 + 3.1041P]$ where $P = (F_o^2 + 2F_c^2)/3$
$\Delta\rho_{max}$, $\Delta\rho_{min}$ (e Å^{-3})	0.54, -0.45

Symmetry code(s): (i) -*x*+3/2, *y*-1/2, -*z*+3/2; (ii) -*x*+1/2, *y*+1/2, -*z*+3/2; (iii) *x*-1/2, -*y*+1/2, *z*+1/2; (iv) -*x*+3/2, *y*+1/2, -*z*+3/2; (v) -*x*+1/2, *y*-1/2, -*z*+3/2; (vi) *x*+1/2, -*y*+1/2, *z*-1/2. Symmetry code(s): (i) -*x*+1, -*y*+1, -*z*+1.

Experimental Details of [2]

Chemical formula	$C_{53.72850}H_{51.36648}Mg_3N_{3.909}O_{21.91}S_3$
M_r	1271.84
Crystal system, space group	Monoclinic, $P2_1/n$
Temperature (K)	100
a, *b*, *c* (Å)	16.5983 (11), 20.6101 (14), 17.5553 (12)
β (°)	99.670 (1)
V (Å^3)	5920.2 (7)
Z	4
F(000)	2642.3
D_x (Mg m^{-3})	1.426
Radiation type	Mo *K*α
No. of reflections for cell measurement	6701
θ range (°) for cell measurement	2.3–26.9
μ (mm^{-1})	0.24
Crystal shape	Fragment
Colour	Pink
Crystal size (mm)	0.52 × 0.37 × 0.30
Diffractometer	Bruker AXS *SMART APEX* CCD diffractometer
Radiation source	fine-focus sealed tube
Monochromator	Graphite
Scan method	ω scans
Absorption correction	Multi-scan Apex2 v2011.2-0 (Bruker, 2011)
T_{min}, T_{max}	0.681, 0.746
No. of measured, independent and observed [$I > 2\sigma(I)$] reflections	47043, 18707, 12352
R_{int}	0.044
θ values (°)	θ_{max} = 32.0, θ_{min} = 1.5

$R[F^2 > 2\sigma(F^2)]$, $wR(F^2)$, S	0.062, 0.143, 1.03
No. of reflections	18707
No. of parameters	959
No. of restraints	160
H-atom treatment	H-atom parameters constrained
Weighting scheme	$w = 1/[\sigma^2(F_o^2) + (0.0507P)^2 + 3.1335P]$ where $P = (F_o^2 + 2F_c^2)/3$
$\Delta\rho_{max}$, $\Delta\rho_{min}$ (e Å^{-3})	0.60, -0.50

Symmetry code(s): (i) -*x*+3/2, *y*-1/2, -*z*+1/2; (ii) -*x*+3/2, *y*+1/2, -*z*+1/2; (iii) *x*-1/2, -*y*+1/2, *z*+1/2; (iv) -*x*+1/2, *y*+1/2, -*z*+1/2; (v) -*x*+1/2, *y*-1/2, -*z*+1/2; (vi) *x*+1/2, -*y*+1/2, *z*-1/2.

Experimental Details of [3]

Chemical formula	$C_{49.31}H_{41.21}Mg_3N_{1.93}O_{21}S_3 \cdot 0.86(C_3H_7NO) \cdot 0.25(H_2O)$
M_r	1233.31
Crystal system, space group	Monoclinic, $P2_1/n$
Temperature (K)	100
a, *b*, *c* (Å)	16.5833 (11), 20.1642 (14), 17.2410 (12)
β (°)	99.927 (1)
V (Å^3)	5678.9 (7)
Z	4
F(000)	2558.1
D_x (Mg m^{-3})	1.442
Radiation type	Mo *K*α
No. of reflections for cell measurement	9919
θ range (°) for cell measurement	2.4–29.2
μ (mm^{-1})	0.25
Crystal shape	Block
Colour	Colourless
Crystal size (mm)	0.55 × 0.51 × 0.48
Diffractometer	Bruker AXS *SMART APEX* CCD diffractometer
Radiation source	sealed tube
Monochromator	Graphite
Scan method	ϕ and ω scans
Absorption correction	Multi-scan Apex2 v2012.4-3 (Bruker, 2012)
T_{min}, T_{max}	0.716, 0.746
No. of measured, independent and	75568, 15435, 12558

observed [$I > 2\sigma(I)$] reflections	
R_{int}	0.025
θ values (°)	θ_{max} = 29.3, θ_{min} = 1.6
$(\sin\theta/\lambda)_{max}$ (Å^{-1})	0.688
Range of *h*, *k*, *l*	*h* = -22→22, *k* = -27→27, *l* = -23→23
$R[F^2 > 2\sigma(F^2)]$, $wR(F^2)$, *S*	0.059, 0.175, 1.03
No. of reflections	15435
No. of parameters	911
No. of restraints	301
H-atom treatment	H-atom parameters constrained
Weighting scheme	$w = 1/[\sigma^2(F_o^2) + (0.083P)^2 + 7.6481P]$ where $P = (F_o^2 + 2F_c^2)/3$
$(\Delta/\sigma)_{max}$	0.001
$\Delta\rho_{max}$, $\Delta\rho_{min}$ (e Å^{-3})	1.00, -0.58

Symmetry code(s): (i) -*x*+3/2, *y*-1/2, -*z*+3/2; (ii) -*x*+1/2, *y*+1/2, -*z*+3/2; (iii) *x*-1/2, -*y*+1/2, *z*+1/2; (iv) -*x*+3/2, *y*+1/2, -*z*+3/2; (v) -*x*+1/2, *y*-1/2, -*z*+3/2; (vi) *x*+1/2, -*y*+1/2, *z*-1/2.

Experimental Details of [4]

Chemical formula	$C_{49.89}H_{43.89}Mg_3N_{1.89}O_{21}S_3\cdot C_3H_7NO$
M_r	1248.12
Crystal system, space group	Monoclinic, $P2_1/n$
Temperature (K)	100
a, *b*, *c* (Å)	16.5646 (18), 20.198 (2), 17.2403 (18)
β (°)	99.9137 (15)
V (Å^3)	5682.1 (10)
Z	4
F(000)	2594.3
D_x (Mg m^{-3})	1.459
Radiation type	Mo *K*α
No. of reflections for cell measurement	9971
θ range (°) for cell measurement	2.4–31.9
μ (mm^{-1})	0.25
Crystal shape	Block
Colour	Pink
Crystal size (mm)	0.49 × 0.32 × 0.29
Diffractometer	Bruker AXS *SMART APEX* CCD diffractometer
Radiation source	fine-focus sealed tube

Monochromator	Graphite
Scan method	ω scans
Absorption correction	Multi-scan Apex2 v2011.2-0 (Bruker, 2011)
T_{min}, T_{max}	0.666, 0.746
No. of measured, independent and observed [$I > 2\sigma(I)$] reflections	88713, 18570, 14457
R_{int}	0.026
θ values (°)	$\theta_{max} = 32.1$, $\theta_{min} = 1.6$
$(\sin\theta/\lambda)_{max}$ (Å^{-1})	0.747
Range of h, k, l	$h = -24\rightarrow23$, $k = -29\rightarrow29$, $l = -24\rightarrow25$
$R[F^2 > 2\sigma(F^2)]$, $wR(F^2)$, S	0.043, 0.119, 1.05
No. of reflections	18570
No. of parameters	983
No. of restraints	75
H-atom treatment	H atoms treated by a mixture of independent and constrained refinement
Weighting scheme	$w = 1/[\sigma^2(F_o^2) + (0.0499P)^2 + 2.9521P]$ where $P = (F_o^2 + 2F_c^2)/3$
$\Delta\rho_{max}$, $\Delta\rho_{min}$ (e Å^{-3})	0.75, -0.41

Symmetry code(s): (i) x-1/2, -y+1/2, z+1/2; (ii) -x+3/2, y-1/2, -z+1/2; (iii) -x+1/2, y-1/2, -z+1/2; (iv) -x+3/2, y+1/2, -z+1/2; (v) x+1/2, -y+1/2, z-1/2; (vi) -x+1/2, y+1/2, -z+1/2.